

Structural investigations of lipids and proteins using MS ultraviolet photodissociation

Cumulative dissertation

by

Simon Sommer



Submitted to the

Faculty of Biology and Chemistry (FB 08)

and prepared at the

Institute of Inorganic and Analytical Chemistry

for the degree of

Doctor rerum naturalium (Dr. rer. nat.)

Justus Liebig University Giessen, Germany

Giessen 2022

This thesis was accepted as a doctoral dissertation in fulfillment of the requirements for the degree of Doctor rerum naturalium by the Faculty of Biology and Chemistry, Justus Liebig University Giessen, Germany.

1. Referee: Prof. Dr. Bernhard Spengler

Institute of Inorganic and Analytical Chemistry, Justus Liebig University Giessen, Germany

2. Referee: Prof. Dr. Bernd Smarsly

Institute of Physical Chemistry, Justus Liebig University Giessen, Germany

Table of contents

Publication list	I
Abstract	II
Zusammenfassung	III
I. Subject of this work	1
Introduction	1
Bioanalytical chemistry	1
Lipids	4
Proteins	6
Tandem mass spectrometry	8
Biological application of tandem mass spectrometry	10
Ionization in mass spectrometry	12
Mass analyzers	13
Computational chemistry	15
Aim of this work	17
Results and Discussion	19
Relative Quantification of Phosphatidylcholine sn-Isomers Using Positive Doubly Charged Lipid-Metal Ion Complexes (Publication 3)	19
IRMPD Spectroscopy of [PC (4:0/4:0) + M] ⁺ (M = H, Na, K) and Corresponding CID Fragment Ions (Publication 4)	21
Influence of Protein Ion Charge State on 213 nm Top-Down UVPD (Publication 5)	23
Outlook	25
References	31
II. Publications	48
Publication 3	48
Publication 4	57
Publication 5	68
III. Appendix	79
Acknowledgements	79
Declaration	80

Publication list

1. Selective Phosphatidylcholine Double Bond Fragmentation and Localisation Using Paternò-Büchi Reactions and Ultraviolet Photodissociation

Fabian Wäldchen, Simon Becher, Patrick Esch, Mario Kompauer, and Sven Heiles

Analyst **2017**, *142*, 4744-4755

DOI: 10.1039/c7an01158j

2. Effects of Wavelength, Fluence, And Dose on Fragmentation Pathways and Photoproduct Ion Yield in 213 nm and 266 nm Ultraviolet Photodissociation Experiments

Simon Becher, Bernhard Spengler, and Sven Heiles

European Journal of Mass Spectrometry **2018**, *24* (1) 54-65

DOI: 10.1177/1469066717741747

3. Relative Quantification of Phosphatidylcholine *sn*-Isomers Using Positive Doubly Charged Lipid-Metal Ion Complexes

Simon Becher, Patrick Esch, and Sven Heiles

Analytical Chemistry **2018**, *90*, 11486-11494

DOI: 10.1021/acs.analchem.8b02731

4. IRMPD Spectroscopy of [PC (4:0/4:0) + M]⁺ (M = H, Na, K) and Corresponding CID Fragment Ions

Simon Becher, Giel Berden, Jonathan Martens, Jos Oomens, and Sven Heiles

Journal of the American Society for Mass Spectrometry **2021**, *32*, 12, 2874–2884

DOI: 10.1021/jasms.1c00277

5. Influence of Protein Ion Charge State on 213 nm Top-Down UVPD

Simon Becher, Huixin Wang, Michael G. Leeming, William A. Donald, and Sven Heiles

Analyst **2021**, *146*, 3977-3987

DOI: 10.1039/D1AN00571E

Publication 3,4,5: The doctoral thesis is based on these publications.

Abstract

Ultraviolet photodissociation (UVPD) is an emerging method for the structural analysis of molecular ions in mass spectrometric experiments. To increase the capabilities of UVPD in bioanalytical research, new structure-specific workflows are required and details of the UVPD-triggered fragmentation event need to be understood to improve the scope of the methodology.

In the presented work, UVPD methods were developed and used to tackle existing challenges of analyte characterization in lipidomics and proteomics. In particular, an UVPD workflow for the discrimination of *sn*-isomers was developed. Bivalent metal salts (*e.g.*, FeCl₂) were added to electrospray ionization (ESI) solvents. This led to the formation of doubly charged metal-glycerophospholipid (GP) ions, which were fragmented using collision-induced dissociation and UVPD. Selective cleavage of the fatty acid in *sn*-2 position was observed. The selectivity of the fragmentation was used as a measure for the relative *sn*-isomer abundance in egg yolk, porcine brain, yeast, and mouse pancreas lipid extracts.

In order to rationalize the *sn*-selectivity introduced via metal ion-adduction, the structures of precursor and fragment ions were investigated. Infrared multiphoton dissociation (IRMPD) spectra of [GP + H/Na/K/Fe]⁺²⁺ and [GP + Na/K - 183]⁺ were obtained. By comparison of the IRPMD spectra to theoretical spectra of quantum-chemically predicted structures, gas-phase structures of the precursor and fragment ions were assigned. The gas-phase structures of the precursor and the fragment were used to draw conclusions of likely fragmentation mechanism of GP ions.

Lastly, the fragmentation sites and efficiencies of intact protein ions upon UVPD activation as a function of the charge carrier quantity and position were investigated. The model proteins ubiquitin, cytochrome c, and myoglobin were sprayed from ESI solutions containing substances for native, denaturing, and supercharging of the proteins. Comparison of the data with calculations of charge carrier positions revealed a correlation between the location of the charge carrier and the fragmentation sites.

Zusammenfassung

Ultraviolette Photodissoziation (UVPD) ist eine vielversprechende Methode für die Strukturaufklärung, welcher in den letzten Jahren zunehmende Beachtung zuteilwurde. Für eine breitere Anwendbarkeit ist die Entwicklung neuer Arbeitsvorschriften, sowie ein Verständnis der zugrundeliegenden Fragmentierungsprozesse essentiell.

Im Rahmen dieser Arbeit wurde eine Methode für die Unterscheidung von *sn*-Isomeren entwickelt. Dafür wurden zweiwertige Metallsalze (z.B. FeCl₂) zur Lösung in Elektrospray-Ionisations- (ESI) Experimenten gegeben. Bei der Fragmentierung der zweifach geladenen Metall-Glycerophospholipid (GP) Ionen mittels UVPD wurde eine selektive Abspaltung der Fettsäuren in *sn*-2 Position beobachtet. Diese selektive Fragmentierung wurde für die relative Quantifizierung von *sn*-Isomeren in Eigelb-, Schweinehirn-, Hefe- und Mauspankreaslipidextrakten genutzt. Dies ermöglichte die relative Quantifizierung von *sn*-Isomeren in Tandem-Massenspektrometrie (MS²) Experimenten durch das Zufügen zweiwertiger Metallsalze.

Die Gasphasenstrukturen verschiedener ein- und zweifach geladener Metall-GP Ionen und von Zwischenprodukten wurden studiert, um die zugrundeliegenden Fragmentierungsprozesse der *sn*-selektiven Abspaltung zu verstehen. Dafür wurden Experimente mittels infraroter Multiphotonendissoziations-Spektroskopie durchgeführt. Durch den Vergleich der spektroskopischen Daten mit quantenchemischen Berechnungen konnten die Gasphasenstrukturen von [GP + H/Na/K/Fe]^{+/2+} und [GP + Na/K - 183]⁺ beschrieben werden. Anhand der Gasphasenstruktur konnten postulierte Reaktionspfade gestützt und Einflüsse auf die Selektivität der Methode verstanden werden.

Als Beitrag zum Verständnis des Fragmentierungsprozess von Proteinen mittels UVPD wurde die Abhängigkeit der Bindungsbruchstellen von Position und Anzahl der Ladungsträger untersucht. Die Modellproteine Ubiquitin, Cytochrom c und Myoglobin wurden dafür in nativer, denaturierter und hochgeladener Form in ESI-MS² Experimenten untersucht. Die Ergebnisse zeigen einen Zusammenhang zwischen Fragmentierung und Ladungsträgerposition.

I. Subject of this work

Introduction

Bioanalytical chemistry

The properties of matter are distinguished by the bonding of atoms in molecules, their structure. The analysis of molecule structures is a major challenge in chemistry. Until the early 19th century, the analysis of molecules was limited to approaches like flame tests, precipitations, complexations, or chemical reactions.¹ In 1831, Justus von Liebig developed

“a device for the analysis of organic bodies ...”,

which combined reaction chambers for the quantitative analysis of carbon, hydrogen, oxygen and nitrogen of organic molecules.² The molecular structures, however, remained unclear. The availability of electricity in technical instruments boosted the development of devices for chemical analysis. Based on the proposals by Prout in 1815, first instruments for the analysis of molecular masses were described by Thomson in the beginning of the 20th century.³⁻⁶ Thomson’s first mass spectrometer (MS) used the inertia of ions to separate them in magnetic fields by their mass-to-charge (m/q) ratios (Figure 1), based on the fundamental work of Wilhelm Wien on channel rays in 1898.⁷ Today, MS can be applied to study for example lipids, peptides/proteins, and nanoparticles.^{8,9}

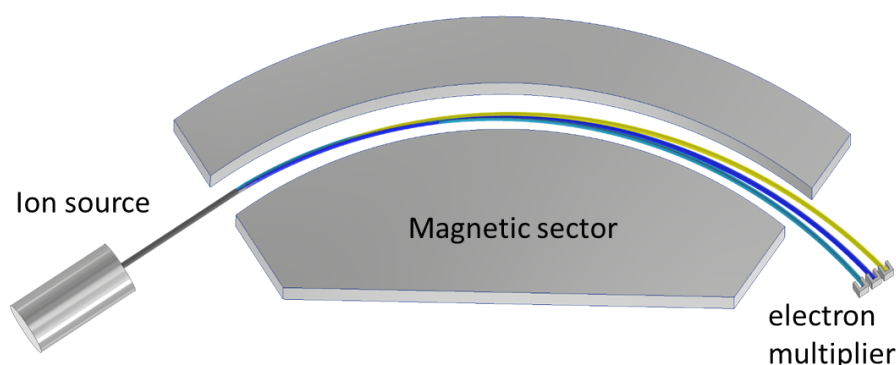


Figure 1. Scheme of a sector field mass spectrometer. Ion beams of species with different m/q values are shown as green, blue, and yellow lines.

However, biomolecules can also be separated and detected using the thin-layer chromatography, gas chromatography, or liquid chromatography (LC).^{10–13} Proteins can be characterized using enzyme-linked immunosorbent assays, western blots, or immunostaining.^{14–16} These methods lack information about the structure or the sum formulae of the analyte. Therefore, the analytes' identity can only be unraveled in comparison to literature or standard substances with these methods.

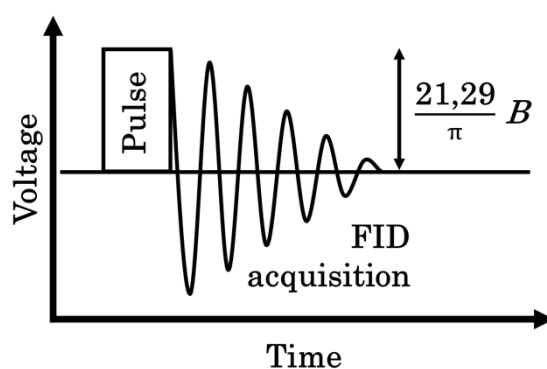


Figure 2. Sequence of excitation and relaxation in NMR experiments.¹⁷

Structural identification of purified samples can be performed with nuclear magnetic resonance (NMR) experiments. NMR is performed in magnetic fields up to 15 T in routine analysis.¹⁸ In an NMR sequence, the nuclei are excited by radiofrequencies followed by relaxation, which correlates to the chemical environment of the atoms (Figure 2).¹⁹ NMR typically provides information about relative proton-proton positions in one-dimensional or two-dimensional experiments through bond interactions, but can also be extended to heteroatoms, such as carbon, or interactions through space (Nuclear Overhauser Enhancement Spectroscopy).^{20–23} In contrast to MS, NMR is not destructive, but the amount of sample needed for NMR analysis is orders of magnitude higher.²⁴ In addition, increasing numbers of analyte atoms, for example hydrogen, challenge the resolution of NMR.²⁵

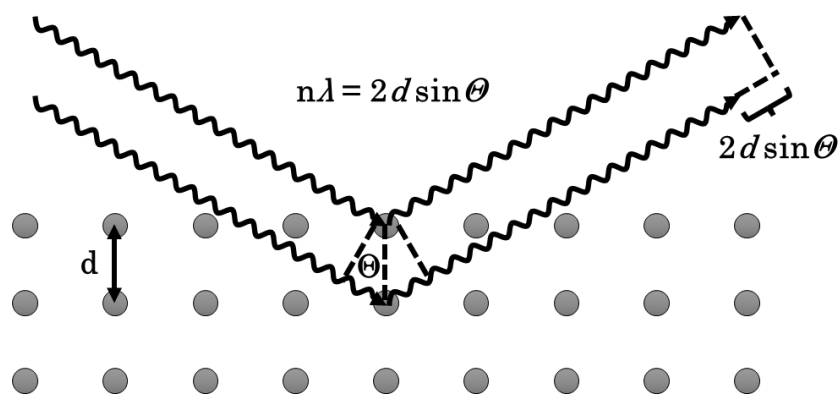


Figure 3. Scheme of the diffraction of X-rays by crystal structures and constructive interference according to Bragg's law.

Another method for structural analysis of biomolecules is X-ray crystallography (XRC), which is able to identify relative positions of all atoms but hydrogen.^{26,27} XRC uses the diffraction of X-rays on ordered structures (*e.g.* crystal structure) to determine the atom positions (Figure 3). The signal positions can be used to identify the atoms, and the intensity indicates the atom position in the unit cell. XRC is a powerful tool for structures which are too large for NMR or do not contain hydrogen atoms. On the other hand, the analyte needs to be enriched, purified, and crystallized prior to analysis. Cryogenic electron microscopy (cryo-EM) overcame the need for crystallization.^{28,29} Cryo-EMs are transmission electron microscopes, which allow the investigation of large biomolecules without substitution of water by embedding media. The analyte is cooled below the glass transition temperature of water within milliseconds, which decreases the formation of artefacts and traps molecules near their native form. By detecting the electron transition through the sample, electron densities can be calculated. However, the preparation of the sample remains challenging and the limited non-destructive electron beam fluence of 1 - 10 electrons per \AA^2 limits the sensitivity of the method.³⁰ To increase the sensitivity, experiments need to be performed under different angles followed by data processing.

MS is able to solve the challenges of sample preparation of NMR, XRC, and cryo-EM.³¹ Solved analytes can directly be injected into the instrument using MS. Coupled to LC, complex biological mixtures can be analyzed. Even imperfectly chromatographically separated analytes can be distinguished in a single MS

experiment.³² Additionally, amounts of the samples for meaningful analysis can be as low as 30 zmol per spectrum, but are roughly in the fmol range in routine analysis.³³ The high sensitivity and easy handling made MS the method of choice for the analysis of complex unknown biological samples.³⁴ However, MS is limited to information on the m/z ratio. Structure determination by MS requires fragmentation of the ions in MSⁿ experiments. The MSⁿ method and strategy strongly depends on the structural element of interest.³⁵ Structural elements of interest can, for example, be esters, double bonds (DBs), or headgroups in lipids.

Lipids

Lipids are of major interest because they are key molecules in the physiology of every known organism on our planet. The increasing interest in lipids as part of the “omics” fields is documented by the publications per year, which increased from 9 in 2003 to 1731 in 2021.³⁶ Lipids are loosely defined as

“... substances of biological origin that are soluble in nonpolar solvents”,

but are further divided into categories, which strongly differ in terms of their physicochemical properties and physiological application area (Figure 4).³⁷

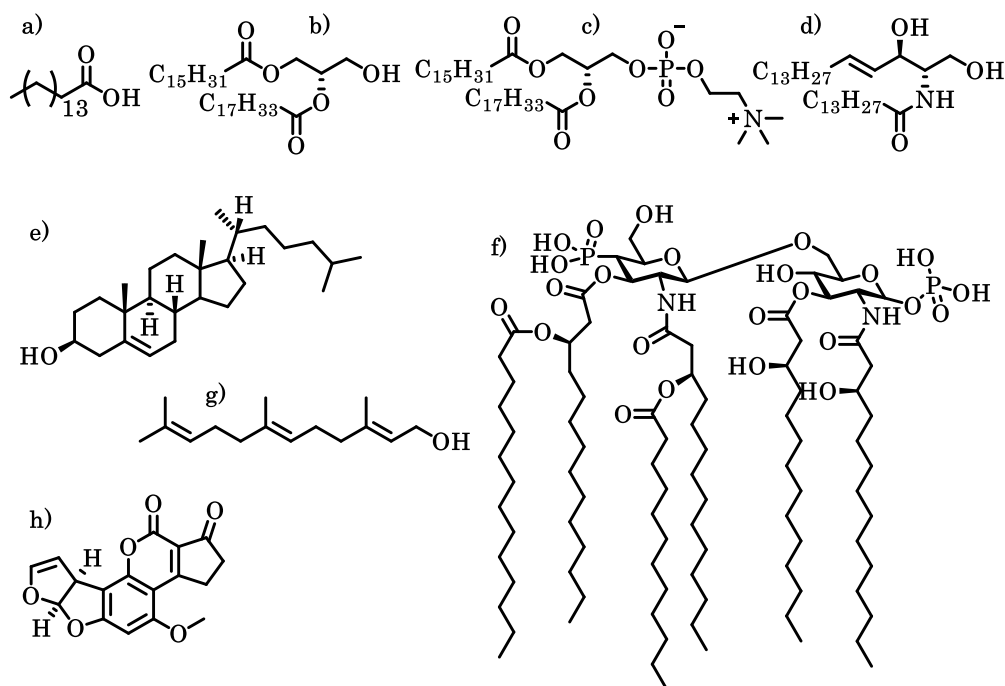


Figure 4. Examples of the lipid classes of a) fatty acids (palmitic acid), b) glycerol lipids (1-palmitoyl-2-oleoyl-glycerol), c) glycerophospholipids (1-palmitoyl-2-oleoyl-*sn*-glycero-3-phosphatidylcholine), d) sphingolipids (N-myristoyl-D-sphingosine), e) sterols (cholest-5-en-3 β -ol), f) glycolipids (lipid A in *E. coli*), g) terpene lipids (2*E*,6*E*-farnesol), and h) polyketides (aflatoxin B₁).³⁷

Lipids are important building blocks (fatty acids; FAs), serve for energy storage (glycerol lipids, sterol lipids), are precursors in biosynthesis (terpene lipids), can be found in outer membranes of gram-negative bacteria (saccharolipids), make up cell membranes, or are part of molecular signaling networks (glycerophospholipids, GPs).^{38–44} GPs are the most abundant category in multicellular organisms.⁴⁵ The structure of GPs consists of the glycerol backbone (yellow), two fatty acids (grey), and the phosphate-containing headgroup (orange) connected via ester and/or phosphoester bonds, respectively (Figure 5). Therefore, GPs can vary in the chemical identity of the headgroup, FAs (lengths, number of double bonds (DB), DB (blue) position, stereochemistry, quantity, and configuration), and permutations of FA moieties attached to the GP glycerol backbone. The latter is called stereospecific numbering (*sn*) - isomerism.

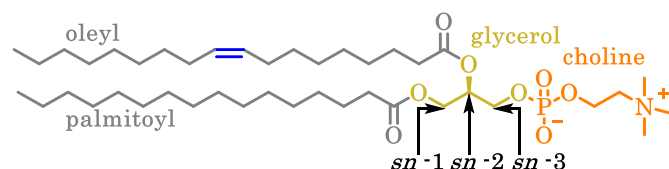


Figure 5. Structural elements of GPs, for the example of 1-palmitoyl-2-oleoyl-glycerol-3-phosphocholine (POPC). The glycerol backbone, fatty acids, the headgroup, and the DBs are color-coded in yellow, grey, orange, and blue, respectively.

Due to the high number of naturally occurring FAs (over 1,000) and the different head groups (around 17), the presence of lysolipids and *sn*-isomerism, the number of possible GPs can be carefully estimated to more than 17,000,000.^{37,46} This number does not take glycolipids or cyclic structures in FAs into account.^{47,48} The number of molecules and their similarity challenges analytical chemists and their methodologies to provide lipid quantities and structures in biological mixtures.

Proteins

Proteins are

“Naturally occurring and synthetic polypeptides having molecular weights greater than about 10000 ...”

the second most abundant class of biomolecules.^{49,50} Proteins are, for example, crucial for signal transmission in cells, transcription and repairing of the DNA, molecule transport, and biosynthesis of lipids and metabolites in enzymes.^{51–56} Due to the close interlinking of physiological processes, defects in the biosynthesis potentially lead to an entail of errors. To counteract this risk, highly selective processes in the biosynthesis are required, which are provided by proteins. They consist of an active site, where reactants are trapped. Similar to a lock and key, binding of educts to the active site is highly selective.⁵⁷ The alignment of the trapped educts determines the stereochemistry of the product.⁵⁸ After reaction, the products are released by the proteins, which are available for the next synthesis. The whole variety of protein biosynthesis is mainly built on only 20 amino acids.⁵⁹ Nevertheless, the number of proteins in humans are predicted to be 10,000 to several billion.^{60,61} The script for protein synthesis is coded in the DNA.⁶² For the synthesis of proteins, RNA polymerases transcribe DNA to mRNA followed by translation of mRNA to amino acids in the ribosomes. After synthesis, the resulting

proteins are folded to the final three-dimensional structure. The diversity of proteins is a result of the protein size (up to 34,000 amino acids; more than 1 μm length) and the presence of four structural levels.⁶³ The sequence (primary structure) can be folded to α -helix or β -sheet (secondary structure), linked by cystine and hydrogen bonding (tertiary structure), and multiple sequences (quaternary structure) can be arranged. The last function-influencing structures are post-translational modifications, for example phosphorylation.⁶⁴ An example of a folded protein structure of human fatty acid synthase obtained by XRD is shown in Figure 6.

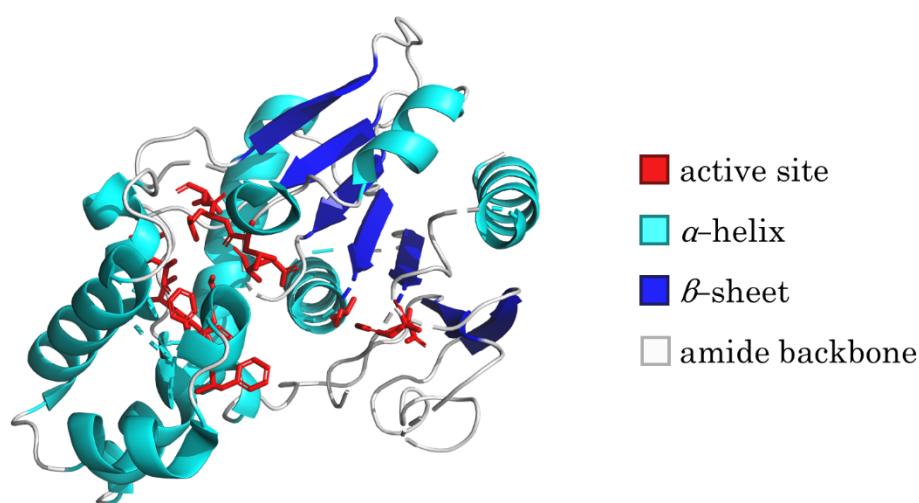


Figure 6. Human fatty acid synthase crystal X-ray structure with the active site in red, α -helices in cyan, β -sheets in blue, and the amide backbone in white.⁶⁵

The protein structures in MS experiments can be influenced by the ionization method. Proteins stay near their native form in buffered solutions, while adding acid or tailored reagents leads to unfolding of the proteins.^{66,67} The following identification of the structures requires a combination of MS² approaches, which tackle the different structural features.

Tandem mass spectrometry

To expand the application possibilities of MS in structural analysis, new strategies were developed, using fragmentation of precursor ions.^{35,68} Fragmentation of molecular ions by collision with inert-gas molecules/atoms, so-called collision-induced dissociation / higher-energy C-trap dissociation (CID / HCD), is most widely used.^{69,70} In CID, transferred kinetic energies of the collisions differ, but are typically 10 kJ mol^{-1} .⁷¹ Between collisions, the energy which was introduced into the analyte equilibrates within the heat bath of the internal degrees of freedom heating the analyte ion. Upon consecutive gas collisions, the energy of the system is increased above the dissociation threshold, resulting in fragment ion formation (Figure 7).

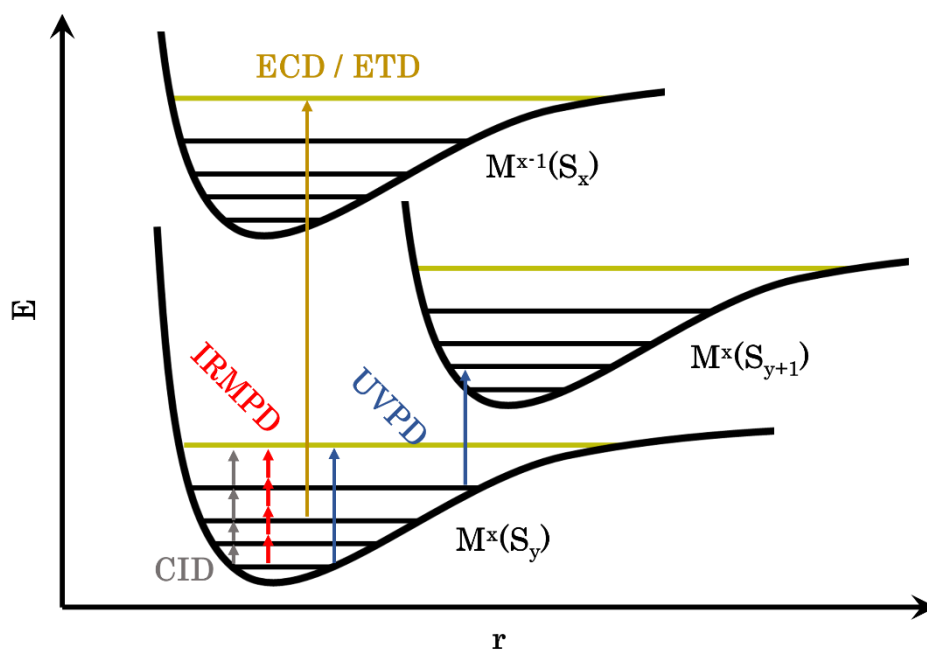


Figure 7. Jablonski diagram showing the energy (E) and the interatomic distance of the excitation using collision-induced dissociation (CID; grey), infrared multiple photon dissociation (IRMPD; red), ultraviolet photodissociation (UVPD; blue), or electron-capture dissociation / electron-transfer dissociation (ECD, ETD; brown). Vibronic energy levels are represented by black lines, dissociative vibronic levels are shown in green.

In contrast to CID, energy is introduced by capturing or transferring electrons in electron-capture dissociation (ECD) and electron-transfer dissociation (ETD).^{72,73} Formation of radical molecules potentially leads to direct cleavage of bonds. Preferentially, radicals are rearranged, which finally leads to cleavage of

molecules.⁷⁴ However, in the positive-ion mode, the loss of a charge requires the presence of multiply charged precursor ions, in the negative-ion mode, electron capturing becomes less likely with increasing charge states. Instead of collisions or electrons, photons can be used for the excitation of ions. In infrared multiphoton dissociation (IRMPD), cumulative low energy excitation leads to fragmentation, similar to CID. Differences of IRMPD to CID are the absorption of the energy by capturing photons instead of inert-gas collisions and the well-defined amounts of energy per photon.⁷⁵ Due to the excitation of vibrational modes in the IR range of the electromagnetic spectrum, the absorption efficiency is wavelength dependent. According to the wavelength, relative fragment ion intensities are increased or decreased. Therefore, IR spectra can be recorded, when the fragmentation yield is tracked as a function of the IR wavelength in IRMPD.⁷⁶ Ultraviolet photodissociation (UVPD) irradiates the analyte with UV instead of IR photons. The higher amount of energy per photon in UV compared to IR potentially leads to instant cleavage of bonds. The dissociation can occur following different energetic pathways (Figure 8).

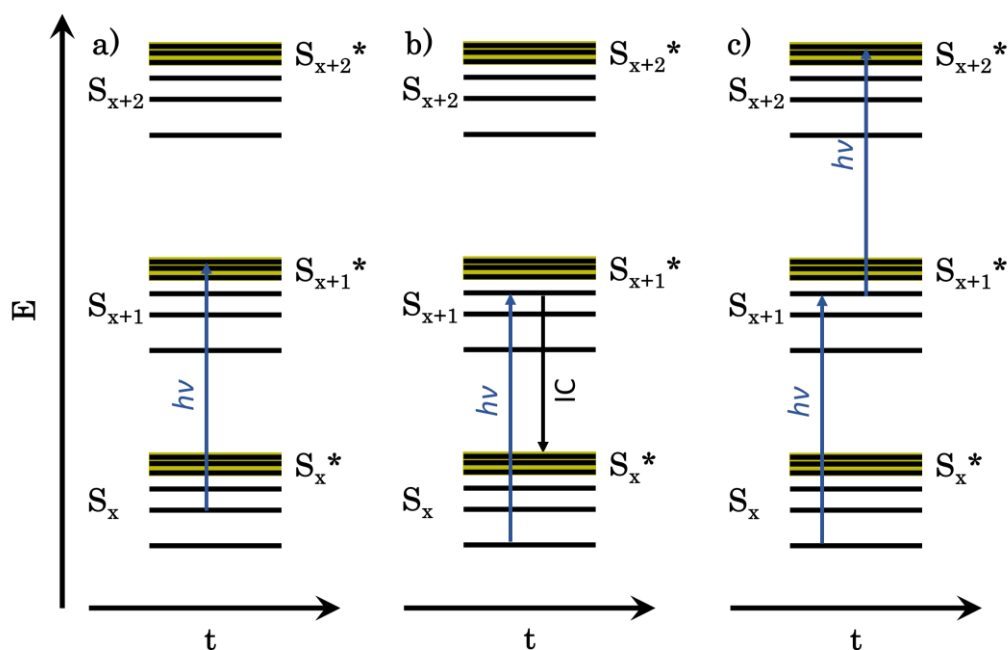


Figure 8. Examples of schematic energy/time diagrams for the photodissociation models using UV excitation. a) Direct cleavage by single photon absorption, b) intersystem crossing (IC), or c) multiphoton absorption can lead to fragmentation.

Absorption of UV photons potentially leads to direct excitation to a dissociative vibronic state and cleavage in femtoseconds.^{77,78} Another possible energetic path is electronic excitation, followed by intersystem crossing (IC) to a dissociative vibronic level of lower electronic states in femto- to picoseconds.⁷⁹ Bond cleavage can also occur by the absorption of multiple photons. Therefore, the energy cannot equilibrate to the internal degrees of freedom of the analyte ion. This opens the possibility to selectively cleave bonds next to a chromophore, so-called radical-directed dissociation (RDD).⁸⁰ Phenylic C-I bonds are promising candidates for the introduction of a localized radical.⁸¹ Phenyl groups absorb UV photons and the resulting radical is trapped in the σ orbital.^{82,83} The group of Julian used this characteristics of phenylic C-I bonds to analyze protein structures, by functionalizing tyrosine to iodo-tyrosine in an RDD approach.⁸⁴

Biological application of tandem mass spectrometry

The composition of biologically relevant molecules ranges from small molecules like metabolites (*e.g.* ethanol), to macromolecules like lipids or proteins.^{85–87} For example, headgroups of lipids are routinely identified using CID combined with database search.⁸⁸ But pinpointing structural elements such as the FA identity, require more sophisticated approaches. DB positions in FAs, for example, can be unraveled using ozone-induced dissociation (OzID), Paternò-Büchi (PB) reactions followed by CID or UVPD or UVPD without prior PB functionalization (Figure 9).^{89–91}

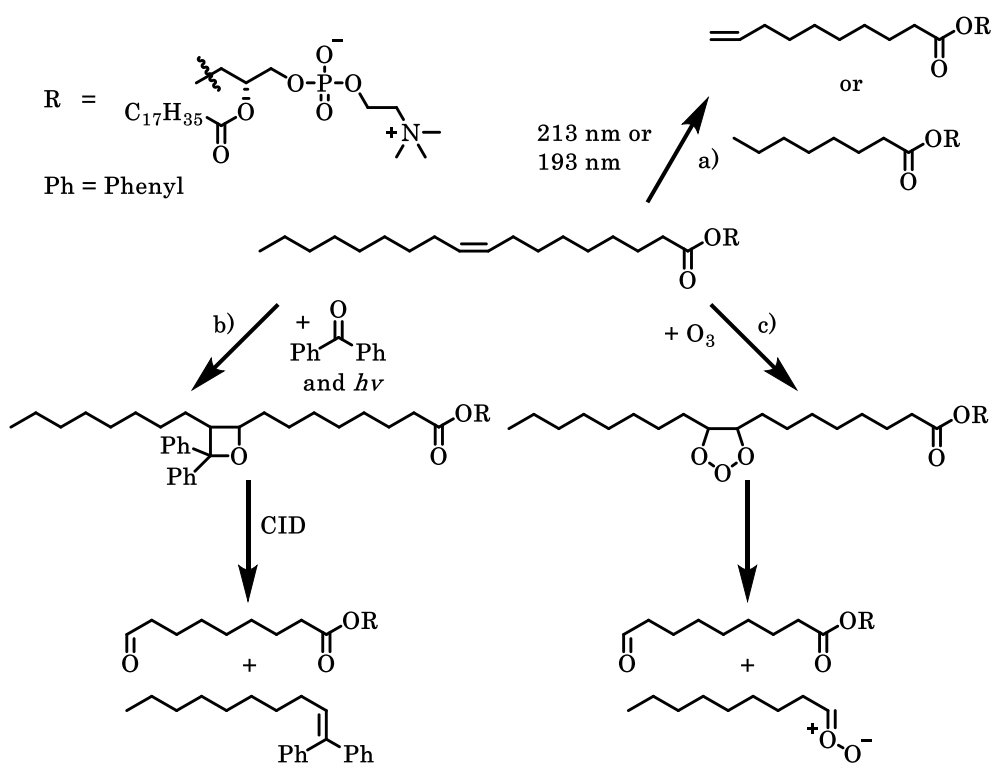


Figure 9. Double-bond-position localization by a) ultraviolet photodissociation (UVPD), b) Paternò-Büchi (PB), and c) ozone-induced dissociation (OzID) on the example of POPC.

However, the identification of *sn*-isomerism remains challenging. Previous methods used the selectivity of enzymatic cleavage in phosphatidylcholines (PCs) followed by product identification, for example using MS.^{92,93} Thao *et al.* showed that *sn*-isomerism can be unraveled using OzID.⁹⁴ The group of Brodbelt developed a HCD-UVPD workflow based on a fragmentation mechanism, which was proposed by Turk and coworkers.⁹⁵ Turk proposed a mechanism in which a 1,3-dioxolane derivative is formed, which Brodbelt and coworkers created in HCD, followed by selective cleavage in *sn*-2 position by UVPD by the Brodbelt group.^{91,96}

Identification of post-translational modifications is challenging with proteomics approaches. The development of mass analyzers with increasing resolution and new MS² methods allow to overcome this shortcoming in top-down approaches. For example, protein tertiary and quaternary structures can be investigated using cross-linking experiments. A crosslinker consists of two reactive ends, typically primary amines, sulfhydryls, carboxylic acids, connected by a spacer, which can be MS cleavable.^{97,98} If the distance defined by the spacer is present in-between two amino acids, specific mass tags can be detected in MS² experiments. Tertiary and

quaternary structures of proteins can also be probed using hydrogen–deuterium exchange.⁹⁹ The analytes are solved in deuterated solvents, and if the proton interacts with the solvent, protons can be exchanged with deuterium and *vice versa*.¹⁰⁰ This exchange results in a change in the mass of fragments created in MS² experiments and can therefore be tracked.

Ionization in mass spectrometry

Gas-phase structures, charge states, and in-source fragmentation are just a few examples of influences on lipids and proteins caused by the ionization method. “Hard” ionization techniques such as electron ionization, chemical ionization, laser desorption/ionization, or secondary ion mass spectrometry typically lead to dissociation of larger (bio-)molecules.^{101–106} Therefore, the invention of “soft” ionization techniques started a new era in the investigation of large biomolecules with MS. The development of matrix-assisted laser desorption/ionization (MALDI) and electrospray ionization (ESI) were awarded with the Noble prize in chemistry in 2002.¹⁰⁷ In MALDI, the laser indirectly ionizes the analyte molecules solved or covered in/by matrix crystals.^{108,109} Energy of laser photons is absorbed by the matrix and afterwards transferred to the analytes, resulting in their ionization. The sample is desorbed by a laser-induced explosion. The so-formed ions can be analyzed using MS. ESI allows the analysis of molecules from solution, by applying high voltages on liquids, which are typically scattered by gas to accelerate the evaporation of the solvent.^{110,111}

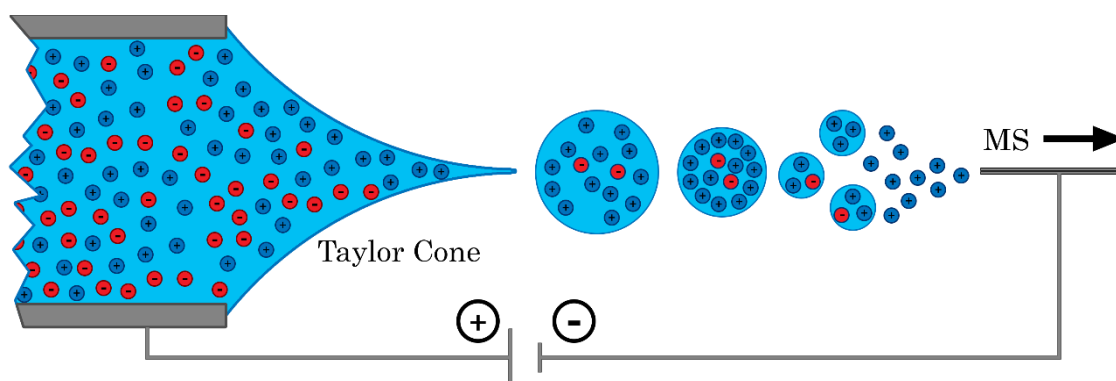


Figure 10. Scheme of an ESI source in positive-ion mode. Anions and cations are shown in red and dark blue, respectively. Solvents are colored light blue.

After the release by the Taylor cone, ions are captured in solvent droplets.¹¹² The size of the droplets is consequently reduced by evaporation of the solvent (Figure 10), resulting in an increase of repulsive Coulomb forces. When the droplets surface tension gets smaller than the Coulomb repulsion the droplet ruptures (Rayleigh limit).^{113,114} Smaller droplets are formed and the process of evaporation starts again. The final step before the evaporation of solvent-free ions was explained by two mechanisms in literature. The ion evaporation model suggests field desorption of ions from the droplet surface.^{115,116} The competing theory is called charge residue model. It suggests that droplets rupture and solvent evaporation goes on until only one analyte is left in the droplet and finally released when the whole solvent evaporates.¹¹⁷

Mass analyzers

After ionization, the analytes are transferred to mass analyzers to determine the m/z ratio. Historically, magnetic or electric sector fields were used but modern instruments mainly contain time-of-flight, quadrupole, FT-ICR, or orbital trapping mass analyzers.^{101,118–121} The resolution and the accuracy of mass analyzers are their figures of merit. The accuracy in ppm is given by equation 1 with the accuracy ($\frac{\delta m}{m}$), the accurate mass value (m) and the exact mass value (m_{exact}). The accuracy can be calibrated using a solution of known compounds.

$$\frac{\delta m}{m} = \frac{m - m_{exact}}{m_{exact}} \cdot 10^6 \quad (1)$$

The resolution (R) is analyzer-specific and depends on the m/z signal and the signal width at half maximum ($\Delta m/z$) (equation 2).¹²²

$$R = \frac{m}{\Delta \frac{m}{z}} \quad (2)$$

The development of high-resolution mass spectrometers-, such as Fourier-transform ion cyclotron resonance mass spectrometers (FT-ICR-MS) and orbital trapping analyzers allow to analyze the elemental composition of analytes by the atomic mass defect. Accuracies lower than 2 ppm with R up to 1,000,000 are achieved on a routine basis.^{120,121}

The advantage of FT-ICR-MS is the independence of the mass resolution of the kinetic energy of the ion (equation 3).

$$f_c = \frac{zB}{2\pi m} \quad (3)$$

The cyclotron frequency (f_c), depends on the charge number (z), the magnetic field strength (B), and the mass (m) of the ion. With B constant for the superconducting magnet, the m/z ratios of the ions are independent from any influence but the cyclotron frequency. Experimentally, radio frequencies are applied by excitation plates to stimulate the ions (Figure 11).¹²³ If the cyclotron frequency equals the excitation frequency, the radii of the ion motion are extended and they induce a current in the detector plates, which can be recorded and transformed to m/z values by Fourier-transformation. High resolution analyzers like FT-ICR-MS allow direct identification of elemental compositions according to the element's mass defect and isotopic distribution.

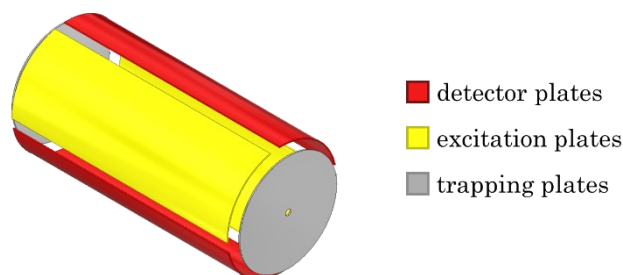


Figure 11. Schematic picture of an ICR cell with the detector (red), excitation (yellow), and trapping (grey) plates.

Computational chemistry

The increasing availability of MS led to the description of multiple dissociation mechanisms in gas-phase chemistry. For example, the McLafferty rearrangement, where β -cleavage of hydrocarbons is induced by keto groups or the oxazolone pathway in protein fragmentation.^{124,125} Due to the ultra-high vacuum in MS, isolated gas-phase molecules can be investigated. The lack of interactions with solvent or matrix molecules benefits the comparison of experimental data with density-functional theory (DFT) calculations.¹²⁶ The low molecular density in mass analyzers, however, prevents conventional IR spectroscopy. This was overcome by the wavelength-tunable free-electron lasers (FELs) in IRMPD experiments.^{127–129} The photoproduct yield (*PY*) in IRMPD depends on the absorption, therefore IR spectra can be generated by monitoring the wavelength dependency of the *PY*.¹³⁰ Instead of monitoring the *PY* it is also possible to trap and cool ions in superfluidic helium droplets.¹³¹ If they are excited by FELs, the Helium evaporates, until the ion is released from the droplet. The wavelength-dependent evaporation efficiency yields IR spectra at 0.4 K in MS. Cooling of the ions sharpens the IR bands by freezing of rotational conformers.

New computational models for chemistry are constantly developed. The early ab-initio self-consistent field method by Hartree and Fock (HF) uses a static mean field of the electrons.^{132,133} By using a single Slater determinant HF methods neglect correlations between the electrons, *e.g.* Coulomb forces.¹³⁴ This approximation reduces computational costs, but limits the accuracy to the so-called Hartree-Fock-Limit.¹³⁵ The development of computer hardware, more effective algorithms, and integrated software solutions fueled theoretical investigations of molecular systems.¹³⁶ Computationally more costly post-Hartree-Fock methods, for example the Møller-Plesset method, were developed, which added electron correlation to the Hartree-Fock method.¹³⁷ However, compromising between computational cost and improvement of the results is an important consideration to be made. DFT approaches dramatically decreased computational costs compared to post-HF methods, while yielding energetic accuracy comparable to experiment.^{138,139} In contrast to HF and post-HF, DFT uses spatially dependent

electron densities for solving the Schrödinger equation.¹⁴⁰ Therefore, in DFT corrections need to be applied for example if dispersion plays a major role in the investigated systems.¹⁴¹ Hybrid functionals such as the Becke 3-parameter, Lee–Yang–Parr (B3LYP) combine DFT with partly HF Kohn-Sham orbitals.^{142–145}

Accuracy of the calculations and their computational cost do not only depend on the method, but also the electronic wave functions taken into account.¹⁴⁶ Single-electron wavefunctions are given by the theory, for example Slater-type (STO), Gaussian-type (GTO), or numerical atomic orbitals (NAO).^{147–151} STOs are the solution of the Schrödinger equation in a single electron system, but the exact calculation of STOs is computationally costly. The computationally less demanding GTOs are approximations of Gaussian functions to the STOs. Linear combination of these atomic orbitals is the simplest way of estimating molecular orbitals.

The acceleration of the calculations using GTOs compared to STOs and NAOs is important, since this is the rate-determining step in most calculations.^{152,153} Therefore, GTOs are most widely used in modern computational chemistry. Examples are the Pople 6-311G series, Dunning's correlation consistent cc-pVXZ series, or Jensen's polarization consistent pc-n series.^{154–158}

Aim of this work

Structural analysis of peptides, proteins and lipids remains one of the biggest challenges in mass spectrometry. However, their structural features are highly relevant because they determine their biological functionality.

One of the emerging mass spectrometric methods that holds the promise to achieve complete structural characterization of biomolecules due to the use of UV laser photons, is UVPD. The aim of this work is to contribute to the understanding and bioanalytical capabilities of UVPD. For this purpose, current challenges in MS-based proteomics and lipidomics are used as models to obtain mechanistic insights and reveal drawbacks of UVPD in bioanalytical mass spectrometry. Specific fragment ion structures and mechanisms associated with structure-selective fragmentation of lipid and protein ions are investigated.

The selective cleavage of GP *sn*-positions are targeted by introducing energetic differences between the cleavage of *sn*-1 and *sn*-2 esters by adding metal ions to the gas-phase structures. Therefore, [GP+M]^{1+/2+} ions are screened using 213 nm UVPD, HCD, and CID on an FT-ICR MS (LTQ FT Ultra, Thermo Fisher Scientific, Bremen, Germany) equipped with a laser (Tempest, New Wave Research, Portland, USA) for UVPD and an orbital trapping mass spectrometer (Q Exactive, Thermo Fisher Scientific GmbH, Bremen, Germany) for HCD.¹⁵⁹

The selectivity of cleavage in *sn*-2 position is validated by comparing relative fragment-ion intensities of both possible fragments (cleavage in *sn*-1 and *sn*-2) to literature and *sn*-2 selective enzymatic digestion using PLA₂. The performance of UVPD is further compared to CID and HCD and limits of detection are investigated. Using relative quantification of standard substances for calibration, egg yolk, porcine brain, yeast, and mouse pancreas lipid extracts are analyzed. Following up the findings of metal-lipid adducts, the fragmentation mechanism and the influence of the cations on the GP gas-phase structures are investigated in detail. Therefore, IRMPD spectra of [GP+M]^{1+/2+} ions are analyzed and compared to theoretical vibrational spectra.

To expand the knowledge about the capabilities of UVPD in proteomics, the influence of the protein charge state on the fragmentation is investigated. For this purpose, the model proteins ubiquitin, cytochrome c and myoglobin are investigated. Numbers of charge carriers attached to the proteins are manipulated using buffered solution, denaturing solution, and adding supercharging reagents to the ESI spray solvent. A home-built algorithm is used to analyze the protein data without prior deconvolution to a spectrum containing only singly charged monoisotopic signals. The number of trapped ions, the mass resolution, the number of averaged spectra, and the number of laser pulses per spectrum were kept constant to avoid influences on the fragmentation. Identifying the influence of the charge carrier positions, the experimental results are compared to Monte Carlo-type 'pseudo-random walk' calculations.¹⁶⁰

Results and Discussion

*Relative Quantification of Phosphatidylcholine *sn*-Isomers Using Positive Doubly Charged Lipid-Metal Ion Complexes (Publication 3)*

We found that doubly charged lipid-metal complexes of PCs, phosphatidylethanolamines (PEs), and phosphatidylserines (PSs) form during ESI when adding 20 mol% MCl_2 ($M = Mg, Sr, Ba, Mn, Fe, Co, Cu, Zn, \text{ or } Sn$) to 10-100 μM GP solutions in methanol.¹⁶¹ In contrast to singly-charged lipid-metal complexes, fragmentation of these lipids resulted in selective cleavages of the FA in *sn*-2 position (Figure 12). Best signal intensities were achieved for PCs, but fragmentation of PE and PS metal adducts also yielded selective cleavage of the *sn*-2 position. DB-related fragments reported for 193 nm on the orbital trapping mass spectrometer were not detected in 213 nm UVPD.¹⁶² This is likely a result of the limited sensitivity of the instrument compared to Orbitrap MS, lower absorption of the DB at 213 nm compared to 193 nm, and the absence of collisional cooling in FT-ICR-MS ($2 \cdot 10^{-10}$ mbar) compared to the HCD-cell ($5 \cdot 10^{-5}$ mbar).

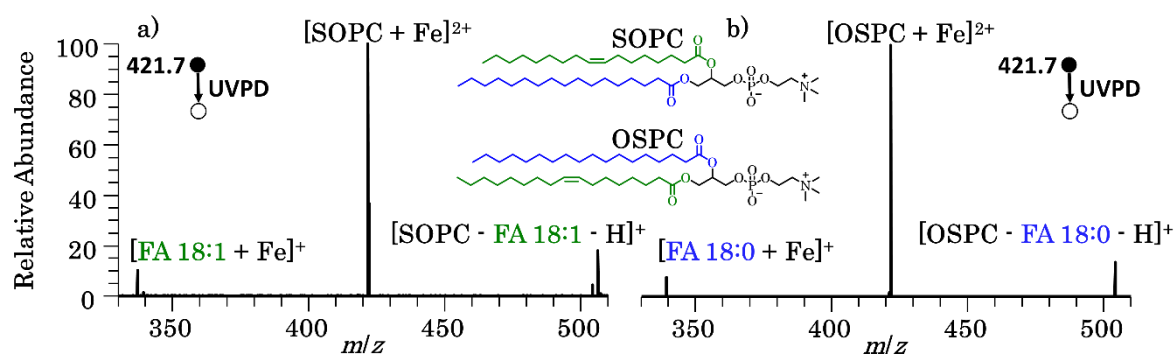


Figure 12. Positive-ion mode ESI-UVPD spectra of a) PC 18:0/18:1(9Z) (SOPC) and b) PC 18:1(9Z)/18:0 (OSPC). FAs in *sn*-2 position are highlighted in green (FA 18:1) and blue (FA 18:0).

Cleavage of the FA in *sn*-2 position of $[PC+M]^{2+}$ most likely resulted in cyclisation of the phosphate group (Figure 13). These fragments were unique for doubly charged precursor ions. The selectivity of the method therefore was determined by the affinity of the metal to coordinate towards the *sn*-1 or the *sn*-2 ester. If the energy introduced by CID/HCD/UVPD was higher than E_a of cleavage in *sn*-1 and *sn*-2 position, a decrease of the selectivity was expected.

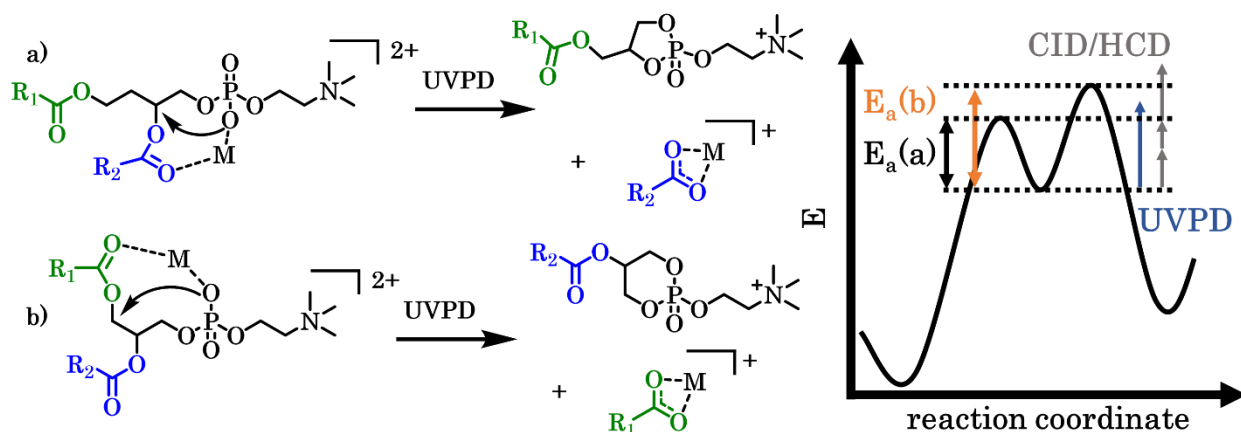


Figure 13. Proposed fragmentation mechanisms for the selective cleavage in a) *sn*-2 and b) *sn*-1 position of $[PC+M]^{2+}$ complexes and the energy diagrams of the dissociation.

This hypothesis was supported by our data because we found that the *sn*-selectivity of the cleavage depends on the fragmentation method. Mean absolute deviations (MDs) determined using PLA₂ digestion as reference of *sn*-impurity of authentic standards were 23 ± 12 for HCD, 19 ± 4 for CID, and 9 ± 4 for UVPD. We conclude that the higher collision energies in HCD compared to CID make higher energy fragmentation pathways available. UVPD on the other hand introduces a well-defined amount of energy per photon to the molecules, leading to the highest *sn*-selectivity.

The development of a method for the *sn*-selective cleavage contributed to the toolbox of lipid analysis. We showed that fragment ion intensities correlate to the abundance of *sn*-isomers in standard substances. By applying the method to lipid extracts, we demonstrated the robustness of the UVPD method for the relative quantification of lipids in complex mixtures without standard substances. Moreover, the method can easily be implemented to any shotgun ESI-MS/MS setup in standard lipidomics workflows.

IRMPD Spectroscopy of $[PC(4:0/4:0) + M]^+$ ($M = H, Na, K$) and Corresponding CID Fragment Ions (Publication 4)

In order to rationalize *sn*-selectivity of tandem MS methods, we next intended to characterize fragment ion structure, fragmentation energetics, and fragmentation pathways. For this purpose, we commenced with singly charged ions of PCs. Fragmentation of $[PC+M]^+$ ($M = Li, Na, K$) species resulted in cleavage of the headgroup. The fragmentation could either be a result of a nucleophilic attack of the *sn*-1 or the *sn*-2 ester to the *sn*-3 position. Attack of the *sn*-1 would result in a six-membered (dioxane) ring, while cyclization involving the *sn*-2 ester results in a five-membered (dioxolane) ring (Figure 14). Using deuterated species Hsu *et al.* proposed that the oxolane species is present in the experiments.¹⁶³ The group of Brodbelt developed a HCD-UVPD workflow for lipid-sodium adducts based on the oxolane species.⁹¹ Using the same intermediate dioxolane structures, lithium and silver(I) were used for discrimination of lipid *sn*-isomers and DB positions in CID experiments.^{95,164} However, these *sn*-selective methods strongly rely on the selectivity of the formation of a dioxolane-intermediate, which was not spectroscopically identified.

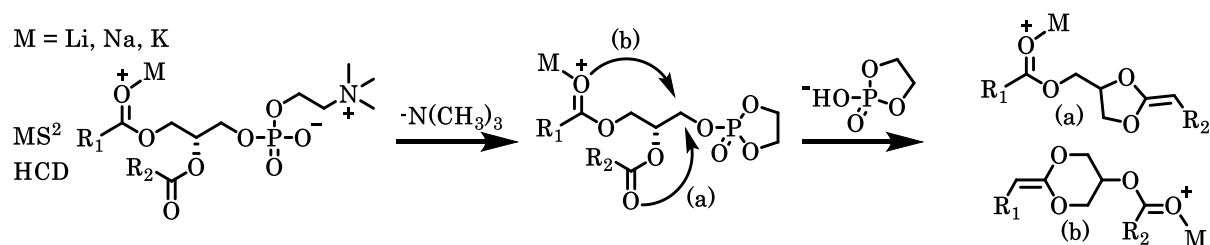


Figure 14. Proposed mechanism for the loss of PC headgroups in CID experiments by Turk *et al.*, yielding (a) five- (dioxolane) or (b) six-membered (dioxane) rings.¹⁶³

To investigate the gas-phase structure of these lipid ions, we investigated ESI sprayed $[PC(4:0/4:0) + M]^+$ ($M = H, Na, K$) species and the fragments assigned to headgroup loss $[PC(4:0/4:0) + Na/K - 183]^+$ using IRMPD spectroscopy. To assign the spectroscopic bands to vibrational modes, the spectra were compared to the theory using B3LYP/pc-1.¹⁶⁵ We found that spectra of the protonated PC differed from those of the alkali metal complexed ones. While the conformational isomers of the predicted $[PC(4:0/4:0) + H]^+$ structures were all within $2 \text{ kJ} \cdot \text{mol}^{-1}$ of each other, the alkali metals preferably coordinated towards the phosphate and the *sn*-1

ester with more than $15 \text{ kJ} \cdot \text{mol}^{-1}$ compared to coordination towards the *sn*-2 ester. The higher energetic differences between the isomers of Na^+ and K^+ indicated less conformational conversion compared to H^+ , which leads to preferred presence of the isomers that sterically hinder the *sn*-1 ester to attack the *sn*-3 position. Acetal-like signals were found in the fragment ion IRMPD spectra, hinting towards the formation of a dioxolane or dioxane structure. The calculated bands of the dioxolane derivatives fitted the experiment better than the dioxane. Therefore, the alkali-metal-mediated orientation within the precursor structure most likely facilitated a nucleophilic attack of the *sn*-2 ester resulting in the formation of dioxolane derivatives.

Next, we performed IRMPD spectroscopic investigations of $[\text{PC } 4:0/4:0 + \text{Fe}]^{2+}$. Vibrational bands of the doubly charged iron adduct were strongly shifted compared to $[\text{PC } 4:0/4:0 + \text{H}/\text{Na}/\text{K}]^+$ (Figure 15).

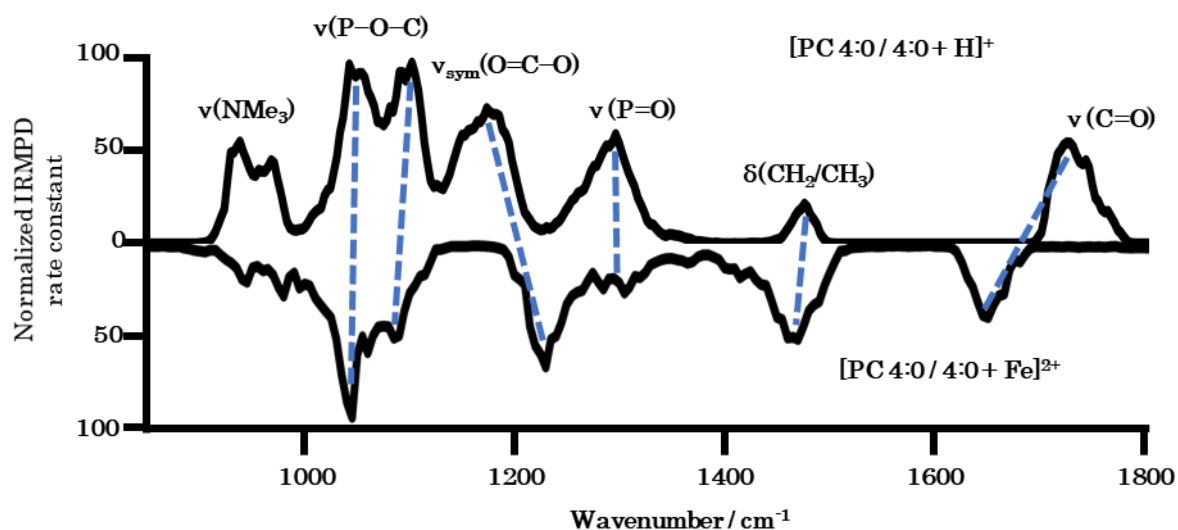


Figure 15. IRMPD spectra of $[\text{PC } 4:0/4:0 + \text{H}]^+$ and $[\text{PC } 4:0/4:0 + \text{Fe}]^{2+}$. Bands are assigned based on Publication 4.¹⁶⁵ As a guide to the eye, bands assigned to the same mode are connected by dashed blue lines.

The spectrum of $[\text{PC } 4:0/4:0 + \text{Fe}]^{2+}$ showed similar positions of bands assigned to phosphate, hydrocarbon and NMe_3 groups. In contrast to results for singly charged $\text{PC } 4:0/4:0$ ions, the bands assigned to ester modes were red- ($\nu_{\text{sym}}(\text{O}=\text{C}-\text{O})$) and blue-shifted ($\nu(\text{C}=\text{O})$) by roughly 100 cm^{-1} compared to the protonated, sodiated and potassiated structures. As described in publication 4, shifts of vibrational bands indicated pronounced interactions between metal ions and functional groups

within the lipid.¹⁶⁵ Therefore, our findings indicated stronger interactions of the iron(II) ions with the esters compared to H⁺, Na⁺, and K⁺. The increase of interactions compared to the singly charged species as well as the increased charge of the doubly charged ion compared to [PC (4:0/4:0) + M]⁺ ions potentially activated the precursors and resulted in the mechanism shown in Figure 13 and discussed in Publication 3.¹⁶¹ The spectroscopic data support that Fe²⁺ coordinated stronger to the ester bonds compared to H⁺, Na⁺, and K⁺. This has two effects, the glycerol *sn*-2 position got more nucleophilic, favoring a nucleophilic attack of the phosphate and the attack of the ester to the *sn*-3 position was blocked. This finding explained the presence of different fragmentation mechanisms in iron(II) compared to alkali metal-lipid adducts.

Influence of Protein Ion Charge State on 213 nm Top-Down UVPD (Publication 5)

In addition to the increasing interest in UVPD for lipidomics, multiple studies showed the benefits of the method in top-down proteomics.^{166–168} In contrast to collisional and electron activation, the protein fragmentation mechanism occurring upon UVPD was not well understood.^{169,170} To shed light on the influence of the charge location and quantity on UVPD fragmentation, we investigated UVPD on the model proteins ubiquitin, cytochrome c, and myoglobin.¹⁷¹ To manipulate the numbers of charge states per protein, buffered solution (low), denaturing solution (medium), and supercharging reagents (high) were added to the ESI solvent. The photoproduct yields and the sequence coverages increased with increasing charge states for all proteins. Comparison with calculations of charge carrier positions showed that cleavage preferentially occurred, if the amide bond was protonated or in-between two protonated amide bonds. Therefore, we concluded that there are two processes determining the fragmentation site, a) a charge-induced dissociation, similar to CID results, and b) charge-remote fragmentation that was driven by repulsive Coulomb forces.

Systematic investigation of protein UVPD experiments can help to interpret top-down proteomics data. Our findings contribute to the understanding of differences in sequence coverage found for UVPD compared to CID, HCD, ETD, and ECD by giving insights into the fragmentation mechanism.¹⁷²

For the analysis of the data, only terminal fragments were considered. However, 10 to 40 laser pulses per spectrum were used to increase the fragmentation efficiency. Therefore, fragments resulting from earlier laser pulses were prone to be further fragmented, resulting in internal fragments. In collaboration with Susannah Brown, analyses of the internal fragments were performed (Figure 16).

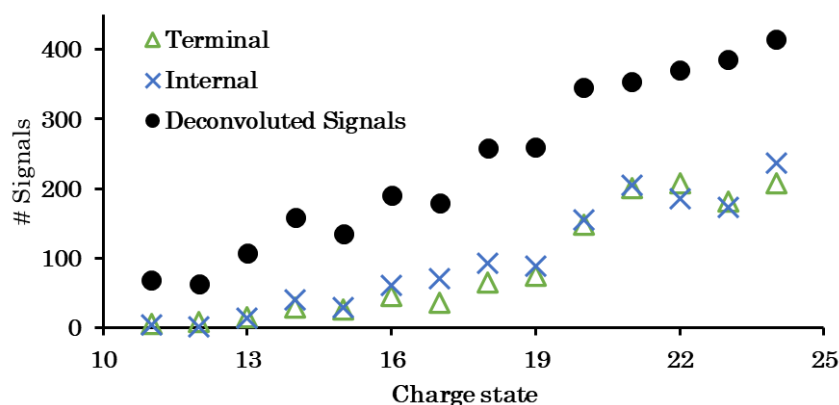


Figure 16. Fragment signals of cytochrome c as a function of precursor charge state. Terminal, internal and overall deconvoluted signals are color-coded green, blue and black, respectively.

We found that the number of internal fragments was in the range of that of terminal fragments when performing experiments with 20 pulses per spectrum on cytochrome c. In good agreement with data of Publication 3, the fragmentation increased with the charge state.

Publication 3 extends the toolset of analytical chemists. Adding metal-salts as the only requirement without the need for instrumental modifications, makes the method widely applicable. The gas-phase structures discussed in publication 4 show the influence of the precursor conformation on the fragmentation. Signals correlating with the presence of a dioxolane species support the mechanisms proposed in the literature. The first study on the influence of charge carrier quantity and position showed that charge carriers directly influence the fragmentation of proteins. This can be used to identify charge carrier sites using MS² data or to predict cleavage sites of proteins in MS² experiments.

Outlook

Further investigations using UVPD were carried out and showed the high potential of the method for the analysis of biomolecules. First experiments and their interpretation should be followed by extended investigations to deepen the understanding of UVPD and to develop novel structure-sensitive MSⁿ workflows.

In addition to the *sn*-selective cleavage observed for PCs, PEs, and PSs, we found that fragmentation of [PE + Fe]²⁺ and [PS + Fe]²⁺ resulted in fragments with a series of (CH₂)_n-loss in UVPD, CID, and HCD experiments. To investigate the origin of this process, HCD experiments were conducted because they yielded the highest fragment-ion intensities. Interestingly, comparison of PE 18:0/18:1 and PE 18:0/18:0 showed that the observed dissociation channels are unique in unsaturated FAs (Figure 17).

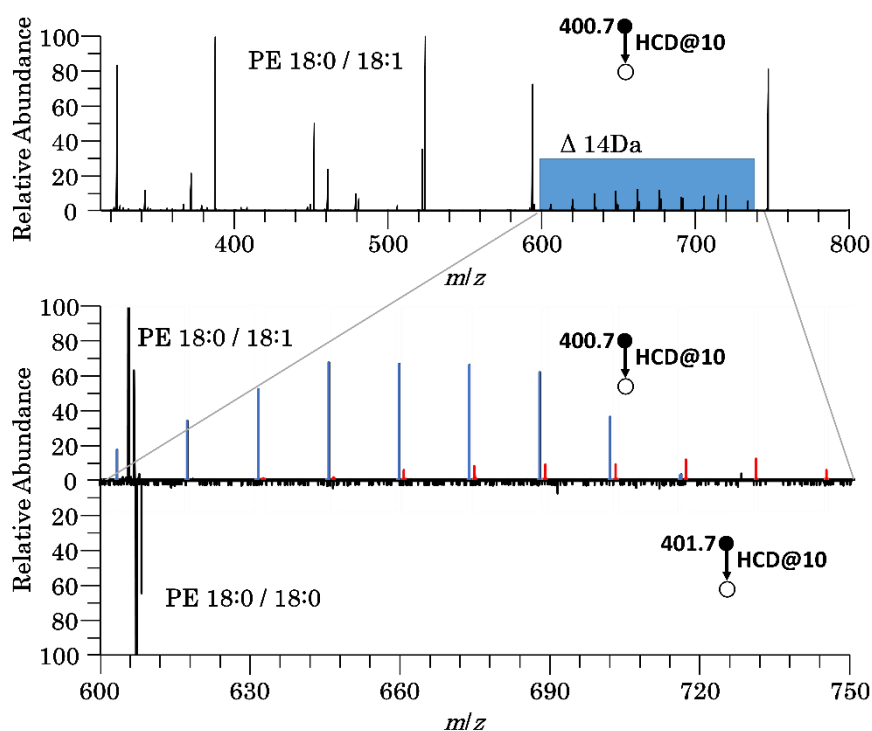


Figure 17. MS² spectra of PE 18:0/18:1 and 18:0/18:0. Signals colored in blue and red are separated by 14 Da each.

This finding was confirmed in experiments with unsaturated deuterated lipids (Figure 18). The (CH₂)_n-losses were unique for the FA containing the DB, resulting

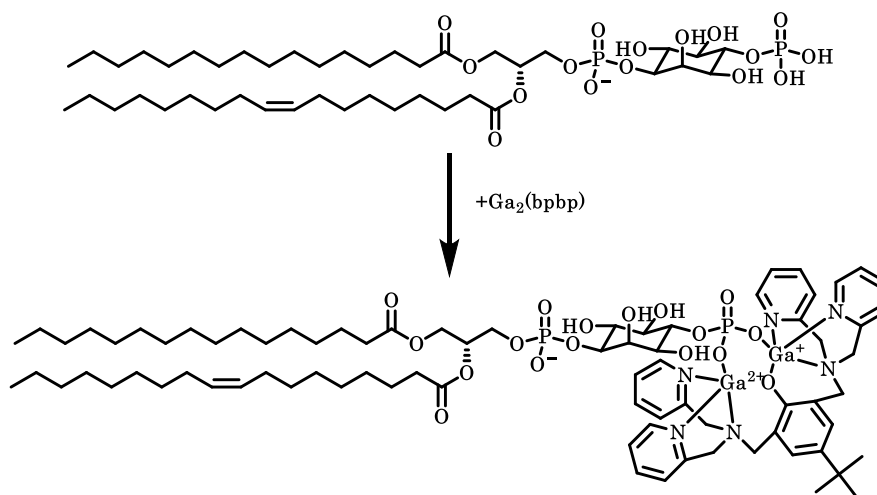


Figure 19. Reaction of phosphatidylinositol-4-phosphate with the digallium complex $\text{Ga}_2(\text{bppb})$.

Attachment of $\text{Ga}_2(\text{bppb})$ to PIs was successfully performed. The introduced chromophores made PI- $\text{Ga}_2(\text{bppb})$ adducts interesting candidates for UVPD. However, UVPD of the species did not result in fragments indicating the phosphate position. Modifying the $\text{Ga}_2(\text{bppb})$ complex, for example iodination of the pyridine, introduces a UV cleavable radical starter, which potentially leads to fragments indicating the phosphorylation site. Further research on this topic is a promising approach to improve characterization methods for PIs.

Deoxysphingosines are another class of lipids, which challenge analytical chemists. They consist of aliphatic chains which can be unsaturated in several positions and numbers. Approaches to identify DBs using UV photons are direct cleavage, functionalization, or RDD.^{84,91,167,185–188} Due to the lack of DB fragments in our UVPD setup and to be specific on deoxysphingosines we developed an RDD workflow. After derivatization with 4-iodo benzaldehyde (Figure 20) the C-I bond was homolytically fissioned by UV photons.¹⁸⁹

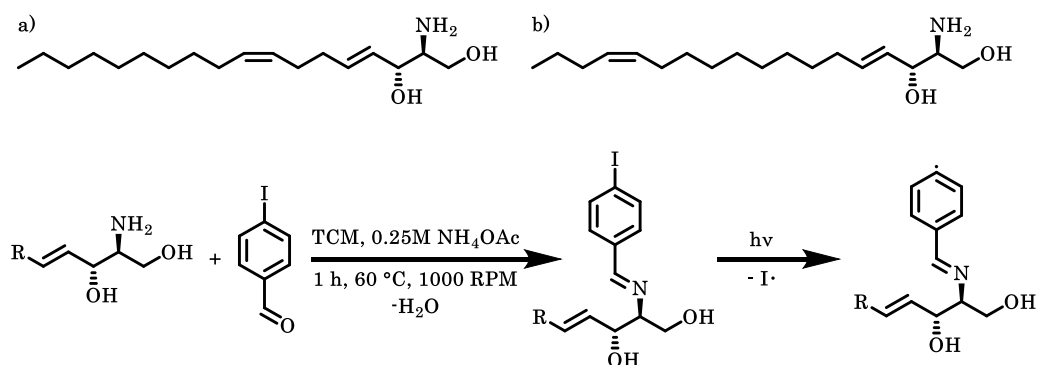


Figure 20. Structures of a) (4*E*,8*Z*)-sphingadiene and b) (4*E*,14*Z*)-sphingadiene. The reaction with the chromophore 4-iodo benzaldehyde and the activation in UVPD.

The resulting radical attacked the aliphatic chain, leading to cleavage of a series of carbon-carbon bonds by radical rearrangement. In Figure 21 the spectrum of the protonated 4-iodo benzaldehyde derivatized octadecyl amine is shown as an example.

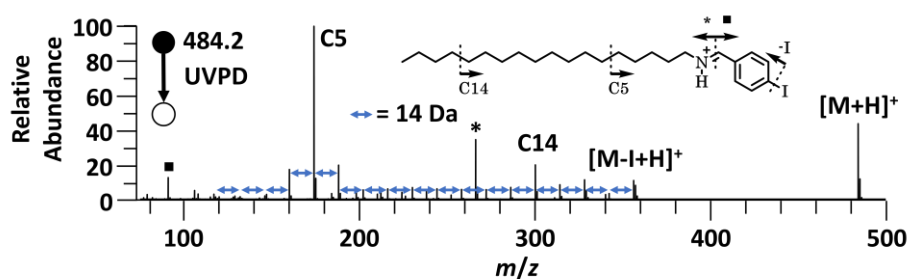


Figure 21. UVPD spectrum of the protonated 4-iodo benzaldehyde derivatized octadecyl amine. Distances of 14 Da between signals are indicated by blue arrows. Fragments in vicinity to the imine are marked by an asterisk and a square.

The signals with distances of 14 Da showed two signal intensity maxima, one near the functionalized group and a second in the aliphatic chain (the position differed corresponding to the degree and position of unsaturation). We concluded that the two signal intensity maxima were the results of two processes. On one hand there is a kinetic (steric) and on the other hand a thermodynamic effect.^{190,191} Fragment ion intensities decreased, starting from the maxima, except for vinylic positions. This local maximum can be used to identify DB positions in deoxysphingosines. Additionally, fragmentation of the DB results in a difference of 12 Da between the signals. Similar results were found for aliphatic primary amines and PEs. To use the method on lipid extracts, for example MTBE, the influence of other amine-containing lipids need to be investigated.¹⁹¹ Following the investigation of

standard substances a workflow of lipid extraction, derivatization, LS-MS/MS experiment should be applied to gain information about the DB position of the extracted lipids.

The development of novel methods allows the identification of increasing numbers of functional groups and improves MS capabilities for structural identification. For future developments, methods that are easy to use and implement are promising to have the biggest impact. The development of multifunctional reactants can help to simplify experiments and make the approaches available for a broad range of analytes.

Another crucial factor for the implementation in routine MS analysis is the combination of LC-MS with novel methods. With decreasing times per scan of the mass analyzers, the duration of the fragmentation becomes the rate-limiting step in MS². OzID, UVPD, and CID/HCD have already been shown to be feasible for LC-MS experiments.^{192,193} The reaction time (OzID) and the excitation time (CID/HCD) determine the duration of MS² measurements. UVPD requires at least the time of a single laser pulse, which is in the range of nanoseconds. The fast fragmentation permits the performance of multiple tandem-MS experiments within the timescale of a chromatographic signal. To combine the capabilities of orbital trapping MS and UVPD, a 266 nm laser was attached to an orbital trapping mass spectrometer (Q Exactive, Thermo Fisher Scientific GmbH, Bremen, Germany). First results were promising to increase the precursor isolation selectivity and the time per spectrum in UVPD-MS experiments.

To understand ion fragmentation mechanisms, gas-phase IR spectroscopy has proven to be a powerful tool for biomolecules.^{194,195} Recently, Kirschbaum *et al.* were able to record gas-phase IR spectra of GPs under cryonic conditions.¹⁹⁶ Studies of the fragments supported the findings of publication 4. According to the low temperatures of the molecules, IR bands were sharper compared to room-temperature IRMPD results.^{197,198} On the other hand, cryogenic infrared spectroscopy instruments are rarer than IRMPD setups. Promising candidates to establish infrared ion spectroscopy in routine analytical laboratories are optical parametric oscillators (OPOs). They combine high pulse powers and wavelength

tunability.¹⁹⁹ In combination with quadrupole ion trap mass spectrometers, benchtop IR ion spectroscopy instruments could be developed. This would make the technique accessible to a broad scientific community.

To gain further insight into UVPD of proteins, it is favorable to increase the number of analyzed fragments. Routine proteomics software packages focus on N- or C-terminal protein fragment ions. Multiple-fragmentation, however, also yields internal fragments, which can exceed the number of terminal fragments for some charge states.^{200,201} The information of internal fragments could be used to get a deeper understanding of influences on the fragmentation, similar to the charge state in publication 5. Several publications showed the influence of the protein structure on the fragmentation.^{202,203} Understanding basic processes could lead to tools, which assign MS fragments to structural motifs.

References

- (1) Ritgen, U. *Analytische Chemie I*; Springer Berlin Heidelberg: Berlin, Heidelberg, 2019.
- (2) Liebig, J. Ueber einen neuen Apparat zur Analyse organischer Körper, und über die Zusammensetzung einiger organischen Substanzen. *Ann. Phys. Chem.* **1831**, *97*, 1–43.
- (3) Prout, W. On the Relation Between the Specific Gravities of Bodies in Their Gaseous State And the Weights of their Atoms. *Ann. Philos.* **1815**, *6*, 321–330.
- (4) Prout, W. Correction of the Mistake in the Eassy On the Relation Between the Specific Gravities of Bodies in Their Gaseous State And the Weights of their Atoms. *Ann. Philos.* **1816**, *7*, 111–113.
- (5) Thomson, J. J. Rays of Positive Electricity. *Lond., Edinb., Dub. Philos. Mag. J. Sci.* **1910**, *19*, 424–435.
- (6) Thomson, J. J. Bakerian Lecture - Rays of positive electricity. *Proc. R. Soc. Lond. A* **1913**, *89*, 1–20.
- (7) Wien, W. *Kanalstrahlen und Ionisation bei hohen Temperaturen*, 1. Aufl.; Physik Nobelpreisträger Schriften 2; Salzwasser Verlag: Paderborn, 2012.
- (8) Costa-Fernández, J. M.; Menéndez-Miranda, M.; Bouzas-Ramos, D.; Encinar, J. R.; Sanz-Medel, A. Mass Spectrometry for the Characterization and Quantification of Engineered Inorganic Nanoparticles. *TrAC-Trend. Anal. Chem.* **2016**, *84*, 139–148.
- (9) Finehout, E. J.; Lee, K. H. An Introduction to Mass Spectrometry Applications in Biological Research. *Biochem. Mol. Biol. Educ.* **2004**, *32*, 93–100.
- (10) Harwood, L. M.; Moody, C. J. *Experimental Organic Chemistry: Principles and Practice*; Blackwell science; Blackwell Scientific Publications: New Jersey, 1989.
- (11) Sommer, S.; Fraatz, M. A.; Büttner, J.; Salem, A. A.; Rühl, M.; Zorn, H. Wild Strawberry-Like Flavor Produced by the Fungus *Wolfiporia cocos*—Identification of Character Impact Compounds by Aroma Dilution Analysis After Dynamic Headspace Extraction. *J. Agr. Food. Chem.* **2021**, *69*, 14222–14230.

- (12) McDonald, J. G.; Ivanova, P. T.; Brown, H. A. Approaches to Lipid Analysis. In *Biochemistry of Lipids, Lipoproteins and Membranes*; Neale D. Ridgway and Roger S. McLeod, Ed.; Elsevier: Amsterdam, 2016; pp 41–72.
- (13) Ali, I.; Aboul-Enein, H. Y.; Singh, P.; Singh, R.; Sharma, B. Separation of Biological Proteins by Liquid Chromatography. *Saudi Pharm. J.* **2010**, *18*, 59–73.
- (14) Yalow, R. S.; Berson, S. A. Immunoassay of Endogenous Plasma Insulin in Man. *J. Clin. Invest.* **1960**, *39*, 1157–1175.
- (15) Burnette, W. “Western Blotting”: Electrophoretic Transfer of Proteins from Sodium Dodecyl Sulfate-Polyacrylamide Gels to Unmodified Nitrocellulose and Radiographic Detection with Antibody and Radioiodinated Protein A. *Anal. Biochem.* **1981**, *112*, 195–203.
- (16) Coons, A. H.; Creech, H. J.; Jones, R. N. Immunological Properties of an Antibody Containing a Fluorescent Group. *Exp. Biol. Med.* **1941**, *47*, 200–202.
- (17) Hahn, E. L. Spin Echoes. *Phys. Rev.* **1950**, *80*, 580–594.
- (18) Moser, E.; Laistler, E.; Schmitt, F.; Kontaxis, G. Ultra-High Field NMR and MRI—The Role of Magnet Technology to Increase Sensitivity And Specificity. *Front. Phys.* **2017**, *5*, 1–15.
- (19) Rabi, I. I.; Zacharias, J. R.; Millman, S.; Kusch, P. A New Method of Measuring Nuclear Magnetic Moment. *Phys. Rev.* **1938**, *53*, 318.
- (20) Gil, M.; Samino, S.; Barrilero, R.; Correig, X. Lipid Profiling Using ¹H NMR Spectroscopy. *Methods Mol. Biol.* **2019**, *2037*, 35–47.
- (21) Li, J.; Vosegaard, T.; Guo, Z. Applications of Nuclear Magnetic Resonance in Lipid Analyses: An Emerging Powerful Tool for Lipidomics Studies. *Prog. Lipid Res.* **2017**, *68*, 37–56.
- (22) Anet, F. A. L.; Bourn, A. J. R. Nuclear Magnetic Resonance Spectral Assignments from Nuclear Overhauser Effects. *J. Am. Chem. Soc.* **1965**, *87*, 5250–5251.
- (23) Diercks, T.; Truffault, V.; Coles, M.; Millet, O. Diagonal-Free 3D/4D HN,HN-TROSY-NOESY-TROSY. *J. Am. Chem. Soc.* **2010**, *132*, 2138–2139.
- (24) Emwas, A.-H. M.; Salek, R. M.; Griffin, J. L.; Merzaban, J. NMR-Based Metabolomics in Human Disease Diagnosis: Applications, Limitations, and Recommendations. *Metabolomics* **2013**, *9*, 1048–1072.

- (25) Yu, H. Extending the Size Limit of Protein Nuclear Magnetic Resonance. *P. Natl. Acad. Sci. USA* **1999**, *96*, 332–334.
- (26) Friedrich, W.; Knipping, P.; Laue, M. Interferenzerscheinungen bei Röntgenstrahlen. *Ann. Phys. Chem.* **1913**, *346*, 971–988.
- (27) Kendrew, J. C.; Bodo, G.; Dintzis, H. M.; Parrish, R. G.; Wyckoff, H.; Phillips, D. C. A Three-Dimensional Model of the Myoglobin Molecule Obtained by X-Ray Analysis. *Nature* **1958**, *181*, 662–666.
- (28) Dubochet, J.; Knappek, E. Ups and Downs in Early Electron Cryo-Microscopy. *PLoS Biol.* **2018**, *16*, 1-4.
- (29) Cressey, D.; Callaway, E. Cryo-Electron Microscopy Wins Chemistry Nobel. *Nature* **2017**, *550*, 167.
- (30) Mulisch, M.; Welsch, U. *Romeis - Mikroskopische Technik*; Springer Berlin Heidelberg: Berlin, Heidelberg, 2015.
- (31) Domon, B.; Aebersold, R. Mass Spectrometry and Protein Analysis. *Science* **2006**, *312*, 212–217.
- (32) Lucci, P.; Saurina, J.; Núñez, O. Trends in LC-MS and LC-HRMS Analysis and Characterization of Polyphenols in Food. *TrAC-Trend. Anal. Chem.* **2017**, *88*, 1–24.
- (33) Belov, M. E.; Gorshkov, M. V.; Udseth, H. R.; Anderson, G. A.; Tolmachev, A. V.; Prior, D. C.; Harkewicz, R.; Smith, R. D. Initial Implementation of an Electrodynamic Ion Funnel with Fourier Transform Ion Cyclotron Resonance Mass Spectrometry. *J. Am. Soc. Mass Spectrom.* **2000**, *11*, 19–23.
- (34) Baker, M. Mass Spectrometry for Biologists. *Nat. Methods* **2010**, *7*, 157–161.
- (35) Heiles, S. Advanced Tandem Mass Spectrometry in Metabolomics And Lipidomics - Methods And Applications. *Anal. Bioanal. Chem.* **2021**, *12*, 668.
- (36) Chemical Abstracts Service. Scifinder. <https://scifinder-n.cas.org/> (accessed March 30, 2022).
- (37) Fahy, E.; Subramaniam, S.; Brown, H. A.; Glass, C. K.; Merrill, A. H.; Murphy, R. C.; Raetz, C. R. H.; Russell, D. W.; Seyama, Y.; Shaw, W.; *et al.* A Comprehensive Classification System for Lipids. *J. Lipid Res.* **2005**, *46*, 839–861.
- (38) Tvrzicka, E.; Kremmyda, L.-S.; Stankova, B.; Zak, A. Fatty Acids As Biocompounds: Their Role in Human Metabolism, Health And Disease - A Review.

Part 1: Classification, Dietary Sources And Biological Functions. *Biomed. Pap. Med. Fac. Univ. Palacky Olomouc Czech Repub.* **2011**, *155*, 117–130.

(39) Welte, M. A.; Gould, A. P. Lipid Droplet Functions Beyond Energy Storage. *BBA - Mol. Cell Biol. L.* **2017**, *1862*, 1260–1272.

(40) Nankai, H.; Miyazawa, M.; Kameoka, H. Biotransformation of (2Z,6Z)-Farnesol by the Plant Pathogenic Fungus *Glomerella Cingulata*. *Phytochemistry* **1998**, *47*, 1025–1028.

(41) Hishikawa, D.; Hashidate, T.; Shimizu, T.; Shindou, H. Diversity and Function of Membrane Glycerophospholipids Generated by the Remodeling Pathway in Mammalian Cells. *J. Lipid Res.* **2014**, *55*, 799–807.

(42) Shevchenko, A.; Simons, K. Lipidomics: Coming to Grips With Lipid Diversity. *Nat. Rev. Mol. Cell Bio.* **2010**, *11*, 593–598.

(43) Wenk, M. R. Lipidomics: New Tools And Applications. *Cell* **2010**, *143*, 888–895.

(44) Kimura, T.; Jennings, W.; Epan, R. M. Roles of Specific Lipid Species in the Cell And Their Molecular Mechanism. *Prog. Lipid Res.* **2016**, *62*, 75–92.

(45) Blanco, A.; Blanco, G. Lipids. *Medical Biochemistry*; Elsevier, 2017; pp 99–119.

(46) Kenar, J. A.; Moser, B. R.; List, G. R. Naturally Occurring Fatty Acids. *Fatty Acids*; Elsevier, 2017; pp 23–82.

(47) Curatolo, W. Glycolipid Function. *Biochim. Biophys. Acta* **1987**, *906*, 137–160.

(48) Grogan, D. W.; Cronan, J. E. Cyclopropane Ring Formation in Membrane Lipids of Bacteria. *Microbiol. Mol. Biol. R.* **1997**, *61*, 429–441.

(49) Moss, G. P.; Smith, P. A. S.; Tavernier, D. Glossary of Class Names of Organic Compounds And Reactivity Intermediates Based on Structure (IUPAC Recommendations 1995). *Pure Appl. Chem.* **1995**, *67*, 1307–1375.

(50) Wang, Z.; Shen, W.; Kotler, D. P.; Heshka, S.; Wielopolski, L.; Aloia, J. F.; Nelson, M. E.; Pierson, R. N.; Heymsfield, S. B. Total Body Protein: A New Cellular Level Mass And Distribution Prediction Model. *Am. J. Clin. Nutr.* **2003**, *78*, 979–984.

(51) Oosting, P. H. Signal Transmission in the Nervous System. *Nature* **1979**, *42*, 1479–1532.

- (52) Werner, F.; Grohmann, D. Evolution of Multisubunit RNA Polymerases in the Three Domains of Life. *Nat. Rev. Microbiol.* **2011**, *9*, 85–98.
- (53) Wood, R. D.; Mitchell, M.; Sgouros, J.; Lindahl, T. Human DNA Repair Genes. *Science* **2001**, *291*, 1284–1289.
- (54) Hünefeld, F. L. *Der Chemismus in der thierischen Organisation: physiologisch-chemische Untersuchungen der materiellen Veränderungen oder des Bildungslebens im thierischen Organismus, insbesondere des Blutbildungsprocesses, der Natur der Blutkörperchen und ihrer Kernchen ; ein Beitrag zur Physiologie und Heilmittellehre*, 2nd ed.; Brockhaus: Leipzig, 1840.
- (55) Blank, H. M.; Maitra, N.; Polymenis, M. Lipid Biosynthesis: When the Cell Cycle Meets Protein Synthesis? *Cell Cycle* **2017**, *16*, 905–906.
- (56) Sadekar, S.; Raymond, J.; Blankenship, R. E. Conservation of Distantly Related Membrane Proteins: Photosynthetic Reaction Centers Share a Common Structural Core. *Mol. Biol. Evol.* **2006**, *23*, 2001–2007.
- (57) Fischer, E. Einfluss der Configuration auf die Wirkung der Enzyme. *Ber. Dtsch. Chem. Ges.* **1894**, *27*, 2985–2993.
- (58) Sundaresan, V.; Abrol, R. Towards a General Model for Protein-Substrate Stereoselectivity. *Protein Sci.* **2002**, *11*, 1330–1339.
- (59) Wagner, I.; Musso, H. New Naturally Occurring Amino Acids. *Angew. Chem., Int. Ed.* **1983**, *22*, 816–828.
- (60) Smith, L. M.; Kelleher, N. L. Proteoform: A Single Term Describing Protein Complexity. *Nat. Methods* **2013**, *10*, 186–187.
- (61) Adkins, J. N.; Varnum, S. M.; Auberry, K. J.; Moore, R. J.; Angell, N. H.; Smith, R. D.; Springer, D. L.; Pounds, J. G. Toward a Human Blood Serum Proteome: Analysis by Multidimensional Separation Coupled with Mass Spectrometry. *Mol. Cell. Proteomics* **2002**, *1*, 947–955.
- (62) Graw, J. *Genetik*; Springer Berlin Heidelberg: Berlin, Heidelberg, 2020.
- (63) Labeit, S.; Kolmerer, B. Titins: Giant Proteins in Charge of Muscle Ultrastructure And Elasticity. *Science* **1995**, *270*, 293–296.
- (64) Smith, L. M.; Kelleher, N. L. Proteoforms As the Next Proteomics Currency. *Science* **2018**, *359*, 1106–1107.

- (65) Chakravarty, B.; Gu, Z.; Chirala, S. S.; Wakil, S. J.; Quiocho, F. A. Human Fatty Acid Synthase: Structure and Substrate Selectivity of the Thioesterase Domain. *P. Natl. Acad. Sci. USA* **2004**, *101*, 15567–15572.
- (66) Vivat Hannah, V.; Atmanene, C.; Zeyer, D.; van Dorsselaer, A.; Sanglier-Cianfèrani, S. Native MS: An 'ESI' Way to Support Structure- And Fragment-Based Drug Discovery. *Future Med. Chem.* **2010**, *2*, 35–50.
- (67) Konermann, L.; Metwally, H.; Duez, Q.; Peters, I. Charging And Supercharging of Proteins for Mass Spectrometry: Recent Insights Into the Mechanisms of Electrospray Ionization. *Analyst* **2019**, *144*, 6157–6171.
- (68) Sleno, L.; Volmer, D. A. Ion Activation Methods for Tandem Mass Spectrometry. *J. Mass Spectrom.* **2004**, *39*, 1091–1112.
- (69) McLuckey, S. A. Principles of Collisional Activation in Analytical Mass Spectrometry. *J. Am. Soc. Mass Spectrom.* **1992**, *3*, 599–614.
- (70) Shukla, A. K.; Futrell, J. H. Tandem Mass Spectrometry: Dissociation of Ions By Collisional Activation. *J. Mass Spectrom.* **2000**, *35*, 1069–1090.
- (71) Yinon, J. Tandem Mass Spectrometry (MS/MS) And Collision Induced Dissociation (CID) - An Introduction. In *Chemistry and Physics of Energetic Materials*; Bulusu, S. N., Ed.; Springer Netherlands: Dordrecht, 1990; pp 685–693.
- (72) Zubarev, R. A.; Kelleher, N. L.; McLafferty, F. W. Electron Capture Dissociation of Multiply Charged Protein Cations. A Nonergodic Process. *J. Am. Chem. Soc.* **1998**, *120*, 3265–3266.
- (73) Syka, J. E. P.; Coon, J. J.; Schroeder, M. J.; Shabanowitz, J.; Hunt, D. F. Peptide and Protein Sequence Analysis By Electron Transfer Dissociation Mass Spectrometry. *P. Natl. Acad. Sci. USA* **2004**, *101*, 9528–9533.
- (74) Sablier, M.; Fujii, T. Mass Spectrometry of Free Radicals. *Chem. Rev.* **2002**, *102*, 2855–2924.
- (75) Polfer, N. C. Infrared Multiple Photon Dissociation Spectroscopy of Trapped Ions. *Chem. Soc. Rev.* **2011**, *40*, 2211–2221.
- (76) Eyler, J. R. Infrared Multiple Photon Dissociation Spectroscopy of Ions in Penning Traps. *Mass Spectrom. Rev.* **2009**, *28*, 448–467.

- (77) Cheng, P. Y.; Zhong, D.; Zewail, A. H. Kinetic-Energy, Femtosecond Resolved Reaction Dynamics. Modes of Dissociation (in Iodobenzene) from Time-Velocity Correlations. *Chem. Phys. Lett.* **1995**, *237*, 399–405.
- (78) Zabuga, A. V.; Kamrath, M. Z.; Boyarkin, O. V.; Rizzo, T. R. Fragmentation Mechanism of UV-Excited Peptides in the Gas Phase. *J. Chem. Phys.* **2014**, *141*, 154309.
- (79) Stannard, P. R.; Gelbart, W. M. Intramolecular Vibrational Energy Redistribution. *J. Phys. Chem.* **1981**, *85*, 3592–3599.
- (80) Talbert, L. E.; Julian, R. R. Directed-Backbone Dissociation Following Bond-Specific Carbon-Sulfur UVPD at 213 nm. *J. Am. Soc. Mass Spectrom.* **2018**, *29*, 1760–1767.
- (81) Thoen, K. K.; Pérez, J.; Ferra, J. J.; Kenttämaa, H. I. Synthesis of Charged Phenyl Radicals And Biradicals By Laser Photolysis in a Fourier-Transform Ion Cyclotron Resonance Mass Spectrometer. *J. Am. Soc. Mass Spectrom.* **1998**, *9*, 1135–1140.
- (82) Kistiakowsky, G. B.; Solomon, A. K. The Ultraviolet Absorption Spectrum of Benzene. *J. Chem. Phys.* **1937**, *5*, 609–616.
- (83) Kavita, K.; Das, P. K. Photodissociation of C₆H₅I, C₆F₅I, and Related Iodides in the Ultraviolet. *J. Chem. Phys.* **2002**, *117*, 2038–2044.
- (84) Ly, T.; Julian, R. R. Residue-Specific Radical-Directed Dissociation of Whole Proteins in the Gas Phase. *J. Am. Chem. Soc.* **2008**, *130*, 351–358.
- (85) Cederbaum, A. I. Alcohol Metabolism. *Clin. Liver Dis.* **2012**, *16*, 667–685.
- (86) Neale D. Ridgway and Roger S. McLeod, Ed. *Biochemistry of Lipids, Lipoproteins and Membranes*; Elsevier: Amsterdam, 2016.
- (87) Liu, Z.; Barrett, E. J. Human Protein Metabolism: Its Measurement And Regulation. *Am. J. Physiol.-Endoc. M.* **2002**, *283*, 1105-1112.
- (88) Fahy, E.; Subramaniam, S.; Murphy, R. C.; Nishijima, M.; Raetz, C. R. H.; Shimizu, T.; Spener, F.; van Meer, G.; Wakelam, M. J. O.; Dennis, E. A. Update of the LIPID MAPS Comprehensive Classification System for Lipids. *J. Lipid Res.* **2009**, *50 Suppl*, 9-14.
- (89) Paine, M. R. L.; Poad, B. L. J.; Eijkel, G. B.; Marshall, D. L.; Blanksby, S. J.; Heeren, R. M. A.; Ellis, S. R. Mass Spectrometry Imaging With Isomeric Resolution

Enabled by Ozone-Induced Dissociation. *Angew. Chem., Int. Ed.* **2018**, *57*, 10530–10534.

(90) Wäldchen, F.; Becher, S.; Esch, P.; Kompauer, M.; Heiles, S. Selective Phosphatidylcholine Double Bond Fragmentation And Localisation Using Paternò-Büchi Reactions And Ultraviolet Photodissociation. *Analyst* **2017**, *142*, 4744–4755.

(91) Williams, P. E.; Klein, D. R.; Greer, S. M.; Brodbelt, J. S. Pinpointing Double Bond And *sn*-Positions in Glycerophospholipids via Hybrid 193 nm Ultraviolet Photodissociation (UVPD) Mass Spectrometry. *J. Am. Chem. Soc.* **2017**, *139*, 15681–15690.

(92) Kates, M. Techniques of Lipidology: Isolation, analysis and identification of lipids. *Laboratory Techniques in Biochemistry and Molecular Biology*; pp 267–274.

(93) Ekroos, K.; Ejsing, C. S.; Bahr, U.; Karas, M.; Simons, K.; Shevchenko, A. Charting Molecular Composition of Phosphatidylcholines by Fatty Acid Scanning and Ion Trap MS³ Fragmentation. *J. Lipid Res.* **2003**, *44*, 2181–2192.

(94) Zhao, X.; Zhang, W.; Zhang, D.; Liu, X.; Cao, W.; Chen, Q.; Ouyang, Z.; Xia, Y. A Lipidomic Workflow Capable of Resolving *sn*- And C=C Location Isomers of Phosphatidylcholines. *Chem. Sci.* **2019**, *10*, 10740–10748.

(95) Hsu, F.-F.; Turk, J. Characterization of Phosphatidylethanolamine as a Lithiated Adduct by Triple Quadrupole Tandem Mass Spectrometry With Electrospray Ionization. *J. Mass Spectrom.* **2000**, *35*, 595–606.

(96) Olsen, J. V.; Macek, B.; Lange, O.; Makarov, A.; Horning, S.; Mann, M. Higher-Energy C-Trap Dissociation for Peptide Modification Analysis. *Nat. Methods* **2007**, *4*, 709–712.

(97) Götze, M.; Iacobucci, C.; Ihling, C. H.; Sinz, A. A Simple Cross-Linking/Mass Spectrometry Workflow for Studying System-wide Protein Interactions. *Anal. Chem.* **2019**, *91*, 10236–10244.

(98) Sinz, A. Chemical Cross-Linking And Mass Spectrometry to Map Three-Dimensional Protein Structures And Protein-Protein Interactions. *Mass Spectrom. Rev.* **2006**, *25*, 663–682.

(99) Miranker, A.; Robinson, C. V.; Radford, S. E.; Aplin, R. T.; Dobson, C. M. Detection of Transient Protein Folding Populations by Mass Spectrometry. *Science* **1993**, *262*, 896–900.

- (100) Konermann, L.; Pan, J.; Liu, Y.-H. Hydrogen Exchange Mass Spectrometry for Studying Protein Structure And Dynamics. *Chem. Soc. Rev.* **2011**, *40*, 1224–1234.
- (101) Dempster, A. J. A new Method of Positive Ray Analysis. *Phys. Rev.* **1918**, *11*, 316–325.
- (102) Munson, M. S. B.; Field, F. H. Chemical Ionization Mass Spectrometry. I. General Introduction. *J. Am. Chem. Soc.* **1966**, *88*, 2621–2630.
- (103) Field, F. H. Chemical Ionization Mass Spectrometry. *Acc. Chem. Res.* **1968**, *1*, 42–49.
- (104) Honig, R. E.; Woolston, J. R. Laser-Induced Emission of Electrons, Ions, and Neutral Atoms from Solid Surfaces. *Appl. Phys. Lett.* **1963**, *2*, 138–139.
- (105) Mandal, A.; Singha, M.; Addy, P. S.; Basak, A. Laser Desorption Ionization Mass Spectrometry: Recent Progress in Matrix-Free And Label-Assisted Techniques. *Mass Spectrom. Rev.* **2019**, *38*, 3–21.
- (106) Barber, M.; Bordoli, R. S.; Sedgwick, R. D.; Tyler, A. N. Fast Atom Bombardment of Solids as an Ion Source in Mass Spectrometry. *Nature* **1981**, *293*, 270–275.
- (107) Fenn, J. B. Electrospray Wings for Molecular Elephants (Nobel lecture). *Angew. Chem., Int. Edit.* **2003**, *42*, 3871–3894.
- (108) Karas, M.; Bachmann, D.; Hillenkamp, F. Influence of the Wavelength in High-Irradiance Ultraviolet Laser Desorption Mass Spectrometry of Organic Molecules. *Anal. Chem.* **1985**, *57*, 2935–2939.
- (109) Karas, M.; Hillenkamp, F. Laser Desorption Ionization of Proteins With Molecular Masses Exceeding 10,000 Daltons. *Anal. Chem.* **1988**, *60*, 2299–2301.
- (110) Wong, S. F.; Meng, C. K.; Fenn, J. B. Multiple Charging in Electrospray Ionization of Poly(ethylene glycols). *J. Phys. Chem.* **1988**, *92*, 546–550.
- (111) Fenn, J. B.; Mann, M.; Meng, C. K.; Wong, S. F.; Whitehouse, C. M. Electrospray Ionization for Mass Spectrometry of Large Biomolecules. *Science* **1989**, *246*, 64–71.
- (112) Geoffrey Ingram Taylor. Disintegration of Water Drops in an Electric Field. *Proc. R. Soc. Lond. A* **1964**, *280*, 383–397.

- (113) Rayleigh. On the Equilibrium of Liquid Conducting Masses Charged With Electricity. *Lond., Edinb., Dub. Philos. Mag. J. Sci.* **1882**, *14*, 184–186.
- (114) Taflin, D. C.; Ward, T. L.; Davis, E. J. Electrified Droplet Fission And the Rayleigh Limit. *Langmuir* **1989**, *5*, 376–384.
- (115) Iribarne, J. V. On the evaporation of Small Ions From Charged Droplets. *J. Chem. Phys.* **1976**, *64*, 2287–2294.
- (116) Nguyen, S.; Fenn, J. B. Gas-Phase Ions of Solute Species From Charged Droplets of Solutions. *P. Natl. Acad. Sci. USA* **2007**, *104*, 1111–1117.
- (117) Dole, M.; Mack, L. L.; Hines, R. L.; Mobley, R. C.; Ferguson, L. D.; Alice, M. B. Molecular Beams of Macroions. *J. Chem. Phys.* **1968**, *49*, 2240–2249.
- (118) Wolff, M. M.; Stephens, W. E. A Pulsed Mass Spectrometer with Time Dispersion. *Rev. Sci. Instrum.* **1953**, *24*, 616–617.
- (119) Paul, W. Apparatus for Separating Charged Particles of Different Specific Charges, Dec 21, 1954.
- (120) Comisarow, M. B.; Marshall, A. G. Fourier Transform Ion Cyclotron Resonance Spectroscopy. *Chem. Phys. Lett.* **1974**, *25*, 282–283.
- (121) Makarov. Electrostatic Axially Harmonic Orbital Trapping: A High-Performance Technique of Mass Analysis. *Anal. Chem.* **2000**, *72*, 1156–1162.
- (122) Brenton, A. G.; Godfrey, A. R. Accurate Mass Measurement: Terminology and Treatment of Data. *J. Am. Soc. Mass Spectrom.* **2010**, *21*, 1821–1835.
- (123) Amster, J. I. Fourier Transform Mass Spectrometry. *J. Mass Spectrom.* **1996**, *31*, 1325–1337.
- (124) Nicholson, A. J. C. The Photochemical Decomposition of the Aliphatic Methyl Ketones. *T. Faraday Soc.* **1954**, *50*, 1067–1073.
- (125) Bythell, B. J.; Suhai, S.; Somogyi, A.; Paizs, B. Proton-Driven Amide Bond-Cleavage Pathways of Gas-Phase Peptide Ions Lacking Mobile Protons. *J. Am. Chem. Soc.* **2009**, *131*, 14057–14065.
- (126) Hohenberg, P.; Kohn, W. Inhomogeneous Electron Gas. *Phys. Rev.* **1964**, *136*, B 864-871.
- (127) Schöllkopf, W.; Gewinner, S.; Junkes, H.; Paarmann, A.; Helden, G. von; Bluem, H.; Todd, A. M. M. The New IR And THz FEL Facility at the Fritz Haber Institute in Berlin. *Proc. of SPIE* **2015**, *9512*, 1-13.

- (128) O'Shea, P. G.; Freund, H. P. Free-Electron Lasers. Status And Applications. *Science* **2001**, *292*, 1853–1858.
- (129) Colson, W. B.; Johnson, E. D.; Kelley, M. J.; Schwettman, H. A. Putting Free-Electron Lasers to Work. *Phys. Today* **2002**, *55*, 35–41.
- (130) Valle, J. J.; Eyler, J. R.; Oomens, J.; Moore, D. T.; van der Meer, A. F. G.; Helden, G. von; Meijer, G.; Hendrickson, C. L.; Marshall, A. G.; Blakney, G. T. Free Electron Laser-Fourier Transform Ion Cyclotron Resonance Mass Spectrometry Facility for Obtaining Infrared Multiphoton Dissociation Spectra of Gaseous Ions. *Rev. Sci. Instrum.* **2005**, *76*, 1–7.
- (131) Toennies, J. P.; Vilesov, A. F. Superfluid Helium Droplets: A Uniquely Cold Nanomatrix for Molecules And Molecular Complexes. *Angew. Chem., Int. Ed.* **2004**, *43*, 2622–2648.
- (132) Douglas Rayner Hartree and W. Hartree. Self-Consistent Field, with Exchange, for Beryllium. *Proc. R. Soc. Lond. A* **1935**, *150*, 9–33.
- (133) Fock, V. Näherungsmethode zur Lösung des quantenmechanischen Mehrkörperproblems. *Z. Physik* **1930**, *61*, 126–148.
- (134) Slater, J. C. The Theory of Complex Spectra. *Phys. Rev.* **1929**, *34*, 1293–1322.
- (135) Jensen, F. Estimating the Hartree—Fock Limit From Finite Basis Set Calculations. *Theor. Chem. Acc.* **2005**, *113*, 267–273.
- (136) Hillisch, A.; Heinrich, N.; Wild, H. Computational Chemistry in the Pharmaceutical Industry: From Childhood to Adolescence. *ChemMedChem* **2015**, *10*, 1958–1962.
- (137) Møller, C.; Plesset, M. S. Note on an Approximation Treatment for Many-Electron Systems. *Phys. Rev.* **1934**, *46*, 618–622.
- (138) Jensen, F. *Introduction to Computational Chemistry*, Third edition; Chichester, West Sussex, UK, 2017.
- (139) Mardirossian, N.; Head-Gordon, M. Thirty Years of Density Functional Theory in Computational Chemistry: An Overview And Extensive Assessment of 200 Density Functionals. *Mol. Phys.* **2017**, *115*, 2315–2372.
- (140) Schrödinger, E. An Undulatory Theory of the Mechanics of Atoms and Molecules. *Phys. Rev.* **1926**, *28*, 1049–1070.

- (141) van Mourik, T.; Gdanitz, R. J. A Critical Note on Density Functional Theory Studies on Rare-Gas Dimers. *J. Chem. Phys.* **2002**, *116*, 9620–9623.
- (142) Stephens, P. J.; Devlin, F. J.; Chabalowski, C. F.; Frisch, M. J. Ab Initio Calculation of Vibrational Absorption And Circular Dichroism Spectra Using Density Functional Force Fields. *J. Phys. Chem.* **1994**, *98*, 11623–11627.
- (143) Lee; Yang; Parr. Development of the Colle-Salvetti Correlation-Energy Formula Into a Functional of the Electron Density. *Phys. Rev. B* **1988**, *37*, 785–789.
- (144) Becke, A. D. Density-Functional Thermochemistry. III. The Role of Exact Exchange. *J. Chem. Phys.* **1993**, *98*, 5648–5652.
- (145) Kohn, W.; Sham, L. J. Self-Consistent Equations Including Exchange and Correlation Effects. *Phys. Rev.* **1965**, *140*, A 1133-1138.
- (146) Lehtola, S. A Review on Non-Relativistic, Fully Numerical Electronic Structure Calculations on Atoms And Diatomic Molecules. *Int. J. Quantum Chem.* **2019**, *119*, 1–31.
- (147) Slater, J. C. Atomic Shielding Constants. *Phys. Rev.* **1930**, *36*, 57–64.
- (148) Zener, C. Analytic Atomic Wave Functions. *Phys. Rev.* **1930**, *36*, 51–56.
- (149) Eckart, C. The Theory and Calculation of Screening Constants. *Phys. Rev.* **1930**, *36*, 878–892.
- (150) S. F. Boys. Electronic Wave Functions - I. A General Method of Calculation for the Stationary States of Any Molecular System. *Proc. R. Soc. Lond. A* **1950**, *200*, 542–554.
- (151) Averill, F. W.; Ellis, D. E. An Efficient Numerical Multicenter Basis Set for Molecular Orbital Calculations: Application to FeCl₄. *J. Chem. Phys.* **1973**, *59*, 6412–6418.
- (152) McMurchie, L. E.; Davidson, E. R. One- And Two-Electron Integrals Over Cartesian Gaussian Functions. *J. Comput. Phys.* **1978**, *26*, 218–231.
- (153) Kikuchi, R. Gaussian Functions in Molecular Integrals. *J. Chem. Phys.* **1954**, *22*, 148–149.
- (154) McLean, A. D.; Chandler, G. S. Contracted Gaussian Basis Sets for Molecular Calculations. I. Second Row Atoms, Z =11–18. *J. Chem. Phys.* **1980**, *72*, 5639–5648.

- (155) Krishnan, R.; Binkley, J. S.; Seeger, R.; Pople, J. A. Self-Consistent Molecular Orbital Methods. XX. A Basis Set For Correlated Wave Functions. *J. Chem. Phys.* **1980**, *72*, 650–654.
- (156) Dunning, T. H. Gaussian Basis Sets for Use in Correlated Molecular Calculations. I. The Atoms Boron Through Neon and Hydrogen. *J. Chem. Phys.* **1989**, *90*, 1007–1023.
- (157) Wilson, A. K.; Woon, D. E.; Peterson, K. A.; Dunning, T. H. Gaussian Basis Sets for Use in Correlated Molecular Calculations. IX. The Atoms Gallium Through Krypton. *J. Chem. Phys.* **1999**, *110*, 7667–7676.
- (158) Jensen, F. Polarization Consistent Basis Sets: Principles. *J. Chem. Phys.* **2001**, *115*, 9113–9125.
- (159) Becher, S.; Spengler, B.; Heiles, S. Effects of Wavelength, Fluence, and Dose on Fragmentation Pathways and Photoproduct Ion Yield in 213 nm and 266 nm Ultraviolet Photodissociation Experiments. *Eur. J. Mass Spectrom.* **2018**, *24*, 54–65.
- (160) Schnier, P. D.; Gross, D. S.; Williams, E. R. On the Maximum Charge State And Proton Transfer Reactivity of Peptide And Protein Ions Formed by Electrospray Ionization. *J. Am. Soc. Mass Spectrom.* **1995**, *6*, 1086–1097.
- (161) Becher, S.; Esch, P.; Heiles, S. Relative Quantification of Phosphatidylcholine *sn*-Isomers Using Positive Doubly Charged Lipid-Metal Ion Complexes. *Anal. Chem.* **2018**, *90*, 11486–11494.
- (162) Klein, D. R.; Brodbelt, J. S. Structural Characterization of Phosphatidylcholines Using 193 nm Ultraviolet Photodissociation Mass Spectrometry. *Anal. Chem.* **2017**, *89*, 1516–1522.
- (163) Hsu, F.-F.; Turk, J. Electrospray Ionization/Tandem Quadrupole mass Spectrometric Studies on Phosphatidylcholines: The Fragmentation Processes. *J. Am. Soc. Mass Spectrom.* **2003**, *14*, 352–363.
- (164) Yoo, H. J.; Håkansson, K. Determination of Phospholipid Regiochemistry By Ag(I) Adduction And Tandem Mass Spectrometry. *Anal. Chem.* **2011**, *83*, 1275–1283.

- (165) Becher, S.; Berden, G.; Martens, J.; Oomens, J.; Heiles, S. IRMPD Spectroscopy of PC (4:0/4:0) + M⁺ (M = H, Na, K) and Corresponding CID Fragment Ions. *J. Am. Soc. Mass Spectrom.* **2021**, *32*, 2874–2884.
- (166) Madsen, J. A.; Boutz, D. R.; Brodbelt, J. S. Ultrafast Ultraviolet Photodissociation at 193 nm And Its Applicability to Proteomic Workflows. *J. Proteome Res.* **2010**, *9*, 4205–4214.
- (167) Ly, T.; Julian, R. R. Ultraviolet Photodissociation: Developments Towards Applications for Mass-Spectrometry-Based Proteomics. *Angew. Chem., Int. Ed.* **2009**, *48*, 7130–7137.
- (168) Brodbelt, J. S.; Morrison, L. J.; Santos, I. Ultraviolet Photodissociation Mass Spectrometry for Analysis of Biological Molecules. *Chem. Rev.* **2020**, *120*, 3328–3380.
- (169) Wang, H.; Leeming, M. G.; Ho, J.; Donald, W. A. Origin And Prediction of Highly Specific Bond Cleavage Sites in the Thermal Activation of Intact Protein Ions. *Chem. - Eur. J.* **2019**, *25*, 823–834.
- (170) Coon, J. J.; Shabanowitz, J.; Hunt, D. F.; Syka, J. E. P. Electron Transfer Dissociation of Peptide Anions. *J. Am. Soc. Mass Spectrom.* **2005**, *16*, 880–882.
- (171) Becher, S.; Wang, H.; Leeming, M. G.; Donald, W. A.; Heiles, S. Influence of Protein Ion Charge State on 213 nm Top-Down UVPD. *Analyst* **2021**, *146*, 3977–3987.
- (172) Shaw, J. B.; Li, W.; Holden, D. D.; Zhang, Y.; Griep-Raming, J.; Fellers, R. T.; Early, B. P.; Thomas, P. M.; Kelleher, N. L.; Brodbelt, J. S. Complete Protein Characterization Using Top-Down Mass Spectrometry And Ultraviolet Photodissociation. *J. Am. Chem. Soc.* **2013**, *135*, 12646–12651.
- (173) Agranoff, B. W.; Bradley, R. M.; Brady, R. O. The Enzymatic Synthesis of Inositol Phosphatide. *J. Biol. Chem.* **1958**, *233*, 1077–1083.
- (174) Wang, H.; Loerke, D.; Bruns, C.; Müller, R.; Koch, P.-A.; Puchkov, D.; Schultz, C.; Haucke, V. Phosphatidylinositol 3,4-Bisphosphate Synthesis And Turnover Are Spatially Segregated in the Endocytic Pathway. *J. Biol. Chem.* **2020**, *295*, 1091–1104.

- (175) Marat, A. L.; Haucke, V. Phosphatidylinositol 3-Phosphates - At the Interface Between Cell Signalling And Membrane Traffic. *EMBO J.* **2016**, *35*, 561–579.
- (176) Hammond, G. R. V.; Fischer, M. J.; Anderson, K. E.; Holdich, J.; Koteci, A.; Balla, T.; Irvine, R. F. PI4P and PI(4,5)P₂ are Essential But Independent Lipid Determinants of Membrane Identity. *Science* **2012**, *337*, 727–730.
- (177) Hasegawa, J.; Strunk, B. S.; Weisman, L. S. PI5P and PI(3,5)P₂: Minor, but Essential Phosphoinositides. *Cell Struct. Funct.* **2017**, *42*, 49–60.
- (178) Vicinanza, M.; Korolchuk, V. I.; Ashkenazi, A.; Puri, C.; Menzies, F. M.; Clarke, J. H.; Rubinsztein, D. C. PI(5)P Regulates Autophagosome Biogenesis. *Mol. Cell* **2015**, *57*, 219–234.
- (179) Gozzelino, L.; Santis, M. C. de; Gulluni, F.; Hirsch, E.; Martini, M. PI(3,4)P₂ Signaling in Cancer and Metabolism. *Front. Oncol.* **2020**, *10*, 1–12.
- (180) Manna, P.; Jain, S. K. Phosphatidylinositol-3,4,5-Triphosphate and Cellular Signaling: Implications for Obesity And Diabetes. *Cell. Physiol. Biochem.* **2015**, *35*, 1253–1275.
- (181) Kim, S. H.; Song, H. E.; Kim, S. J.; Woo, D. C.; Chang, S.; Choi, W. G.; Kim, M. J.; Back, S. H.; Yoo, H. J. Quantitative Structural Characterization of Phosphatidylinositol Phosphates From Biological Samples. *J. Lipid Res.* **2017**, *58*, 469–478.
- (182) Ghiladi, M.; McKenzie, C. J.; Meier, A.; Powell, A. K.; Ulstrup, J.; Wocadlo, S. Dinuclear Iron(III)–Metal(II) Complexes as Structural Core Models for Purple Acid Phosphatases. *J. Chem. Soc. Dalton* **1997**, 4011–4018.
- (183) Svane, S.; Kryuchkov, F.; Lennartson, A.; McKenzie, C. J.; Kjeldsen, F. Overcoming the Instability of Gaseous Peptide Phosphate Ester Groups By Dimetal Protection. *Angew. Chem., Int. Ed.* **2012**, *51*, 3216–3219.
- (184) Svane, S.; Jørgensen, T. J. D.; McKenzie, C. J.; Kjeldsen, F. Effect of Metals in Biomimetic Dimetal Complexes on Affinity And Gas-Phase Protection of Phosphate Esters. *Anal. Chem.* **2015**, *87*, 7060–7068.
- (185) Klein, D. R.; Blevins, M. S.; Macias, L. A.; Douglass, M. V.; Trent, M. S.; Brodbelt, J. S. Localization of Double Bonds in Bacterial Glycerophospholipids

Using 193 nm Ultraviolet Photodissociation in the Negative Mode. *Anal. Chem.* **2020**, *92*, 5986–5993.

(186) Ma, X.; Xia, Y. Pinpointing Double Bonds in Lipids by Paternò-Büchi Reactions And Mass Spectrometry. *Angew. Chem., Int. Edit.* **2014**, *53*, 2592–2596.

(187) Esch, P.; Heiles, S. Investigating C=C Positions and Hydroxylation Sites in Lipids Using Paternò-Büchi Functionalization Mass Spectrometry. *Analyst* **2020**, *145*, 2256–2266.

(188) Sun, Q.; Nelson, H.; Ly, T.; Stoltz, B. M.; Julian, R. R. Side Chain Chemistry Mediates Backbone Fragmentation in Hydrogen Deficient Peptide Radicals. *J. Proteome Res.* **2009**, *8*, 958–966.

(189) Felix-Levin Hormann. Mass Spectrometric Methods for the Structure Elucidation of Iodobenzaldehyde Functionalized Sphingolipids by means of Radical Directed Dissociation. Bachelor Thesis, Justus-Liebig-University Gießen, 2020.

(190) Ly, T.; Julian, R. R. Tracking Radical Migration in Large Hydrogen Deficient Peptides With Covalent Labels: Facile Movement Does Not Equal Indiscriminate Fragmentation. *J. Am. Soc. Mass Spectrom.* **2009**, *20*, 1148–1158.

(191) Matyash, V.; Liebisch, G.; Kurzchalia, T. V.; Shevchenko, A.; Schwudke, D. Lipid Extraction by Methyl-Tert-Butyl Ether for High-Throughput Lipidomics. *J. Lipid Res.* **2008**, *49*, 1137–1146.

(192) Poad, B. L. J.; Zheng, X.; Mitchell, T. W.; Smith, R. D.; Baker, E. S.; Blanksby, S. J. Online Ozonolysis Combined With Ion Mobility-Mass Spectrometry Provides a New Platform for Lipid Isomer Analyses. *Anal. Chem.* **2018**, *90*, 1292–1300.

(193) Cannon, J. R.; Cammarata, M. B.; Robotham, S. A.; Cotham, V. C.; Shaw, J. B.; Fellers, R. T.; Early, B. P.; Thomas, P. M.; Kelleher, N. L.; Brodbelt, J. S. Ultraviolet Photodissociation for Characterization of Whole Proteins on a Chromatographic Time Scale. *Anal. Chem.* **2014**, *86*, 2185–2192.

(194) Martens, J.; Grzetic, J.; Berden, G.; Oomens, J. Structural Identification of Electron Transfer Dissociation Products in Mass Spectrometry Using Infrared Ion Spectroscopy. *Nat. Commun.* **2016**, *7*, 11754.

(195) Lau, J. K.-C.; Esuon, F.; Berden, G.; Oomens, J.; Hopkinson, A. C.; Ryzhov, V.; Siu, K. W. M. Generation, Characterization, And Dissociation of Radical

Cations Derived from Prolyl-glycyl-glycine. *J. Phys. Chem. B* **2021**, *125*, 6121–6129.

(196) Kirschbaum, C.; Greis, K.; Polewski, L.; Gewinner, S.; Schöllkopf, W.; Meijer, G.; Helden, G. von; Pagel, K. Unveiling Glycerolipid Fragmentation by Cryogenic Infrared Spectroscopy. *J. Am. Chem. Soc.* **2021**, *143*, 14827–14834.

(197) Kirschbaum, C.; Greis, K.; Mucha, E.; Kain, L.; Deng, S.; Zappe, A.; Gewinner, S.; Schöllkopf, W.; Helden, G. von; Meijer, G.; *et al.* Unravelling the Structural Complexity of Glycolipids With Cryogenic Infrared Spectroscopy. *Nat. Commun.* **2021**, *12*, 1201.

(198) Lettow, M.; Greis, K.; Grabarics, M.; Horlebein, J.; Miller, R. L.; Meijer, G.; Helden, G. von; Pagel, K. Chondroitin Sulfate Disaccharides in the Gas Phase: Differentiation and Conformational Constraints. *J. Phys. Chem. A* **2021**, *125*, 4373–4379.

(199) van Outersterp, R. E.; Martens, J.; Peremans, A.; Lamard, L.; Cuyckens, F.; Oomens, J.; Berden, G. Evaluation of Table-Top Lasers for Routine Infrared Ion Spectroscopy in the Analytical Laboratory. *Analyst* **2021**, *146*, 7218–7229.

(200) Zenaidee, M.; Lantz, C.; Perkins, T.; Fu, J.; Jung, W.; R. Ogorzalek Loo, R.; Loo, J. A. *Internal Fragments Generated by Electron Ionization Dissociation Enhances Protein Top-down Mass Spectrometry*, 2020.

(201) Brown, S. Formation and dissociation of highly charged protein ions, UNSW Sydney, 2021.

(202) Santos, I. C.; Brodbelt, J. S. Structural Characterization of Carbonic Anhydrase-Arylsulfonamide Complexes Using Ultraviolet Photodissociation Mass Spectrometry. *J. Am. Soc. Mass Spectrom.* **2021**, *32*, 1370–1379.

(203) Crittenden, C. M.; Novelli, E. T.; Mehaffey, M. R.; Xu, G. N.; Giles, D. H.; Fies, W. A.; Dalby, K. N.; Webb, L. J.; Brodbelt, J. S. Structural Evaluation of Protein/Metal Complexes via Native Electrospray Ultraviolet Photodissociation Mass Spectrometry. *J. Am. Soc. Mass Spectrom.* **2020**, *31*, 1140–1150.

II. Publications

Publication 3

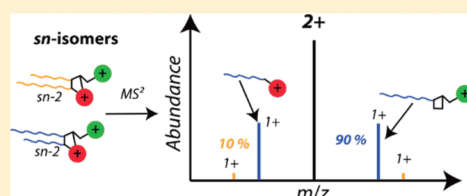
Relative Quantification of Phosphatidylcholine *sn*-Isomers Using Positive Doubly Charged Lipid–Metal Ion Complexes

Simon Becher,[‡] Patrick Esch,[‡] and Sven Heiles^{*†}

Institute of Inorganic and Analytical Chemistry, Justus Liebig University Giessen, 35392 Giessen, Germany

Supporting Information

ABSTRACT: Phosphatidylcholines are the major phospholipid component of most eukaryotic cell membranes. Phosphatidylcholines have been shown to actively participate in regulatory and metabolic processes. Dysfunctional metabolic processes have been linked to human disease and can result in altered phosphatidylcholine structural features, such as permutation of fatty acid connectivity. Assignment and relative quantitation of structural isomers that arise from fatty acid permutation on the phosphatidylcholine backbone, so-called *sn*-isomers, is difficult with routine tandem mass spectrometry or with liquid chromatography without authentic standards. In this work, we report on the observation that phosphatidylcholines form abundant doubly charged metal ion complexes during electrospray ionization (ESI) and show that these complexes can be used to assign fatty acid moieties, relatively quantify *sn*-isomers in MS^2 experiments, and mass spectrometrically separate phosphatidylcholines from other phospholipid classes in positive ion mode. Addition of Fe^{2+} salts (20 mol %) to ESI spray solutions affords highly abundant doubly charged metal ion phosphatidylcholine complexes (~110% of protonated compounds) and allows sensitive fragment ion detection (limit of detection = 100 pM). Higher energy collisional dissociation, collision-induced dissociation, and ultraviolet photodissociation of doubly charged complexes yield two fragment ions for every fatty acid moiety. The latter two tandem MS methods preferentially yield *sn*-2 associated product ions enabling relative *sn*-isomer quantification. The analytical utility of doubly charged phosphatidylcholine-metal ion complexes is demonstrated for polar lipid extracts, including extracts from diabetes type 1 and type 2 mouse models, and *sn*-isomer abundances are derived.



Glycerophospholipids play essential roles in cellular function, influencing structural integrity and biophysical properties of cellular membranes, modulating membrane protein functions, and serving as intra- as well as intercellular signaling molecules.^{1–6} This multitude of biochemical functions gives rise to the structural diversity encountered for this lipid class. Changes in lipid abundance, lipid structures, or dysregulation of glycerophospholipid metabolism have been implicated in cancer, diabetes, and cardiovascular disease.^{7–10} But also cell types, tissue regions, or cell mating has been linked to specific glycerophospholipids or lipid distributions.^{11–13}

In particular, phosphatidylcholines (PCs) that are the major components of most eukaryotic cell membranes, have been associated with multiple biochemical processes.^{4,5} For example, the cell mating of *Tetrahymena thermophila* was studied by Ewing and co-workers revealing that PC levels are diminished at cell–cell interfaces during cell fusion.^{12,13} Mouchlis et al. recently demonstrated that the selectivity of three different human phospholipase A₂ (PLA₂) enzymes, that exclusively cleave *sn*-2 (*sn*: stereospecific numbering) ester groups, is influenced by the fatty acid (FA) attached to *sn*-2 and differs between members of different PLA₂ enzyme families.¹⁴ These results indicate that PC structure-dependent lipid-enzyme interactions exist and that PC remodeling depends on the

PLA₂ enzyme type. In line with the structure-sensitive selectivity of PLA₂ enzymes toward PCs, localized changes of PC isomers were recently visualized by Ellis and co-workers.¹⁵ They were able to show that the relative abundance of PC *sn*- and double bond position isomers depends on tissue regions and hypothesized that these changes reflect cell-specific enzyme activities and therefore cell-specific lipid metabolism. A similar PC isomer specific effect that even compartmentalizes PC distribution within cells, was found for neurons.¹⁶ One specific PC *sn*-isomer is accumulated in the presynaptic plasma membrane suggesting a specific function of this lipid. This combined evidence highlights that obtaining molecular-level understanding for PC structures is of great importance.

Many advancements in lipid analysis in recent years were driven by mass spectrometry (MS) and tandem MS (MS/MS) methods.^{17–22} Lipidomics studies have benefited from powerful MS methods, such as direct infusion “shotgun” lipidomics and liquid chromatography (LC) approaches.^{23–25} When coupled to high performance mass spectrometers these methods allow for routine lipid sum formulas assignment

Received: June 17, 2018

Accepted: September 10, 2018

Published: September 10, 2018

and simultaneous quantification of hundreds of lipid. MS/MS in the form of collision-induced dissociation (CID) is a powerful tool to aid lipid assignments from accurate mass measurements with lipid headgroup and FA moiety information.^{17,26} For example, positive ion mode MS/MS measurements of protonated PCs are dominated by the headgroup fragment ion at m/z 184 that allow to discriminate PCs from isobaric phosphatidylethanolamines (PEs).^{27,28} For FA assignment of PCs, MS/MS of $[\text{PC}+\text{X}]^-$, with $\text{X} = \text{Cl}, \text{HCOO},$ or CH_3COO , in negative ion mode is required. In contrast to headgroup and FA composition, positional double bond isomers, stereochemistry of double bonds, and *sn*-isomers are not accessible from routine CID experiments. Powerful LC-MS, LC-MS/MS, and most recently ion mobility spectrometry (IMS)-MS methods separated isomeric PCs.^{29–32} For example, Nakanishi et al. developed a LC-MS/MS method that separated PC *sn*-isomers.²⁹ Despite the impressive capabilities of LC and IMS methods, all these separation techniques require authentic standards for accurate PC structure assignment.

To address the problem of lipid structure identification new tandem MS methods aim to generate PC structure selective fragment ions that allow to probe *sn*-positions or double bond isomers. Paternò-Büchi functionalization,^{33–36} ozone-induced dissociation (OzID),^{37,38} metastable atom activated dissociation,³⁹ radical directed dissociation,^{40,41} and ultraviolet photodissociation (UVPD)^{36,42,43} are the most widely adapted tandem MS methods that probe double bond positional isomers. Electron impact excitation of ions from organics was reported to yield information about PC double bond geometries.⁴⁴ Whereas the number of double bond selective tandem MS methods has considerably increased in recent years, discrimination or relative quantification of *sn*-isomers of PCs using tandem MS methods is rather scarce. Most notably Blanksby and co-workers used CID of $[\text{PC}+\text{Na}]^+$ followed by OzID of product ions in order to assign *sn*-isomers.^{45,46} Discrimination between *sn*-1 and *sn*-2 position most likely occurs during CID activation because OzID predominantly cleaves FAs in *sn*-2 position, whereas OzID without CID does not result in *sn*-selective fragments. Relative *sn*-isomeric abundances from CID/OzID experiments are extracted by taking the relative fragment ion abundances into account. In line with the CID/OzID method, Ekroos et al. were able to correlate relative product ion abundances with *sn*-isomeric purities by using *sn*-2 selective ion trap CID-MS³ of $[\text{PC}+\text{Cl}]^-$ ions in negative ion mode.⁴⁷ Brodbelt and co-workers most recently employed higher-energy collisional dissociation (HCD) followed by UVPD to assign *sn*-isomers as well as double bond positions in a MS³ workflow.⁴⁸ Adduct formation between metal ions and glycerophospholipids, such as Ag^+ and neutral PCs,⁴⁹ was shown to yield fragment ion abundances in MS² experiments but the analytical capabilities of this method were not explored in more detail.^{49–51}

In this work, the formation as well as fragmentation of $[\text{PC}+\text{M}]^{2+}$ ($\text{M} = \text{Mg}, \text{Sr}, \text{Ba}, \text{Mn}, \text{Fe}, \text{Co}, \text{Cu}, \text{Zn}$ or Sn) during electrospray ionization (ESI) is investigated to evaluate if doubly charged PC–metal ion complexes can be used to assign and relatively quantify PC *sn*-isomers from complex lipid mixtures. Fragment ions and relative product ion abundances are compared between tandem MS methods (UVPD, CID, HCD) and enzymatic PLA₂ digestion to study the *sn*-selectivity of different activation methods. The ability to use CID and UVPD of $[\text{PC}+\text{X}]^{2+}$ ions to relatively quantify *sn*-isomers in

complex mixtures is demonstrated by performing shotgun lipid analysis of different polar lipid extracts and determining PC *sn*-isomer abundances.

EXPERIMENTAL SECTION

Safety Considerations. MeOH/EtOH were used as ESI spray solvents. ESI requires high voltage to produce ions. To ensure safe handling, ESI sources are shielded and excess solvent was transferred to solvent containers using flexible tubing. UV laser light is dangerous for skin and eyes. All equipment and laboratories were approved by the laser safety officer and laser safety goggles were worn at all time.

Lipid Nomenclature. Shorthand notations according to the guidelines by Liebisch et al. are used throughout the manuscript.⁵² The separator “/” is used to indicate that the *sn* positions of the FA moieties are known. For synthetic standards the double bond position with respect to the ester group and double bond geometry are reported in the format “9Z”. When the double bond position and geometry is unknown this nomenclature is omitted. Abbreviations are introduced for some lipid standards for clarity.

Materials. All synthetic standards, solvents, salts, or reagents were obtained from commercial sources and used without further purification. PC 16:0/18:1(9Z), PC 18:1(9Z)/16:0, PC 18:0/18:1(9Z), PC 18:1(9Z)/18:0, PC 16:0/18:0, PC 18:0/16:0, PC 16:0/16:0, PC 14:0/18:0, PC 18:0/14:0, SM d18:1/16:0, egg yolk, porcine brain, and yeast extracts were purchased from Avanti Polar Lipids Inc. (Alabaster, AL, U.S.A.). PC 18:1(9Z)/18:1(9Z) was purchased from NOF Corporation (New York, U.S.A.). Metal salt screening experiments were performed with NaCl, KCl, MgCl₂, SrCl₂, BaSO₄, MnCl₂, FeSO₄, FeCl₂, CoSO₄, CuSO₄, ZnSO₄, and SnCl₂ with purities of 90% or higher obtained from Sigma-Aldrich (Munich, Germany). All other experiments were performed with anhydrous FeCl₂ (99.998%, Sigma-Aldrich). Phospholipase A₂ (PLA₂) from honey bee and all other chemicals for PLA₂ digestion were purchased from Sigma-Aldrich.

PLA₂ Digestion. We followed the PLA₂ digestion protocol used by Ekroos and co-workers with some modifications.⁴⁷ In brief, 500 nmol of PC lipid standard was dissolved in 800 μL methanol. This solution was mixed with a solution containing 450 μL water, 20 mM Tris-HCl, 40 mM CaCl₂, and 7 μg PLA₂. Resulting samples were vortexed for 15 h prior to solvent evaporation. Dried reaction mixtures were reconstituted in methanol with 1% formic acid for mass spectrometric analysis.

Standard Solutions for MS Analysis. Lipid standards with 10–100 μM concentration were dissolved in ethanol–water (99:1; v/v), methanol–water (99:1; v/v), or mixtures thereof, and FeCl₂ dissolved in water or methanol (1 mM) was added to a final concentration of 20 mol % with respect to the lipid. Some experiments were performed with 100 pM to 1 μM lipid concentrations (see Supporting Information, SI). The limit of detection (LOD) was estimated by diluting a 10 μM POPC solution containing 20 mol % FeCl₂ by a factor of 10 until no more fragment ions stemming from CID of $[\text{POPC}+\text{Fe}]^{2+}$ were detected. The reported LOD is the concentration of the last solution in the dilution series for which the signal-to-noise of the fragment ions was above 3.

Lipid Extraction and Preparation for Analysis. Lipid extracts of mouse pancreas tissue from female C57-J, ins2Akita, and db/db mice were prepared according to Matyash et al., and details are described in the SI.⁵³ Extracts in CHCl₃ were

dried and stored at $-80\text{ }^{\circ}\text{C}$. Purchased and dried extracts were reconstituted in CHCl_3 -methanol (50:50; v/v) with final concentrations of $0.04\text{--}0.40\text{ g}\cdot\text{L}^{-1}$ and 20 v% of 1 mM FeCl_2 solution in methanol was added for shotgun experiments. After quantifying PC 34:1 in porcine brain extract, the LOD of PC 34:1 in porcine brain extract was determined as described above for standards.

Mass Spectrometric Analysis of Lipid Standards and Extracts. All mass spectrometric experiments were performed on a 7 T LTQ FT Ultra or a Q Exactive instrument (both Thermo Scientific, Bremen, Germany) equipped with Thermo Scientific heated electrospray ionization (HESI) sources. HCD was performed on the Q Exactive instrument, whereas the LTQ FT Ultra was used for ion trap CID and UVPD at 213 nm as described previously.⁵⁴ Normalized collision energy (NCE) were tested for CID and HCD (Figure S-1) and best results (highest *sn*-2 selectivity) were obtained for NCE 12 for LTQ-FT Ultra and NCE 10 for Q Exactive experiments. UVPD with 213 nm laser light was performed with 40 laser pulses but the fragment ion identity does not depend on the number of laser pulses. Similar results but lower UVPD fragment ion yields compared to 40 pulses were obtained with 2–20 laser pulses (see ref 54). UVPD fragment ion yields were obtained by dividing the sum of all (or a selected subset) fragment ions by the sum of all ion abundances in UVPD mass spectra. Experimental settings: +4.5 kV HESI voltage; $330\text{ }^{\circ}\text{C}$ inlet temperature; 80 S-lens (Q Exactive), 35 V capillary and 120 V tube lens voltage (LTQ FT Ultra); 100 000 at m/z 400 (LTQ FT Ultra)/140 000 at m/z 200 (Q Exactive) mass resolution; ± 3 ppm mass accuracy (FTMS methods); $\Delta m/z = 0.4$ (Q Exactive), $\Delta m/z = 1.5$ (LTQ FT Ultra) isolation window. All reported uncertainties are standard deviations from triplicate measurements.

RESULTS AND DISCUSSION

Formation of Doubly Charged Lipid Metal Ion Complexes and UVPD. In an attempt to increase the UVPD fragment ion yield for phospholipids, lipid–metal complexes between PC 18:1(9Z)/18:1(9Z) and Na^+ , K^+ , Mg^{2+} , Sr^{2+} , Ba^{2+} , Mn^{2+} , Fe^{2+} , Co^{2+} , Cu^{2+} , Zn^{2+} , or Sn^{2+} were studied using ESI-MS and UVPD (213 nm) as summarized in Figure S-2.⁵⁴ The two singly charged reference complexes between PC 18:1(9Z)/18:1(9Z) and Na^+/K^+ , for which the CID/UVPD fragment ions and yields are well-known,^{26,43} form in 93% and 72% abundance with respect to the protonated lipid ion. UVPD of these ions results in low abundant headgroup related fragments (Figure S-2). In contrast, all investigated divalent metal ions, M^{2+} , form [PC 18:1(9Z)/18:1(9Z)+ M]²⁺ ion adducts (example Figure S-3) and the abundance of these ions depends on the M^{2+} identity (Figure S-2). The lowest abundance is observed for the Zn^{2+} adduct that is formed in >1% abundance with respect to the protonated phospholipid ion, whereas the abundance of Fe^{2+} adducts relative to [PC 18:1(9Z)/18:1(9Z)+H]⁺ is 12%. For glycerophospholipid classes other than PCs, formation of doubly charged metal ion complexes was not observed (results not shown) but doubly charged ions of sphingomyelins with divalent metals are formed (Figure S-4). The UVPD fragment ion yield is also affected by the metal ion identity (Figure S-2). For example, the attachment of Co^{2+} to PC 18:1(9Z)/18:1(9Z) results in a 36% UVPD fragment ion yield, a 13-fold UVPD fragment ion yield increase compared to results for [PC 18:1(9Z)/18:1(9Z)+ K]⁺. However, 97% of the UVPD frag-

ment ions obtained for [PC 18:1(9Z)/18:1(9Z)+ Co]²⁺ are associated with headgroup loss. In contrast, UVPD of [PC 18:1(9Z)/18:1(9Z)+ Fe]²⁺ does not result in headgroup loss and the overall UVPD fragment ion yield is 40%. Because increased UVPD fragment ion yields are obtained compared to results for $\text{H}^+/\text{Na}^+/\text{K}^+$, headgroup loss is suppressed and the propensity for [PC 18:1(9Z)/18:1(9Z)+ M]²⁺ formation is higher than for all other investigated divalent metal ions, Fe^{2+} is exclusively used in all following experiments.

Spray Solution Optimization. To improve the Fe^{2+} adduct ion abundance in ESI mass spectra, solvent composition and lipid to FeCl_2 ratio was optimized. Significantly improved [PC+ Fe]²⁺ ion abundances compared to results reported in Figure S-2 were obtained for solutions containing 1:1 v/v ethanol/water or 99:1 v/v methanol/water and 20 mol % FeCl_2 with respect to the lipid concentration. Representative mass spectra obtained for PC 18:1(9Z)/18:0 (OSPC) and PC 16:0/18:1(9Z) (POPC) are shown in Figure 1a (Figure S-5 for LTQ results) and Figure S-6, respectively. For example, the two most abundant signals in Figure 1a are [OSPC+H]⁺ (orange, m/z 788.616) and [OSPC+ Fe]²⁺ (red, m/z 421.771). The experimental isotopic distribution of the signals around m/z 421.771 is compared to the theoretical distribution for [OSPC+ Fe]²⁺ in Figure 1a (inset) confirming the assignment. The signal abundance of [OSPC+ Fe]²⁺ is 108% of the abundance of [OSPC+H]⁺ indicating that doubly charged lipid ion complexes are readily formed in ESI when appropriate solvents and experimental settings are used.

Effect of *sn*-Position on UVPD Results. In order to identify UVPD fragment ions and monitor the effect of a variable *sn*-fatty acid composition on [PC+ Fe]²⁺ fragment ion intensities, PC 18:0/18:1(9Z) (SOPC) and OSPC were investigated and results are shown in Figure 1b+c. The *sn*-1 position of SOPC contains a FA 18:0 moiety and FA 18:1(9Z) is attached to *sn*-2, whereas the *sn*-position of the same FAs are inverted in OSPC compared to SOPC. UVPD of both iron(II) adducts results in the same fragment ion signals. Two signals are present at m/z 504.345 and m/z 506.360 after UVPD (Figure 1b+c, blue). These signals are assigned to [OSPC–FA 18:0–H]⁺ (m/z 504.345) and [OSPC–FA 18:1–H]⁺ (m/z 506.360), respectively. The presence of fragment ions at m/z values above the doubly charged precursor in UVPD mass spectra suggests that [OSPC+ Fe]²⁺ and [SOPC+ Fe]²⁺ have lost [FA 18:0+ Fe –H]⁺ and [FA 18:1+ Fe –H]⁺ upon fragmentation. Corresponding fragment ions are present at m/z 337.183 and m/z 339.198 in both UVPD mass spectra (Figure 1b+c, green). Interestingly, the relative fragment ion abundance in [OSPC+ Fe]²⁺ (Figure 1b) and [SOPC+ Fe]²⁺ (Figure 1c) UVPD mass spectra differs. For [OSPC+ Fe]²⁺ the fragment ion at m/z 504.345 and the m/z 339.198, both associated with the cleavage of FA 18:0 from the precursor, are 16 times more abundant than FA 18:1(9Z) fragment ions. Permutation of the FA positions on the glycerol backbone in SOPC compared to OSPC results in pronounced FA 18:1(9Z) dissociation from the precursor with m/z 506.360 and m/z 337.183 being 5 times more abundant than m/z 504.345 and m/z 339.198. Because FA 18:0 is preferably lost from [OSPC+ Fe]²⁺ and FA 18:1(9Z) from [SOPC+ Fe]²⁺, the *sn*-2 attached FA moieties, these results indicate that UVPD of [PC+ Fe]²⁺ ions is a *sn*-2 selective fragmentation process.

Fragment Ions and Fragmentation Pathways of [PC+ Fe]²⁺. Possible fragment ion structures and fragmentation pathways that are consistent with UVPD results presented in

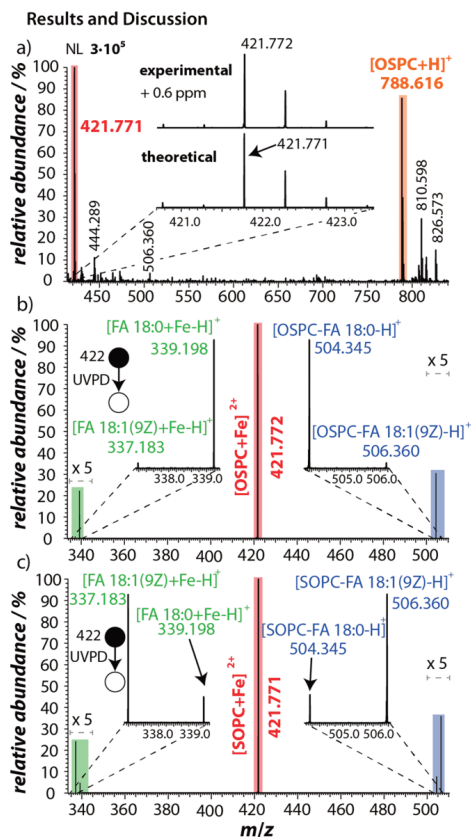
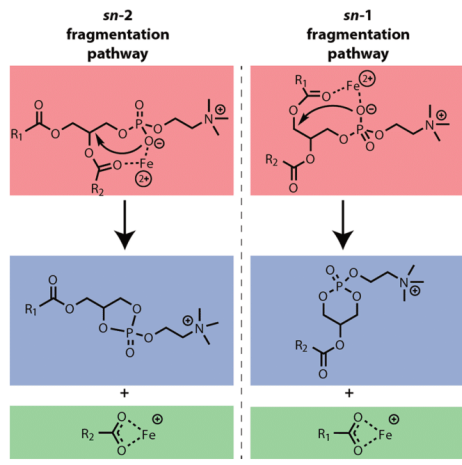


Figure 1. a) Positive ion mode ESI MS of PC 18:1 (9Z)/18:0 (OSPC) after FeCl_2 addition. Inset: Comparison of theoretical and experimental isotopic distributions for $[\text{OSPC}+\text{Fe}]^{2+}$. b) UVPD of $[\text{OSPC}+\text{Fe}]^{2+}$ (m/z 421.772, red). Assigned sum formulas and experimental m/z values are highlighted in green and blue, respectively. c) UVPD of $[\text{SOPC}+\text{Fe}]^{2+}$ (m/z 421.771, red). Assigned sum formulas and experimental m/z values are highlighted in green and blue, respectively.

Figure 1 are shown in Scheme 1. Activation of a $[\text{PC}+\text{Fe}]^{2+}$ *sn*-isomer with 213 nm UV light can facilitate formation of a five-membered ring containing the phosphate group to give fragment ions that are associated with FAs attached to *sn*-2 (R_2 -COOH). Alternatively, a six-membered ring is formed when *sn*-1 specific fragmentation (loss of R_1 -COOH) occurs. $[\text{PC}+\text{Fe}]^{2+}$ fragmentation results in two distinct singly charged ions for every *sn*-specific fragmentation pathway (Scheme 1) but no headgroup loss occurs as usually observed in tandem mass spectra of singly charged PCs.²⁶ Unlike CID of $[\text{PC}+\text{M}]^+$ with $\text{M} = \text{Li}, \text{Na}, \text{K}$ that results in neutral headgroup loss and intramolecular cyclization involving FA moieties as reported previously by several groups,^{46,48,55} the proposed fragmentation pathway of $[\text{PC}+\text{Fe}]^{2+}$ is consistent with results for $[\text{PC}+\text{H}]^+$ and CID-MS³ of $[\text{PC}+\text{formate}]^-$ for which similar

Scheme 1. Proposed Fragmentation Pathways for $[\text{PC}+\text{Fe}]^{2+}$ and Corresponding Proposed Fragment Ion Structures



fragment ions or neutral losses were observed.^{47,55} Because CID of singly charged PC ions is known to result in PC dissociation, $[\text{PC}+\text{Fe}]^{2+}$ were subjected to CID. CID of $[\text{PC}+\text{Fe}]^{2+}$ (Figure S-7) afforded product ion signals down to a LOD of 100 pM for standards and 500 pM for extracts (Figure S-8) that are consistent with the pathways proposed in Scheme 1. This provides evidence that fragmentation of $[\text{PC}+\text{Fe}]^{2+}$ using UV light or collisional activation results in the same fragment ion signals and most likely the same fragment ion species. CID-MS³ results for $[\text{PC}+\text{Fe}]^{2+}$ (Figures S-9–S-11) are in line with the proposed fragmentation pathways and ion structures shown in Scheme 1. These results indicate that activation of $[\text{PC}+\text{Fe}]^{2+}$ ions enable exclusive fragmentation of FA moieties from PCs using collisional and UV activation.

UVPD, CID, HCD of *sn*-isomers. In order to investigate the extent of *sn*-2 selectivity upon $[\text{PC}+\text{Fe}]^{2+}$ fragmentation, UVPD, CID, and HCD of iron(II) PC 16:0/18:1(9Z), PC 18:1(9Z)/16:0, PC 18:0/18:1(9Z), PC 18:1(9Z)/18:0, PC 16:0/18:0, PC 18:0/16:0, PC 14:0/18:0, and PC 18:0/14:0 adducts were performed. Results are summarized in Table 1 and shown in Figure 2 and S-12 for POPC and PC 18:1/16:0(9Z) (OPPC), respectively. Because commercially available *sn*-isomer lipid standards contain *sn*-isomeric impurities, PLA₂ digestion was performed, and these results are used as reference values (Table 1). The results for UVPD of $[\text{POPC}+\text{Fe}]^{2+}$ (Figure S-12a) and $[\text{OPPC}+\text{Fe}]^{2+}$ (Figure 2a) are similar when compared to the results for SOPC/OSPC (Figure 1). For $[\text{POPC}+\text{Fe}]^{2+}$, that contains a FA 18:1(9Z) moiety at *sn*-2 position, the relative abundance of fragment ions that originate from FA 18:1(9Z) loss (m/z 337.185 and m/z 478.329) is increased by a factor of 6 (Figure S-12a) compared to ions from FA 16:0 loss (m/z 311.167 and m/z 504.345). The FA 16:0 fragment ions are, on the other hand, 49 times more abundant than the FA 18:1(9Z) associated fragment ions for $[\text{OPPC}+\text{Fe}]^{2+}$ (Figure 2a). This indicates that dissociation of FAs attached to *sn*-2 position is preferred in UVPD of $[\text{PC}+\text{Fe}]^{2+}$ ions, in line with results for SOPC/OSPC. CID of

Table 1. Comparison of *sn*-Isomeric Purity for Synthetic Lipid Standards in Mol % Using PLA₂ Digestion and UVPD/CID/HCD

lipids ^a	PLA ₂ ^b	UVPD ^c	CID ^c	HCD ^c
PC 14:0/18:0	95/5	79/21	77/23	61/39
PC 18:0/14:0	89/11	83/17	58/42	62/38
PC 16:0/18:0	95/5	83/17	79/21	81/19
PC 18:0/16:0	91/9	77/23	75/25	74/26
PC 16:0/18:1(9Z)	93/7	85/15	82/18	81/19
PC 18:1(9Z)/16:0	97/3	98/2	83/17	56/44
PC 18:0/18:1(9Z)	92/8	82/18	71/19	88/12
PC 18:1(9Z)/18:0	88/12	94/6	65/35	54/46
MD ± SD ^d (n = 8)	---	9 ± 4	19 ± 4	23 ± 12

^aMajor *sn*-composition of lipid standard. ^bRelative abundance obtained with FT-ICR MS of chloride adducts. First number: major *sn*-isomer; second number: minor *sn*-isomer. Coefficient of variation 2%. ^cRelative abundance of [PC+Fe]²⁺ fragment ions. Coefficient of variation 3%. ^dMean absolute deviation (MD) and standard deviation (SD) with respect to PLA₂ results.

[POPC+Fe]²⁺ (Figure S-12b) and [OPPC+Fe]²⁺ (Figure 2b) also yield relative fragment ion abundances that are connected to the position of the FAs on the glycerol backbone. FA 18:1(9Z) loss is preferred over FA 16:0 loss in CID mass spectra of [POPC+Fe]²⁺, whereas relative fragment ion abundances are inverted in CID mass spectra of [OPPC+Fe]²⁺ compared to [POPC+Fe]²⁺. The increased abundance of fragment ions stemming from *sn*-2 position is, however, not observed for both *sn*-isomers in HCD experiments (Figures S-12c and S2c). HCD fragment ions connected to FA 18:1(9Z) loss from [POPC+Fe]²⁺ are 4 times more abundant than FA 16:0 ions, whereas FA 16:0 loss is only preferred by 1.3 over FA 18:1(9Z) loss for [OPPC+Fe]²⁺. The [FA 16:0+Fe-H]⁺ fragment ion is even lower in abundance than [FA 18:1(9Z)+Fe-H]⁺ in HCD experiments of [OPPC+Fe]²⁺ (Figure 2c).

To quantitatively analyze the *sn*-selectivity in tandem mass spectra of [PC+Fe]²⁺, the relative signal intensity of product ions associated with loss of one particular FA, e.g., all fragment ions connected to the FA 16:0 loss from OPPC, is calculated and compared to results obtained by PLA₂ digestion (Table 1).^{32,47} For example, FA 16:0 is attached to the *sn*-2 position in 97% abundance according to PLA₂ digestion of OPPC, whereas the relative abundance of FA 16:0 attached to the *sn*-2 position obtained from UVPD, CID, and HCD of [OPPC+Fe]²⁺ is 98%, 83%, and 56%, respectively. The decreased *sn*-2 selectivity of HCD and CID compared to UVPD is not only observed for OPPC but also for most other investigated PCs as summarized in Tables 1 and S-1. The mean absolute deviation (MD) and corresponding standard deviation (SD) are given in Table 1. UVPD results deviate by an average of 9% from PLA₂ digestion measurements, in contrast to the *sn*-isomeric purity obtained from CID and HCD that differ on average by 19% and 23% from PLA₂ results, respectively.

Especially for HCD, the fragment ion abundances appear to depend on the FA moieties. In particular, HCD of [OSPC+Fe]²⁺ results only in 54% fragment ions that are connected to FA 18:0 loss from the precursor but 88% of FA 18:1(9Z) product ions are obtained upon HCD of [SOPC+Fe]²⁺. This indicates that the double bond number of the FA in *sn*-1 is connected to selectivity of the *sn*-2 bond cleavage during HCD (Table 1) but no correlation between HCD results and FA

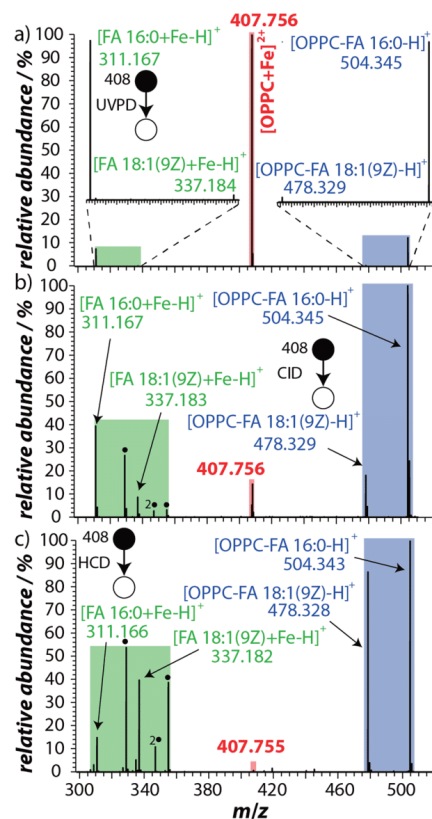


Figure 2. Tandem MS results for [PC 18:1(9Z)/16:0+Fe]²⁺ ([OPPC+Fe]²⁺) (red) activated by UVPD (a), ion trap CID (b), and HCD (c). Fragment ions assigned to [carboxylate+Fe]⁺ and [lipid-carboxylate]⁺ are highlighted in green and blue, respectively. Assigned sum formulas and experimental *m/z* values are included. ● H₂O attachment.

chain length is observed. The *sn*-selectivity differences between ion trap CID and HCD could be caused by the specifics of the ion activation in these collision activation methods. Whereas precursor ions but not product ions are resonantly excited in CID by multiple low energy (~tens eV) gas collisions,^{56,57} in HCD precursor and resulting fragment ions are activated by multiple collisions with tens to hundreds of eV.^{56,58} Consequently, ions activated with HCD can access higher energy dissociation pathways as compared to ion trap CID and HCD activation facilitates rearrangements and secondary fragmentation from primary fragment ions. Rearrangements or secondary fragmentation could be responsible for the decreased *sn*-selectivity in HCD compared to CID. In order to understand the HCD “*sn*-2 scrambling” effect for [PC+Fe]²⁺ in more detail, an increased number of authentic *sn*-isomer pairs is required. UVPD and CID results for [PC+Fe]²⁺, however, show no structure dependent change of *sn*-2 fragmentation

selectivity (Table 1). These results suggest that UVPD and CID can be used to deduce relative *sn*-isomer abundances.

Relative *sn*-Quantification using UVPD. Because *sn*-isomeric abundances obtained from UVPD have the smallest deviation to PLA₂ digestion results of all investigated tandem mass spectrometry methods, the ability to infer relative *sn*-isomer abundances from UVPD experiments without comparison to authentic standards was investigated. Results for PC 34:1 in yeast, porcine brain, and egg yolk polar lipid extracts analyzed in a shotgun approach are summarized in Table S-2. For egg yolk and porcine brain the relative POPC/OPPC abundance inferred from UVPD mass spectra is 97/3 and 49/51, respectively. This is in reasonable agreement with OzID results from Blanksby, Ellis, and co-workers that reported *sn*-abundances of 97/3, 61/39, and 57/43 for egg yolk, sheep brain, and rat brain (gray matter), respectively.^{15,45,46}

To further demonstrate the robustness of using UVPD of [PC+Fe]²⁺ to relatively quantify *sn*-isomers, a mouse pancreas polar lipid extract was analyzed in a shotgun approach after addition of FeCl₂. A typical mass spectrum is shown in Figure 3a and demonstrates the ability to detect [PC+Fe]²⁺ adducts in

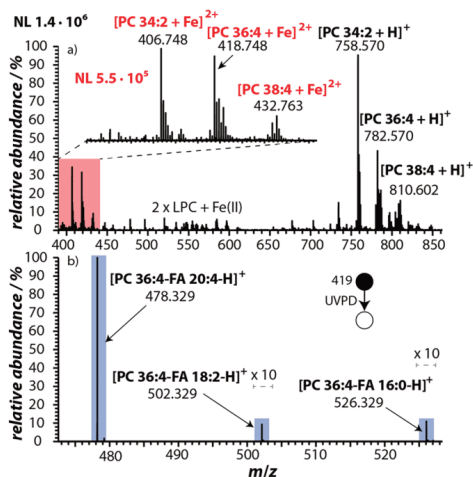


Figure 3. a) Shotgun ESI-FT-ICR-MS of mouse pancreas lipid extract. [PC+Fe]²⁺ ions are magnified in the inset and some signals are assigned and labeled with corresponding *m/z* values. b) UVPD of [PC 36:4+Fe]²⁺ in C57-J mouse pancreas lipid extract. Fragment ion signals are assigned and labeled with corresponding *m/z* values.

complex lipid mixtures. To investigate if all investigated ions are PCs and no isobaric PE impurities exist, MS³ experiments were performed. By fragmentation of [lipid-carboxylate]⁺ ions only the neutral loss of 59.073 Da associated with PCs was observed (Figure S-13). Additionally, no odd chain FAs were detected in MS² experiments. This confirms that all investigated ions are only PCs and not PEs. A total of 18 PCs were identified as listed in Table 2. The relative abundance was deduced for 12 PCs. For example, part of the UVPD mass spectrum of [PC 36:4 + Fe]²⁺ is shown in Figure 3b (Figure S-14 for overview). Fragment ion signals for FA 16:0, FA 18:2, and FA 20:4 loss are obtained indicating

Table 2. Compositional and Relative *sn*-Abundance Analysis of PCs in Mouse Pancreas Lipid Extract Using UVPD^{a,b,c}

precursor (<i>m/z</i>)	fragment ion <i>m/z</i>	assigned compounds ^d
PC 32:0 (394.748)	478.329	PC 16:0/16:0
PC 32:1 (392.741)	476.314	PC 16:1/16:0 (9%)
	478.329	PC 16:0/16:1 (91%)
PC 34:0 (408.764)	478.329	PC 16:0_18:0
	506.361	
PC 34:1 (407.756)	478.329	PC 16:0/18:1 (70%)
	504.345	PC 18:1/16:0 (30%)
PC 34:2 (406.748)	478.329	PC 16:0/18:2 (42%)
	502.329	PC 18:2/16:0 (58%)
PC 36:2 (420.764)	478.329	PC 16:0_20:2
	502.329	PC 18:1/18:1
	504.345	PC 18:0/18:2 (75%)
	506.361	PC 18:2/18:0 (25%)
	530.361	
PC 36:4 (418.748)	478.329	PC 16:0/20:4 (98%)
	502.329	PC 20:4/16:0 (2%)
	526.329	PC 18:2/18:2
PC 38:4 (432.764)	478.329	PC 16:0_22:4
	506.361	PC 18:0/20:4 (97%)
	526.329	PC 20:4/18:0 (3%)
	554.361	

^aRelative abundance of *sn*-isomers in brackets. Only [PC-FA-H]⁺ ions are listed. ^bAbsolute uncertainties of *sn*-isomer abundances are ±9% (Table 1) and relative errors of reported values are ±3%. ^cCompositions confirmed by CID-MS using [PC+Fe]²⁺. ^d*sn*-purity only determined if the signal-to-noise of all fragments was >5. Predominate FA moiety in *sn*-1 position is bold.

that PC 18:2/18:2, PC 16:0/20:4 (98%), and PC 20:4/16:0 (2%) are present. The 2% abundance of the latter is consistent with previously reported results for PC 16:0_20:4 that found relative *sn*-abundances for PC 20:4/16:0 of 5–10%.^{29,59}

If authentic standards are available, [PC+Fe]²⁺ fragment ion abundances from UVPD experiments and PLA₂ digestion results are linearly correlated (Figure S-15) and comparison between PLA₂ digestion and UVPD, thus, allows to relatively quantify PC *sn*-abundances.

Relative *sn*-Quantification using CID. To examine the capability to use [PC+Fe]²⁺ ions in MS² CID experiments for relative *sn*-quantification and account for the systematic offset between CID and PLA₂, POPC:OPPC mixtures with varying lipid standard mixing ratios were investigated. CID results for selected mixing ratios and the resulting correlation between signal intensities and solution composition obtained from PLA₂ digestion are shown in Figure 4. [PC+Fe]²⁺ fragment ions from [FA+Fe]⁺ loss are used for the analysis presented in Figure 4. Similar results are obtained for PCs with other FA composition than POPC/OPPC (Figure S-16) or by taking all *sn*-selective fragment ions into account (Figure S-17). The FA 16:0 fragment ion abundance (blue) increases with respect to the FA 18:1(9Z) loss ion signal abundance from Figure 4a to Figure 4c. This suggests that the amount of FA 16:0 attached to *sn*-2 of PC 34:1 increases, consistent with the increased amount of OPPC in the POPC/OPPC mixtures. By plotting the relative abundance of FA 16:0 associated fragment ions relative to all [PC-FA-H]⁺ product ions as a function of solution phase OPPC content, a linear correlation between the mass spectrometric signal abundances and solution *sn*-isomer abundance is identified (Figure 4d, Figure S-14). These results

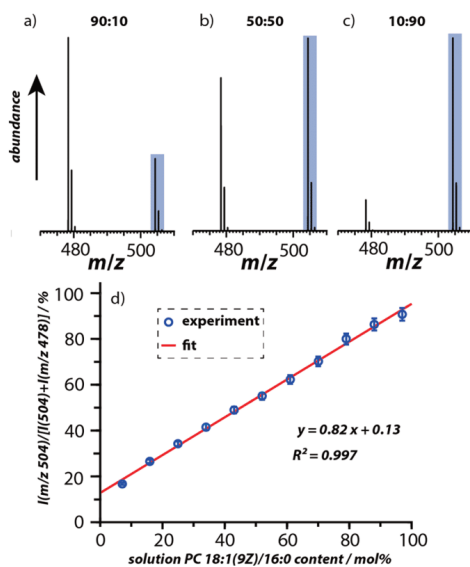


Figure 4. CID tandem mass spectra of PC 16:0/18:1(9Z):PC 18:1(9Z)/16:0 standard mixtures with a) 90:10, b) 50:50 and c) 10:90 mixing ratios. d) The m/z 504 fragment ion abundance with respect to the sum of m/z 504 and m/z 478 as a function of relative PC 18:1(9Z)/16:0 solution content obtained from PLA₂ digestions.

indicate that CID of $[\text{PC}+\text{Fe}]^{2+}$ can be used to relatively quantify *sn*-isomers if authentic standards are available.

To demonstrate that CID of $[\text{PC}+\text{Fe}]^{2+}$ is capable to relatively quantify *sn*-isomers in complex lipid mixtures, the abundance of PC 16:0/18:1 relative to PC 18:1/16:0 is investigated in pancreas lipid extracts from C57-J, ins2akita and db/db mice (Figure S-18) applying a shotgun approach. CID of $[\text{PC } 34:1+\text{Fe}]^{2+}$ from C57-J pancreas extract yields relative abundances of 73% and 27% for PC 16:0/18:1 and PC 18:1/16:0, respectively. This is in good agreement with *sn*-abundances from UVPD experiments (Table 2) for the same tissue extract. For ins2akita and db/db extracts, mouse models for type 1 and type 2 diabetes, the POPC/OPPC ratios are 59/41 and 68/32, respectively. Whereas the *sn*-isomeric abundance of PCs in a larger number of biological replicates for C57-J, ins2akita, and db/db mice organ extracts is currently investigated to enable interpretation of *sn*-isomeric abundances changes, these first results show the CID of $[\text{PC}+\text{Fe}]^{2+}$ can be used for relative quantification of *sn*-isomers in complex lipid extracts.

RESULTS AND DISCUSSION

In this study, formation of double charged metal ion-phospholipid complexes during ESI is reported for the first time. These ions were investigated with CID, HCD and UVPD tandem mass spectrometry. Most abundant formation of doubly charged phospholipid-metal ion complexes is observed for PC with Fe^{2+} . Fragmentation of $[\text{PC}+\text{Fe}]^{2+}$ ions containing different FAs with CID, HCD and UVPD results in exclusive dissociation of FA moieties and suppression of headgroup loss.

For every FA group, two abundant product ions, $[\text{PC}-\text{FA}-\text{H}]^+$ and $[\text{FA}+\text{Fe}-\text{H}]^+$, are obtained. The limit of detection for the fragment ions is determined to be 100 pM and consequently $[\text{PC}+\text{Fe}]^{2+}$ fragmentation enables sensitive PC compositional analysis in positive ion mode.

For authentic PC standards, comparison between PLA₂ digestion and tandem MS results reveal that CID and UVPD yield preferential dissociation of FAs from *sn*-2 positions, whereas HCD fragment ion abundances are not only influenced by the FA *sn*-position but also by the FA structure. The MD for UVPD is 9% enabling *sn*-isomeric abundance estimation without authentic standards. In contrast, lipid standards are required for the relative *sn*-isomer quantification with CID due to the MD of 19% compared to PLA₂ digestion results. By using a shotgun approach both tandem MS methods, UVPD and CID, enabled relative quantification of *sn*-isomers in complex lipid mixtures such as egg yolk, porcine brain, yeast and mouse pancreas lipid extracts.

The major advantage is the predominant $[\text{PC}+\text{Fe}]^{2+}$ ion formation by simply adding Fe^{2+} salts in low concentrations (~ 0.1 – $20 \mu\text{M}$) to ESI solutions. Formation of $[\text{PC}+\text{Fe}]^{2+}$ ions helps to mass spectrometrically separate PCs from other lipid classes. Potential PE impurities can be investigated by performing MS² and MS³ experiments to determine FA moieties and head groups, respectively. The currently not detected Fe^{2+} attachment to other glycerophospholipids, however, prevents their analysis as doubly charged metal ion complexes. CID or UVPD of $[\text{PC}+\text{Fe}]^{2+}$ ions from complex lipid mixtures readily reveal PC composition and *sn*-isomer abundance in positive ion mode without the need for prior isomer separation. To understand the differences between CID, HCD, and UVPD in more detail and deduce potential structures of $[\text{PC}+\text{Fe}]^{2+}$ as well as fragment ions, experiments with synthesized PC standards will be performed. Further optimization of the solvent composition to increase doubly charged lipid-metal ion complex abundances is currently underway in order to quantify PC *sn*-isomers in LC-MS/MS experiments using $[\text{PC}+\text{Fe}]^{2+}$ or to observe other glycerophospholipids– Fe^{2+} complexes.

ASSOCIATED CONTENT

Supporting Information

The Supporting Information is available free of charge on the ACS Publications website at DOI: 10.1021/acs.analchem.8b02731.

Additional UVPD, CID and HCD results for $[\text{PC}+\text{Fe}]^{2+}$ ions; mass spectrometric data for $[\text{PC}+\text{Fe}]^{2+}$ and $[\text{SM}+\text{Fe}]^{2+}$ using optimized ESI-MS parameters and employing different mass analyzers; NCE dependence of CID results, LOD estimation, and PLA₂ digestion data obtained with a LTQ-MS compared to UVPD, CID, and HCD results; and MS³ experiments, relative *sn*-isomer quantification results using UVPD and CID (PDF)

AUTHOR INFORMATION

Corresponding Author

*E-mail: Sven.Heiles@anorg.chemie.uni-giessen.de (S.H.)

ORCID

Sven Heiles: 0000-0003-3779-8071

Author Contributions

[‡]These authors contributed equally to this work. Experiments were performed by S.B. and P.E.; data were analyzed by S.B., P.E., and S.H.; S.H. supervised the project, designed the experiments, and wrote the manuscript. All authors have given approval to the final version of the manuscript.

Notes

The authors declare no competing financial interest.

ACKNOWLEDGMENTS

S.H. thanks the Fonds der chemischen Industrie for financial support through a Liebig fellowship. P.E. is grateful to the Fonds der chemischen Industrie for a doctoral scholarship. S.H. is grateful to Prof. Dr. B. Spengler (Analytical Chemistry, JLU Giessen) for his continuing support and insightful discussions. Financial support by the Bundesministerium fuer Bildung und Forschung, BMBF (project 0313442) and by the Deutsche Forschungsgemeinschaft (Sp 314/12-1) is gratefully acknowledged. All authors would like to thank Prof. Dr. T. Linn (Internal Medicine, Justus Liebig University Giessen, Germany) and his group for providing all mouse pancreas samples.

REFERENCES

- (1) Wenk, M. R. *Cell* **2010**, *143*, 888–895.
- (2) Shevchenko, A.; Simons, K. *Nat. Rev. Mol. Cell Biol.* **2010**, *11*, 593–598.
- (3) Gross, R. W.; Han, X. *Chem. Biol.* **2011**, *18*, 284–291.
- (4) Furse, S.; de Kroon, A. I. P. M. *Mol. Membr. Biol.* **2015**, *32*, 117–119.
- (5) Kimura, T.; Jennings, W.; Epan, R. M. *Prog. Lipid Res.* **2016**, *62*, 1, 75–92.
- (6) van Meer, G. *EMBO J.* **2005**, *24*, 3159–3165.
- (7) Wenk, M. R. *Nat. Rev. Drug Discovery* **2005**, *4*, 594–610.
- (8) Ersoy, B. A.; Tarun, A.; D'Aquino, K.; Hancer, N. J.; Ukomadu, C.; White, M. F.; Michel, T.; Manning, B. D.; Cohen, D. E. *Sci. Signaling* **2013**, *6*, ra64.
- (9) Sakai, H.; Kado, S.; Taketomi, A.; Sakane, F. *J. Biol. Chem.* **2014**, *289*, 26607–26617.
- (10) Balog, J.; Kumar, S.; Alexander, J.; Golf, O.; Huang, J.; Wiggins, T.; Abbassi-Ghadi, N.; Enyedi, A.; Kacska, S.; Kinross, J.; Hanna, G. B.; Nicholson, J. K.; Takats, Z. *Angew. Chem., Int. Ed.* **2015**, *54*, 11059–11062.
- (11) Kompauer, M.; Heiles, S.; Spengler, B. *Nat. Methods* **2017**, *14*, 90–96.
- (12) Kurczy, M. E.; Piehowski, P. D.; van Bell, C. T.; Heien, M. L.; Winograd, N.; Ewing, A. G. *Proc. Natl. Acad. Sci. U. S. A.* **2010**, *107*, 2751–2756.
- (13) Ostrowski, S. G.; van Bell, C. T.; Winograd, N.; Ewing, A. G. *Science* **2004**, *305*, 71–73.
- (14) Mouchlis, V. D.; Chen, Y.; McCammon, J. A.; Dennis, E. A. *J. Am. Chem. Soc.* **2018**, *140*, 3285–3291.
- (15) Paine, M. R. L.; Poad, B. L. J.; Eijkel, G. B.; Marshall, D. L.; Blanksby, S. J.; Heeren, R. M. A.; Ellis, S. R. *Angew. Chem.* **2018**, *130*, 10690.
- (16) Kuge, H.; Akahori, K.; Yagyu, K.-i.; Honke, K. *J. Biol. Chem.* **2014**, *289*, 26783–26793.
- (17) Han, X. *Lipidomics*; John Wiley & Sons, Inc: Hoboken, NJ, USA, 2016.
- (18) Ryan, E.; Reid, G. E. *Acc. Chem. Res.* **2016**, *49*, 1596–1604.
- (19) Mitchell, T. W.; Pham, H.; Thomas, M. C.; Blanksby, S. J. *J. Chromatogr. B: Anal. Technol. Biomed. Life Sci.* **2009**, *877*, 2722–2735.
- (20) Brown, S. H. J.; Mitchell, T. W.; Oakley, A. J.; Pham, H. T.; Blanksby, S. J. *J. Am. Soc. Mass Spectrom.* **2012**, *23*, 1441–1449.
- (21) Bou Khalil, M.; Hou, W.; Zhou, H.; Elisma, F.; Swayne, L. A.; Blanchard, A. P.; Yao, Z.; Bennett, S. A. L.; Figeys, D. *Mass Spectrom. Rev.* **2010**, *29*, 877–929.
- (22) Holcápek, M.; Liebisch, G.; Ekroos, K. *Anal. Chem.* **2018**, *90*, 4249–4257.
- (23) Brügger, B.; Erben, G.; Sandhoff, R.; Wieland, F. T.; Lehmann, W. D. *Proc. Natl. Acad. Sci. U. S. A.* **1997**, *94* (6), 2339–2344.
- (24) Ejsing, C. S.; Sampaio, J. L.; Surendranath, V.; Duchoslav, E.; Ekroos, K.; Klemm, R. W.; Simons, K.; Shevchenko, A. *Proc. Natl. Acad. Sci. U. S. A.* **2009**, *106*, 2136–2141.
- (25) Danne-Rasche, N.; Coman, C.; Ahrends, R. *Anal. Chem.* **2018**, *90*, 8093.
- (26) Murphy, R. C. *Tandem Mass Spectrometry of Lipids*; Royal Society of Chemistry: Cambridge, 2014.
- (27) Phaner, C. J.; Liu, S.; Ji, H.; Simpson, R. J.; Reid, G. E. *Anal. Chem.* **2012**, *84*, 8917–8926.
- (28) Rojas-Betancourt, S.; Stutzman, J. R.; Londry, F. A.; Blanksby, S. J.; McLuckey, S. A. *Anal. Chem.* **2015**, *87*, 11255–11262.
- (29) Nakanishi, H.; Iida, Y.; Shimizu, T.; Taguchi, R. *J. Biochem.* **2010**, *147*, 245–256.
- (30) Groessel, M.; Graf, S.; Knochenmuss, R. *Analyst* **2015**, *140*, 6904–6911.
- (31) Bowman, A. P.; Abzalimov, R. R.; Shvartsburg, A. A. *J. Am. Soc. Mass Spectrom.* **2017**, *28*, 1552–1561.
- (32) Maccarone, A. T.; Duldig, J.; Mitchell, T. W.; Blanksby, S. J.; Duchoslav, E.; Campbell, J. L. *J. Lipid Res.* **2014**, *55*, 1668–1677.
- (33) Ma, X.; Xia, Y. *Angew. Chem., Int. Ed.* **2014**, *53*, 2592–2596.
- (34) Stinson, C. A.; Xia, Y. *Analyst* **2016**, *141*, 3696–3704.
- (35) Murphy, R. C.; Okuno, T.; Johnson, C. A.; Barkley, R. M. *Anal. Chem.* **2017**, *89*, 8545–8553.
- (36) Wäldchen, F.; Becher, S.; Esch, P.; Kompauer, M.; Heiles, S. *Analyst* **2017**, *142*, 4744–4755.
- (37) Poad, B. L. J.; Zheng, X.; Mitchell, T. W.; Smith, R. D.; Baker, E. S.; Blanksby, S. J. *Anal. Chem.* **2018**, *90*, 1292–1300.
- (38) Thomas, M. C.; Mitchell, T. W.; Blanksby, S. J. *J. Am. Chem. Soc.* **2006**, *128*, 58–59.
- (39) Li, P.; Hoffmann, W. D.; Jackson, G. P. *Int. J. Mass Spectrom.* **2016**, *403*, 1–7.
- (40) Pham, H. T.; Ly, T.; Trevitt, A. J.; Mitchell, T. W.; Blanksby, S. J. *Anal. Chem.* **2012**, *84*, 7525–7532.
- (41) Pham, H. T.; Prendergast, M. B.; Dunstan, C. W.; Trevitt, A. J.; Mitchell, T. W.; Julian, R. R.; Blanksby, S. J. *Int. J. Mass Spectrom.* **2015**, *390*, 170–177.
- (42) Ryan, E.; Nguyen, C. Q. N.; Shiea, C.; Reid, G. E. *J. Am. Soc. Mass Spectrom.* **2017**, *28*, 1406–1419.
- (43) Klein, D. R.; Brodbelt, J. S. *Anal. Chem.* **2017**, *89*, 1516–1522.
- (44) Baba, T.; Campbell, J. L.; Le Blanc, J. C. Y.; Baker, P. R. S. *Anal. Chem.* **2017**, *89*, 7307.
- (45) Pham, H. T.; Maccarone, A. T.; Thomas, M. C.; Campbell, J. L.; Mitchell, T. W.; Blanksby, S. J. *Analyst* **2014**, *139*, 204–214.
- (46) Kozłowski, R. L.; Mitchell, T. W.; Blanksby, S. J. *Sci. Rep.* **2015**, *5*, 9243.
- (47) Ekroos, K.; Ejsing, C. S.; Bahr, U.; Karas, M.; Simons, K.; Shevchenko, A. *J. Lipid Res.* **2003**, *44*, 2181–2192.
- (48) Williams, P. E.; Klein, D. R.; Greer, S. M.; Brodbelt, J. S. *J. Am. Chem. Soc.* **2017**, *139*, 15681–15690.
- (49) Yoo, H. J.; Håkansson, K. *Anal. Chem.* **2011**, *83*, 1275–1283.
- (50) Ho, Y.-P.; Huang, P.-C.; Deng, K.-H. *Rapid Commun. Mass Spectrom.* **2003**, *17*, 114–121.
- (51) James, P. F.; Perugini, M. A.; O'Hair, R. A. J. *J. Am. Soc. Mass Spectrom.* **2008**, *19*, 978–986.
- (52) Liebisch, G.; Vizcaino, J. A.; Kofeler, H.; Trotzmüller, M.; Griffiths, W. J.; Schmitz, G.; Spener, F.; Wakelam, M. J. O. *J. Lipid Res.* **2013**, *54*, 1523–1530.
- (53) Matyash, V.; Liebisch, G.; Kurzchalia, T. V.; Shevchenko, A.; Schwudke, D. *J. Lipid Res.* **2008**, *49*, 1137–1146.
- (54) Becher, S.; Spengler, B.; Heiles, S. *Eur. J. Mass Spectrom.* **2018**, *24*, 54–65.

- (55) Hsu, F.-F.; Turk, J. *J. Am. Soc. Mass Spectrom.* **2003**, *14*, 352–363.
- (56) Wells, J. M.; McLuckey, S. A. *Methods Enzymol.* **2005**, *402*, 148–185.
- (57) Sleno, L.; Volmer, D. A. *J. Mass Spectrom.* **2004**, *39*, 1091–1112.
- (58) Olsen, J. V.; Macek, O.; Lange, O.; Makarov, A.; Horning, S.; Mann, M. *Nat. Methods* **2007**, *4*, 709–712.
- (59) Mitchell, T. W.; Ekroos, K.; Blanksby, S. J.; Hulbert, A. J.; Else, P. L. *J. Exp. Biol.* **2007**, *210*, 3440–3450.

IRMPD Spectroscopy of [PC (4:0/4:0) + M]⁺ (M = H, Na, K) and Corresponding CID Fragment Ions

Simon Becher, Giel Berden, Jonathan Martens, Jos Oomens, and Sven Heiles*

Cite This: *J. Am. Soc. Mass Spectrom.* 2021, 32, 2874–2884

Read Online

ACCESS |

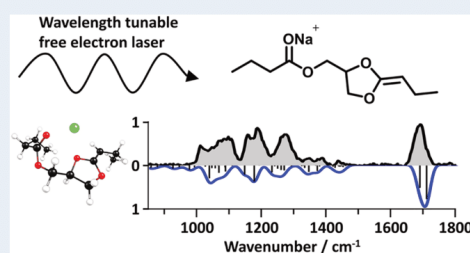
Metrics & More

Article Recommendations

Supporting Information

ABSTRACT: Glycerophospholipids (GPs) are highly abundant in eukaryotic cells and take part in numerous fundamental physiological processes such as molecular signaling. The GP composition of samples is often analyzed using mass spectrometry (MS), but identification of some structural features, for example, differentiation of stereospecific numbering (*sn*) isomers by well-established tandem MS (MS^2) methods, is challenging. In particular, the formation of 1,3-dioxolane over 1,3-dioxane intermediates proposed to be responsible for the *sn*-selectivity of these tandem MS strategies has not been validated by spectroscopic methods. In this work, we present infrared multiple photon dissociation (IRMPD) spectra of phosphatidylcholine (PC) ions [PC 4:0/4:0 + H/Na/K]⁺ and [PC 4:0/4:0 + Na/K – 183]⁺ fragments generated by electrospray ionization (ESI)-MS and collision-induced dissociation (CID), respectively. IRMPD spectra of protonated, sodiated, and potassiumated PC 4:0/4:0 differ in the phosphate- and ester-related bands, which are increasingly shifted to lower wavenumbers with higher adduct masses. Comparison of calculated and experimental IR spectra indicates the presence of multiple, two and one isomer(s) for [PC 4:0/4:0 + H]⁺, [PC 4:0/4:0 + Na]⁺, and [PC 4:0/4:0 + K]⁺, respectively. Isomers exhibiting pronounced *sn*-1 ester–ion interactions are computationally predicted to be energetically preferred for all species and are in line with experimental results. IRMPD spectra of [PC 4:0/4:0 + Na/K – 183]⁺ are presented and shed the first light on the fragment ion structures, rationalizing MS-based lipidomics strategies that aim to characterize the *sn*-isomerism of GPs.

KEYWORDS: lipids, IRMPD spectroscopy, tandem mass spectrometry, density functional theory, phosphatidylcholine, *sn*-isomerism



Downloaded via UNIV GIESSEN on December 2, 2021 at 08:39:26 (UTC).
See <https://pubs.acs.org/sharingguidelines> for options on how to legitimately share published articles.

INTRODUCTION

Glycerophospholipids (GPs) are essential biomolecules that are found in cell membranes, are involved in protein–protein interactions, and are crucial for molecular signaling.^{1–3} Changes in the lipid composition have been associated with cancer, diabetes, and cardiovascular disease.^{4–6} Recently, Munir et al. found that triglycerides (TG) and cholesterol esters (CE) are upregulated in the metastasis of the colon carcinoma cell line SW620 compared to the primary tumor cell line SW480.⁷ Moreover, fatty acid (FA) moieties of triglycerides and cholesterol esters showed an increase of saturation in SW620. The authors concluded that the FA composition is altered by cancer-induced modulation of the lipid metabolism. The lipid composition and FA content are tightly regulated and so is the abundance of specific lipid isomers, as demonstrated by Honke and co-workers.⁸ They were able to show that accumulation of 1-oleoyl-2-palmitoyl-*sn*-glycero-3-phosphocholine (PC 18:1/16:0, shorthand notations according to Liebisch et al.), a *sn*-isomer of PC 16:0/18:1 in protrusion tips and presynaptic areas of neuronal synapses of mouse brains occurs.⁹ The presence of PC 18:1/16:0 was explained as resulting from attraction of a dopamine trans-

porter and $G\alpha_o$ protein confinement by building a scaffold for these proteins. This highlights that GP structures and their changes are important to understand influences of lipids in diseases. In eukaryotic organisms, structural features typically important for GP properties are the headgroup, FA compositions, C=C double bond (DB) positions in the FAs, and permutations of FA moieties attached to the GP glycerol backbone leading to the so-called stereospecific numbering isomerism (*sn*-isomerism).

Mass spectrometry (MS) is arguably the method of choice to analyze lipid composition, abundance, and structures in the emerging field of lipidomics.^{10,11} This is because MS combines high analytical sensitivity with high sample throughput, outperforming other methods such as histochemical staining or nuclear magnetic resonance spectroscopy. However,

Received: September 6, 2021

Revised: October 14, 2021

Accepted: October 14, 2021

Published: November 1, 2021



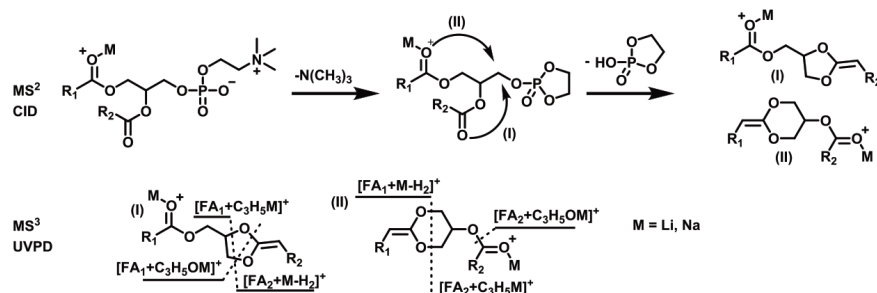


Figure 1. Proposed mechanism for headgroup loss of phosphatidylcholine (PC) in CID experiments by Turk et al., yielding (I) five- or (II) six-membered rings.¹⁹ Fragments found by Brodbelt and co-workers using CID-UVPD are assigned to the (I) six- and (II) five-membered intermediates.

structural discrimination in MS is challenging. Whereas identification of lipid FA compositions can routinely be performed in tandem MS (MS²) experiments, the development of advanced tandem MS methods is required to unveil detailed structural elements such as DB positions or *sn*-isomers.¹² Newly developed tandem MS tools allow some challenges associated with MS-based lipid structure elucidation to be overcome.¹³ For example, ozone-induced dissociation (OzID) leads to selective cleavage of the FA double bonds.¹⁴ Another method uses Paternò-Büchi (PB) reactions followed by collision-induced dissociation (CID) for DB position localization.¹⁵ Ultraviolet photodissociation (UVPD) yields DB position diagnostic fragment ions with or without prior derivatization.¹⁶ However, despite these improved methods, discrimination of *sn*-isomers in lipidomics remains challenging. While differences in bond dissociation energies often allow differential fragmentation of bonds in CID-MSⁿ, this approach does not work for GP analysis, presumably due to the similarity of the ester bond dissociation energies. Identification of *sn*-positions for GPs can be performed using phospholipase A₂ (PLA₂) for the selective cleavage of the FA in *sn*-2 position.¹⁷ After enzymatic cleavage, the fragments can be analyzed using liquid layer chromatography, gas chromatography, thin-layer chromatography, or MS. However, the enzymatic cleavage is time-consuming, especially in comparison to MS analysis. Additionally, Dennis and co-workers found that the selectivity of PLA₂ is influenced by the FA chain length and degree of saturation.¹⁸

Methods for *sn*-isomer identification were developed using lipid-metal adducts that influence the fragmentation for the analysis in MS².^{12,19,20} Our group contributed to this progress by developing a method using doubly charged metal ions, leading to selective cleavage of the FA in the *sn*-2 position in CID and UVPD experiments, with higher selectivity in UVPD.²¹ In our approach, fragments assigned to the loss of one FA are predicted to yield 2-hydroxy-1,3,2-dioxaphospholane 2-oxide or 2-hydroxy-1,3,2-dioxaphosphorinan 2-oxide derivatives (Figure S1). This contrasts with singly charged GP-alkali metal adducts for which the fragment used for *sn*-position analysis is associated with headgroup loss. Brodbelt and co-workers developed a CID-UVPD MS³ workflow for sodiated GP ions (Figure 1).¹⁶ They propose that CID leads to 1,3-dioxolane (I) derivatives, first described by Turk and co-workers.¹⁹ Subsequent cleavage of the dioxolane by UVPD results in [FA₁ + C₃H₅Na]⁺, [FA₂ + Na - H₂]⁺, and

[FA₁ + C₃H₅ONa]⁺ fragments, allowing the identification of *sn*-isomers. The complementary 1,3-dioxane (II) derivative fragment ion, however, could potentially yield fragment ions with *m/z* values similar to those originating from I. Therefore, the step that leads to *sn*-selective fragment ion formation depends on the initial headgroup loss event, which will ultimately dictate the structure and relative abundance of the resulting fragment ions.

To explore the fragmentation mechanism of GPs that are fundamental to lipidomics workflows that aim to assign *sn*-isomer abundances, gas-phase structures of precursor and fragment ions involved in these tandem MS steps are necessary. An approach to study the gas-phase structure of ions is infrared multiple-photon dissociation (IRMPD) spectroscopy, where gas-phase ions are irradiated with IR photons produced by a wavelength-tunable IR laser source.^{22,23} By recording the wavelength-dependent fragment ion intensities upon IR irradiation of the mass-to-charge-selected precursor ions, IRMPD spectra are obtained. The IRMPD spectra can identify ion functional groups and allow the assignment of gas-phase structures by comparing experimental with theoretical IR spectra. IRMPD spectroscopy has successfully been used to analyze gas-phase structures of small biomolecules, polycyclic aromatic hydrocarbons, nucleotide 5'-triphosphates, etc., as well as their complexes.^{24–30}

The aim of our study is to investigate the gas-phase structure of PC cations and corresponding CID fragments to contribute to the understanding of reported *sn*-selective fragment ion formation. To avoid influences of the acyl chain on spectroscopic results and minimize computational cost, the model lipid PC 4:0/4:0 was selected and gas-phase structures of [PC 4:0/4:0 + H/Na/K]⁺ precursors and [PC 4:0/4:0 + Na/K - 183]⁺ fragments were examined using IRMPD spectroscopy. IRMPD spectra are compared to theoretical vibrational spectra calculated at the B3LYP/pc-1 level of theory, revealing preferred H⁺, Na⁺, and K⁺ attachment sites in the precursor, and provide evidence for CID-generated headgroup loss fragment ion structures derived from alkali metal attached PC 4:0/4:0.

EXPERIMENTAL SECTION

Materials. All synthetic standards were commercially obtained and used without further purification. PC 4:0/4:0 was purchased from Avanti Polar Lipids Inc. (Alabaster, AL,

U.S.A.). MeOH, trifluoroacetic acid (TFA) ($\geq 99\%$), NaCl ($\geq 99\%$), and KCl ($\geq 99\%$) were purchased from Sigma-Aldrich (Munich, Germany).

Mass Spectrometry and IRMPD Spectroscopy. All experiments were performed with an Amazon ETD quadrupole ion trap mass spectrometer (Bruker, Bremen, DE), modified for IRMPD experiments and coupled to the free electron laser for infrared experiments (FELIX).³¹ For the experiments described here, settings for the MS were chosen to give an approximate 0.5 Da mass resolution for the precursor ion masses under investigation. Wavenumbers were calibrated using a grating spectrometer ($\pm 0.02 \mu\text{m}$), and observed vibrational band widths in the IRMPD spectra are typically on the order of 30 cm^{-1} .³² Precursor isolation was performed with a mass isolation window of $\Delta m/z = \pm 1$ centered around the precursor mass. Ions were generated using electrospray ionization (ESI), employing a flow rate of $2\text{--}3 \mu\text{L}\cdot\text{min}^{-1}$ with a voltage difference of approximately 4 kV in positive ion mode. The spray was nebulized using N_2 at 180 to $220 \text{ }^\circ\text{C}$ and $4\text{--}5 \text{ L}\cdot\text{min}^{-1}$.

MeOH solutions containing 1 vol % of TFA, 50 mol % of NaCl, or 50 mol % of KCl with 10^{-6} M PC 4:0/4:0 were used. IRMPD was performed with laser energies of $20\text{--}120 \text{ mJ}$ per pulse using $1\text{--}10$ pulses per mass spectrum. Pulse numbers were adjusted to maximize fragment signal intensities without reaching saturation of the IRMPD signal. FELIX was scanned from 850 to 1800 cm^{-1} in steps of 3 cm^{-1} . For each wavelength, six mass spectra were averaged. Wavelength-dependent IRMPD rates were derived from fragment ion intensities by the relation $k = -\ln(A/A_0)/t$, where A , A_0 , and t are the precursor ion abundance, the sum of precursor and product ion abundances, and the irradiation time, respectively. The $[\text{PC } 4:0/4:0 + \text{Na/K} - 183]^+$ fragments were generated using CID with collision energy settings of $0.2\text{--}0.5$ on the Amazon collision scale. Activation via IRMPD of CID fragments did not lead to detection of fragment ions, and instead, the loss of precursor ions was measured (thus A_0 derived from a spectral region without vibrational bands).

Computational Chemistry. Molecular gas-phase structures were optimized on the B3LYP/pc-1 level of theory using the Grimme DFT-D3 dispersion correction based on structures generated and preoptimized with molecular dynamics (MD) with the MMFF94s and GAFF force fields in Avogadro.^{33–36} All quantum-chemical calculations were performed with NWChem 6.8.1 and visualized using ChemCraft.³⁷ Gibbs free energies were calculated using electronic energies, scaled harmonic vibrations, and rotational constants at 298 K (G_{298}). Nine isomers were compared for each species, and the energetically most stable structures are discussed in detail. Attempts to optimize structures in which the added proton interacts with both esters and the phosphate converged to structures containing only interactions of the *sn*-1 ester and the proton (Figure S2). The predicted vibrational stick spectrum was convoluted with a Gaussian line shape function of 50 cm^{-1} fwhm. For wavenumbers $<1000 \text{ cm}^{-1}$, a scaling factor of 0.9808 was used, and for wavenumbers $>1000 \text{ cm}^{-1}$, a scaling factor of 0.9654 was used, as suggested by Wilson and co-workers.³⁸ The vibrational frequencies used for the calculation of the Gibbs energy (G_{298}) were scaled by 1.014 , as also suggested by Wilson and co-workers.

Whereas most bond lengths for related systems were obtained from literature reports, bond lengths between the NMe_3 groups and the esters were derived from benchmark

calculations based on tetramethylammonium methyl butyrate (Figure S3).

RESULTS AND DISCUSSION

IRMPD Spectroscopy $[\text{PC } 4:0/4:0 + \text{H/Na/K}]^+$. As the charge carrier has the potential to influence the abundances and identities of tandem MS fragment ions of lipids, we first explored the possible structural variations of $[\text{PC } 4:0/4:0 + \text{H/Na/K}]^+$ precursor ions. For this purpose, IRMPD spectra of $[\text{PC } 4:0/4:0 + \text{H/Na/K}]^+$ were recorded, and the results are shown in Figure 2. IRMPD fragment ion m/z

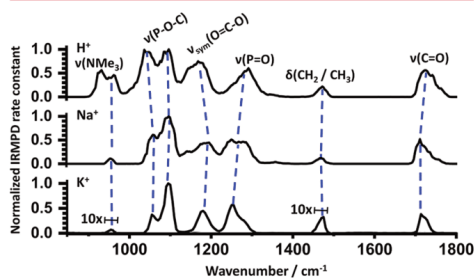


Figure 2. IRMPD spectra of $[\text{PC } 4:0/4:0 + \text{M}]^+$, with $\text{M} = \text{H}, \text{Na}, \text{K}$. Bands are assigned based on literature values.^{12,19} The influence of the charge carrier identity on band position is shown by dashed blue lines.

z values did not depend on IR wavelength, and representative tandem mass spectra are shown in Figures S4–S6. IRMPD fragment ions are in line with CID-MS² literature reports of protonated, sodiated, or potassiumated PCs. Additionally, fragment ion and IRMPD spectra intensities are lower for sodiated/potassiumated lipids than for protonated lipids, consistent with tandem MS results of these lipids. The signal at m/z 184 is the major fragment of $[\text{PC } 4:0/4:0 + \text{H}]^+$, and alkali-metal-containing precursors are dominated by $[\text{C}_2\text{H}_5\text{O}_4\text{P} + \text{M}]^+$ ($\text{M} = \text{Na}$ (m/z 147), K (m/z 163)) ions.^{12,19} Irradiation of the sodiated PC 4:0/4:0 additionally resulted in neutral loss of the headgroup and sodium (m/z 215), the headgroup (m/z 237), and one fatty acid (m/z 273).

The IRMPD spectra shown in Figure 2 were compared to literature reports in order to assign features and characterize the impact of the charge carrier on band positions. The bands at 1725 cm^{-1} (H^+), 1710 cm^{-1} (Na^+), and 1713 cm^{-1} (K^+) are assigned to the $\nu(\text{C}=\text{O})$ stretching vibrations. These experimental bands are red-shifted compared to free ester bonds ($1750\text{--}1725 \text{ cm}^{-1}$) for all three adducts, indicating a weakening of the ester $\text{C}=\text{O}$ bonds most likely due to interactions with the charge carriers.³⁹ Bands assigned to the $\nu_{\text{sym}}(\text{O}=\text{C}-\text{O})$ mode are at 1172 , 1195 , and 1181 cm^{-1} for H^+ , Na^+ , and K^+ in the experimental spectrum, respectively. All $\nu_{\text{sym}}(\text{O}=\text{C}-\text{O})$ bands are in good agreement with reported literature values of solid- and liquid-state IR ($1300\text{--}1000 \text{ cm}^{-1}$).⁴⁰ In contrast to the red shift of $\nu(\text{C}=\text{O})$ signals, the $\nu_{\text{sym}}(\text{O}=\text{C}-\text{O})$ signals are blue-shifted in the spectra of Na^+ and K^+ compared to H^+ and for Na^+ and K^+ narrowed by 15 and 5 cm^{-1} relative to H^+ . The findings of $\nu(\text{C}=\text{O})$ and $\nu_{\text{sym}}(\text{O}=\text{C}-\text{O})$ indicate that the ester bonds are strongly

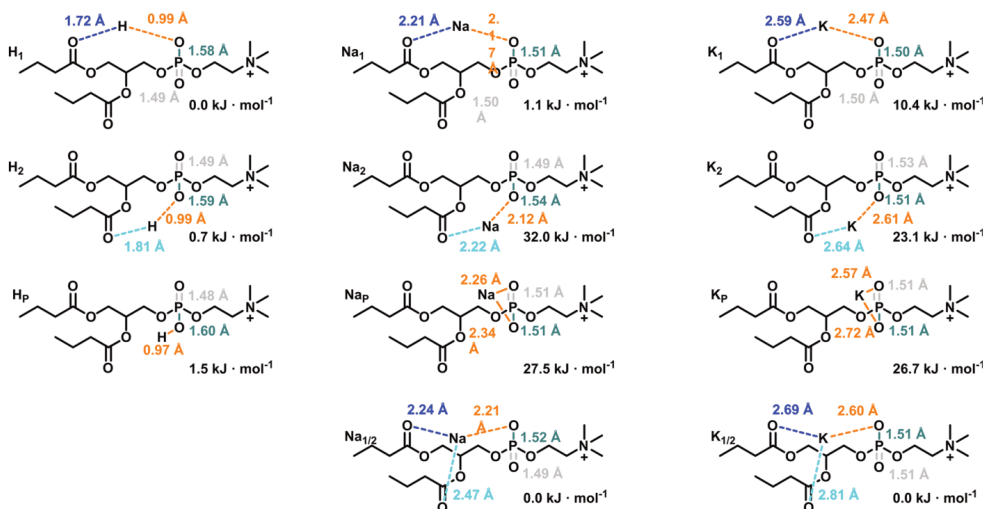


Figure 3. Lowest-energy isomers of $[\text{PC } 4:0/4:0 + \text{H}]^+$, $[\text{PC } 4:0/4:0 + \text{Na}]^+$, and $[\text{PC } 4:0/4:0 + \text{K}]^+$. Computed bond lengths of charge carrier to phosphate oxygen (orange), charge carrier to carbonyl ester (*sn*-1 blue and *sn*-2 cyan), phosphate oxygen double bond (gray), ion binding phosphate oxygen to phosphorus (azure), and ΔG_{298} relative to the lowest-energy isomer are included.

influenced by the adduct identity, providing strong evidence that H^+ , Na^+ , and K^+ interact with the carbonyl ester groups.

Bands at 1472 cm^{-1} (H^+), 1469 cm^{-1} (Na^+), and 1476 cm^{-1} (K^+) are consistent with literature values of freely vibrating $\delta(\text{CH}_2)/\delta(\text{CH}_3)$ groups in solid- and liquid-state IR ($1470\text{--}1400 \text{ cm}^{-1}$) and differ only by 7 cm^{-1} .⁴⁰ Therefore, interactions of the charge carrier with the FA chains is likely minimal.

Bands assigned to $\nu(\text{P}=\text{O})$ (H^+ , $1325\text{--}1236 \text{ cm}^{-1}$; Na^+ , $1291\text{--}1248 \text{ cm}^{-1}$; K^+ , $1291\text{--}1231 \text{ cm}^{-1}$) are in good agreement with theoretical results of neutral diethylphosphate (DEP, 1295 cm^{-1}) and $\text{DEP} - \text{H} + \text{Na}$ (1240 cm^{-1}) reported by Rodgers and co-workers.⁴¹ In our data, the red-shifted shoulder of the $\nu(\text{P}=\text{O})$ signals in the spectra of Na^+ indicate a weakening of the $\text{P}=\text{O}$ bond most likely due to $\text{P}=\text{O}\cdots\text{Na}^+$ interactions. In the study of DEP-related ions, an additional band at 1025 cm^{-1} , which was identified as splitting of the $\nu(\text{P}-\text{O}-\text{C})$ mode by coupling of the alkoxy and oxo stretching modes in IRMPD spectra of $[\text{DEP} - \text{H} + 2\text{Na}]^+$, is consistent with shoulders at 1090 cm^{-1} for H^+ , 1099 cm^{-1} for Na^+ , and 1097 cm^{-1} for K^+ with a maximum deviation of 26 cm^{-1} . Compared with $\nu(\text{P}=\text{O})$ and the band resulting from coupling of the alkoxy and oxo stretching, relative band intensities of $\nu(\text{P}-\text{O}-\text{C})$ decrease with higher atom radii of the charge carrier. The coupling mode and the shifts of phosphate-assigned bands are a strong indication for binding of the charge carriers to the PO_4 unit of PC 4:0/4:0.

Vibrational modes involving the N-C bonds of NMe_3 are related to the bands at $965/935 \text{ cm}^{-1}$ (H^+), 956 cm^{-1} (Na^+), and 957 cm^{-1} (K^+), all within or close to the range reported in the literature ($960\text{--}940 \text{ cm}^{-1}$).⁴² All modes except this N-C vibration of the NMe_3 group give rise to the same number of bands in the spectra of $[\text{PC } 4:0/4:0 + \text{H}/\text{Na}/\text{K}]^+$, so that the gas-phase structures of the three systems are likely similar. The presence of a second band in $[\text{PC } 4:0/4:0 + \text{H}]^+$ could indicate

a second gas-phase isomer. All other vibrations involving NMe_3 are located at the same wavenumbers for all adducts, similar to the CH_2/CH_3 bands, so that significant intramolecular interactions involving these groups are unlikely. On the other hand, strong evidence for interactions with the phosphate and ester groups is suggested by the shift of their IR bands in Figure 2. Therefore, only isomers with interactions of H^+ , Na^+ , or K^+ with the phosphate and the esters will be considered for in-depth analysis.

Structures of $[\text{PC } 4:0/4:0 + \text{H}/\text{Na}/\text{K}]^+$. To understand gas-phase structures of PC 4:0/4:0 adducts and differences in the fragmentation pathways, density functional theory (DFT) calculations were conducted. Structures of the most stable conformers are schematically shown in Figure 3 (detailed structures in Figures S7–S9) and grouped into four categories. One group of structures exhibits bonding interactions of the charge carrier with the phosphate and the *sn*-1 carbonyl oxygen (H_1 , Na_1 , K_1). In the second group, the *sn*-2 carbonyl oxygen is involved instead of the *sn*-1 (H_2 , Na_2 , K_2). In some structures, the ion is not coordinated to ester groups but only to the phosphate (H_p , Na_p , K_p). In the final set of structures, both ester carbonyl oxygens as well as the phosphate bind to Na^+ or K^+ ($\text{Na}_{1/2}$, $\text{K}_{1/2}$). As a simplistic measure for the strength of interactions between functional groups and the ions, distances between the charge carrier and the ester carbonyl oxygens ($M_{\text{O } sn-1}$ in blue and $M_{\text{O } sn-2}$ in cyan), the phosphate oxygen ($M_{\text{O } p}$ in orange), the phosphate oxygen double bond ($P_{\text{P}=\text{O}}$ in gray), and the phosphate oxygen length ($P_{\text{O}-M}$ in azure) are given in Figure 3 (Table S1). Interactions between the choline nitrogen and the ester bonds are also discussed in terms of their distance ($N_{\text{O } sn-1}/N_{\text{O } sn-2}$).

The energetically most stable $[\text{PC } 4:0/4:0 + \text{H}]^+$ isomer is H_1 , with H_2 and H_p being higher in energy by 0.7 and 1.5 $\text{kJ}\cdot\text{mol}^{-1}$, respectively. In H_1 , the hydrogen bonding dihedral angle is 170.08° . The charge-carrying NMe_3 residue is

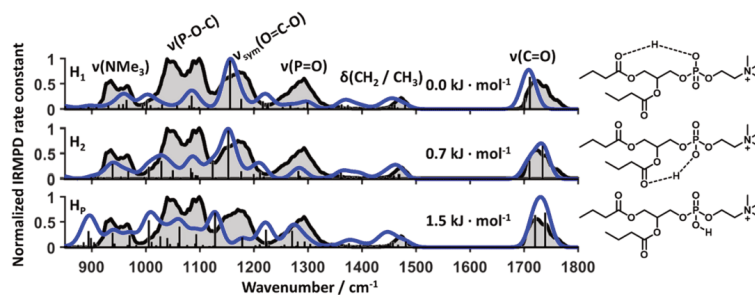


Figure 4. Lowest-energy isomers of $[\text{PC } 4:0/4:0 + \text{H}]^+$ and corresponding predicted vibrational spectra compared to the experimental IRMPD spectrum. Experimental and theoretical bands are shown in black with gray areas and blue, respectively. Predicted ΔG_{298} values relative to the lowest-energy isomer are included.

coordinated by the *sn*-2 ester. In H_2 , the interaction of the proton with the *sn*-2 ester carbonyl oxygen only allows coordination of NMe_3 with the *sn*-1 ester. In H_p , the $\text{M}_{\text{O-P}}$ bond is shortened by 0.02 Å compared to that in H_1 and H_2 . The charge-carrying choline group is oriented toward the *sn*-1 and *sn*-2 ester carbonyl oxygen.

To put these bond lengths into perspective and measure the influence of charge-carrier lipid interactions and lipid structures, computed results can be compared to benchmark values, as outlined in the Experimental Section. The benchmark bond length for NMe_3 -carbonyl ester oxygen is 3.39 Å. The H_1 , H_2 , and H_p isomers, however, have NMe_3 -carbonyl ester oxygen bond lengths well above 3.75 Å. This indicates that the influence of the charged NMe_3 group on the ester groups is likely negligible. Lommerse et al. described that hydrogen bonding to ester moieties has typical bond lengths from 1.90 to 1.95 Å.⁴³ Dihedral angles of the proton, the donor, and the acceptor oxygen approach 180°, with increasing H-bonding strength.⁴⁴ The H-bonding distances of 1.72 Å and the O-H...O dihedral angle of 170.08° indicate strong hydrogen bonding in H_1 , which is weakened in H_2 (166.60°, 1.81 Å) and absent in H_p . This emphasizes a stabilizing influence of the hydrogen bonding in H_1 and H_2 . The $\text{P}_{\text{O-M}}$ and $\text{P}_{\text{P=O}}$ lengths of 1.60 and 1.48 Å in H_p are elongated compared to literature values (1.56 Å $\text{P}_{\text{O-M}}$ /1.46 Å $\text{P}_{\text{P=O}}$).⁴⁵ However, energy differences between the protonated PC 4:0/4:0 isomers of a maximum 1.5 $\text{kJ}\cdot\text{mol}^{-1}$ suggest that multiple isomers could coexist under our experimental conditions.

In contrast to the protonated species, sodium directly interacts with the phosphate group and both ester carbonyl oxygens in the energetically most stable $\text{Na}_{1/2}$ isomer. Energy differences relative to the most stable $\text{Na}_{1/2}$ isomer are 1.1 $\text{kJ}\cdot\text{mol}^{-1}$ (Na_1), 32.0 $\text{kJ}\cdot\text{mol}^{-1}$ (Na_2), and 27.5 $\text{kJ}\cdot\text{mol}^{-1}$ (Na_p). No coordination of the positively charged NMe_3 toward the partially negatively charged groups such as the phosphate or the esters is observed in $\text{Na}_{1/2}$. In comparison to the literature values (1.54 Å ($\text{P}_{\text{O-M}}$); 1.46 Å ($\text{P}_{\text{P=O}}$)), there is an elongation of $\text{P}_{\text{P=O}}$ in all isomers, whereas the $\text{P}_{\text{O-M}}$ is shorter or equal to literature values.⁴⁵ This indicates that sodium-phosphate interactions result in strengthened P-O bonds at the cost of a weaker P=O bond. The $\text{M}_{\text{O-}sn-1}$ (2.24 Å) and $\text{M}_{\text{O-P}}$ (2.21 Å) lengths in $\text{Na}_{1/2}$ are close to those of the Na_1 isomer (2.21 Å $\text{M}_{\text{O-}sn-1}$ /2.17 Å $\text{M}_{\text{O-P}}$). Hence, the $\text{Na}_{1/2}$ isomer can be interpreted as a Na_1 species with additional interactions involving the *sn*-2 ester. The interactions of the sodium with

the *sn*-1 ester can be identified as the major stabilizing effect, as isomers missing this interaction are considerably destabilized compared to $\text{Na}_{1/2}$ and Na_1 .

Results for $[\text{PC } 4:0/4:0 + \text{K}]^+$ are comparable to those with sodium. The $\text{K}_{1/2}$ isomer is energetically favored by 10.4, 23.1, and 26.7 $\text{kJ}\cdot\text{mol}^{-1}$ compared to K_1 , K_2 , and K_p , respectively. Similar to sodium, potassium is chelated by two phosphate oxygens in K_p with equal $\text{P}_{\text{P=O}}$ and $\text{P}_{\text{O-M}}$ lengths. The $\text{M}_{\text{O-}sn-1}$ length of the $\text{K}_{1/2}$ isomers is shorter than the $\text{M}_{\text{O-}sn-2}$ length. This is in line with the $\text{Na}_{1/2}$ species and the isomer can also be interpreted as K_1 with additional interactions to the *sn*-2 ester. Supporting the findings for Na^+ , $\text{K}_{1/2}$ and K_1 yield the two lowest-energy isomers. This strongly indicates the presence of a metal-*sn*-1 binding motif in $[\text{PC } 4:0/4:0 + \text{Na/K}]^+$ gas-phase structures.

In general, our computations predict that interactions of the charge-carrying NMe_3 group with electron-rich groups such as the phosphate or the esters are weaker than $\text{H}^+/\text{Na}^+/\text{K}^+$ interactions with these groups. Coordination of $\text{H}^+/\text{Na}^+/\text{K}^+$ to the *sn*-1 ester is preferred over coordination to the *sn*-2 ester, with the energetically most stable isomers of the alkali metals showing further stabilization by metal-*sn*-2 ester carbonyl oxygen interactions. Whereas $\text{P}_{\text{O-M}}$ lengths decrease with higher ion radii from 1.59 Å (H^+) on average to 1.52 Å (Na^+) and 1.51 Å (K^+), $\text{P}_{\text{P=O}}$ lengths increase from 1.49 Å (H^+) on average to 1.50 Å (Na^+) and 1.51 Å (K^+). Overall, shorter $\text{P}_{\text{O-M}}$ and longer $\text{P}_{\text{P=O}}$ lengths in the alkali adducts indicate stronger interactions compared to those with H^+ . This is also reflected in energy differences of maximum 1.5 $\text{kJ}\cdot\text{mol}^{-1}$ but 32.0 and 26.7 $\text{kJ}\cdot\text{mol}^{-1}$ in Na^+ and K^+ , respectively.

Comparison of the Experimental and Theoretical IRMPD Spectra for $[\text{PC } 4:0/4:0 + \text{H/Na/K}]^+$. To develop a detailed picture of the $[\text{PC } 4:0/4:0 + \text{H}]^+$ gas-phase structure, experimental and theoretical results for different isomers are compared in Figure 4 (experiment in black, theory in blue). Band positions for H_1 , H_2 , and H_p are listed in Table S2.

The experimental feature above 1700 cm^{-1} assigned to ester $\nu(\text{C=O})$ vibrations by comparison to literature values is broader (71 cm^{-1}) compared to that of typical carbonyl bands (50 cm^{-1}).⁴⁶ The theoretical spectra for all isomers consist of two distinct $\nu(\text{C=O})$ bands, one for each ester. In H_1 , the predicted bands are blue-shifted compared to the experimental band by about 25 cm^{-1} . The predicted ester $\nu(\text{C=O})$ bands for the H_2 and H_p isomers are within the width of the experimental $\nu(\text{C=O})$ feature. Combination of more than one

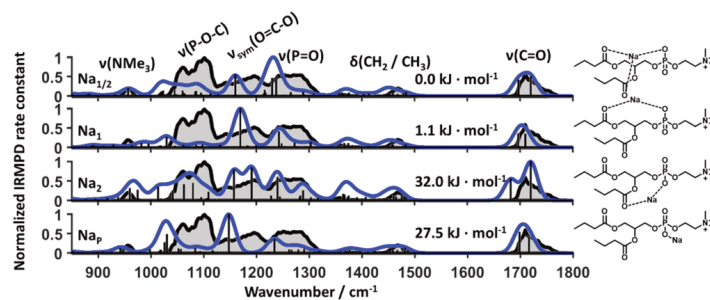


Figure 5. Lowest-energy isomers of $[\text{PC } 4:0/4:0 + \text{Na}]^+$ and corresponding predicted vibrational spectra compared to the experimental IRMPD spectrum. Experimental and theoretical bands are shown in black and blue, respectively. Predicted ΔG_{298} values relative to the lowest-energy isomer are included.

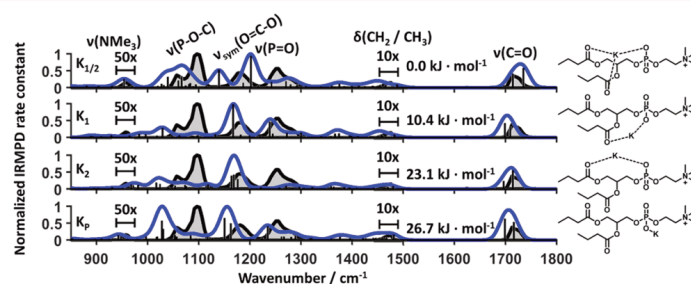


Figure 6. Lowest-energy isomers of $[\text{PC } 4:0/4:0 + \text{K}]^+$ and corresponding predicted vibrational spectra compared to the experimental IRMPD spectrum. Experimental and theoretical bands are shown in black with gray areas and blue, respectively. Predicted ΔG_{298} values relative to the lowest-energy isomer are included.

H^+ isomer or different *sn*-1 and *sn*-2 ester vibrational modes could explain the broadening of the experimental $\nu(\text{C}=\text{O})$ band. The $\nu(\text{O}=\text{C}-\text{O})$ signals at roughly 1155 cm^{-1} in H_1 and H_2 are in good agreement with experimental signals at $1182\text{--}1167 \text{ cm}^{-1}$, but the red-shifted $\nu(\text{O}=\text{C}-\text{O})$ mode of H_p is at odds with the experimental band position. The experimental band at 1472 cm^{-1} is within the theoretically predicted $\delta(\text{CH}_2/\text{CH}_3)$ range for all isomers. Experimental bands in the wavenumber range of the phosphate modes are close to the $\nu(\text{P}=\text{O})$, $\nu(\text{P}-\text{O}-\text{C})$, and $\nu(\text{P}-\text{O}-\text{C})/\nu(\text{P}=\text{O})$ bands predicted by theory for all three isomers. Bands at 965 and 935 cm^{-1} in the experimental spectrum are in line with the $\nu(\text{NMe}_3)$ mode predicted for the H_1 (964 cm^{-1}), the H_2 (939 cm^{-1}), and the H_p (938 cm^{-1}) isomers.

Predicted phosphate signal intensities differ for all three isomers compared to the experiment. However, the experimental data for $[\text{PC } 4:0/4:0 + \text{H}]^+$ agrees best with calculated band positions of the $\nu(\text{C}=\text{O})$ mode of the H_1 and H_2 isomers. The bands at 965 and 935 cm^{-1} are not present in the spectrum of a single isomer but are most likely the consequence of the presence of multiple isomers. Coexistence of the isomers is also likely due to the intramolecular mobility of protons known for other biomolecules.^{47,48} The $\nu(\text{C}=\text{O})$ and $\nu(\text{NMe}_3)$ bands of H_1 , H_2 , and H_p are all consistent with the experimental data. Therefore, possibly all isomers contribute to the experiment spectrum.

Predicted vibrational spectra of the $[\text{PC } 4:0/4:0 + \text{Na}]^+$ isomers are shown along with the experimental IRMPD spectrum in Figure 5 (band positions in Table S3). Experimental spectra and theoretical spectra of Na_1 , Na_2 , Na_p , and $\text{Na}_{1/2}$ with ΔG_{298} values are shown in black and blue, respectively.

The spectrum of the sodiated PC 4:0/4:0 lipid shows bands for ester- and phosphate-related vibrational modes, exceeding band widths reported for phosphate (60 cm^{-1}) and ester species (50 cm^{-1}) in the literature.^{41,49} Theoretical bands that are close to the experimental band at $1746\text{--}1697 \text{ cm}^{-1}$ are the combination of *sn*-1 and *sn*-2 $\nu(\text{C}=\text{O})$ modes, similar to the protonated species. In contrast to the predicted H^+ spectra, bands assigned to $\nu_{\text{sym}}(\text{O}=\text{C}-\text{O})$ are split into one band for each ester in the calculated spectra of $\text{Na}_{1/2}$ (1238 cm^{-1} *sn*-1, 1160 cm^{-1} *sn*-2), Na_1 (1184 cm^{-1} *sn*-1, 1170 cm^{-1} *sn*-2), Na_2 (1158 cm^{-1} *sn*-1, 1191 cm^{-1} *sn*-2), and Na_p (1234 cm^{-1} *sn*-1, 1280 cm^{-1} *sn*-2) isomers. The presence of a second $\nu_{\text{sym}}(\text{O}=\text{C}-\text{O})$ band in all spectra of Na^+ isomers indicates stronger interactions of the sodium to the ester compared to the proton. However, the broad nature of the experimental band challenges differentiation of the isomers based on this vibrational mode. All PC 4:0/4:0 isomers of Na^+ show bands near 1469 and 1358 cm^{-1} corresponding to CH_2/CH_3 vibrations. The feature assigned to $\nu(\text{P}=\text{O})$ in the IRMPD spectrum agrees with calculated signals of the $\text{Na}_{1/2}$, Na_1 , and Na_2 modes. Na_p (1151 cm^{-1}) is the only isomer predicted to

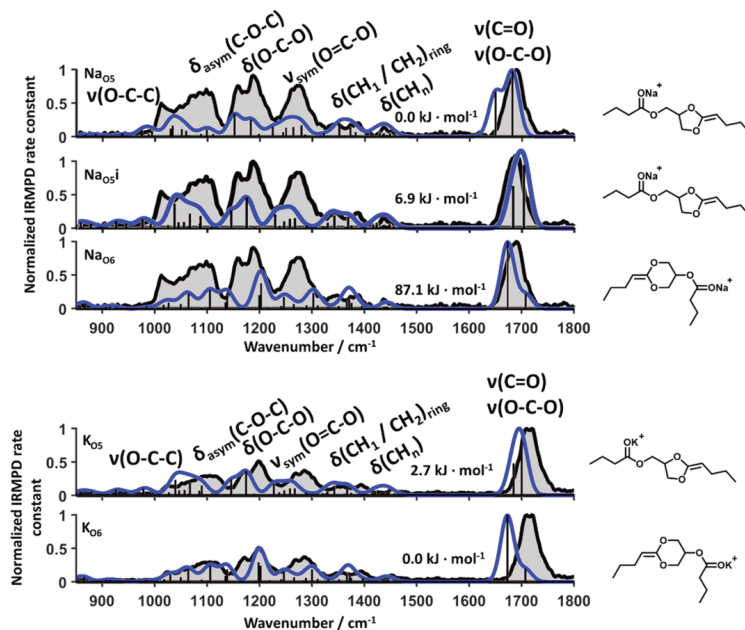


Figure 7. Lowest-energy isomers of $[\text{PC } 4:0/4:0 - 183 + \text{Na/K}]^+$ five- and six-membered rings and IRMPD spectra. Experimental and theoretical spectra are shown in black and blue, respectively. Bands are assigned according to literature values. ΔG_{298} values relative to the lowest-energy isomer are included.

exhibit a 60 cm^{-1} red-shifted band compared to the experiment. The two bands in the experiment at 1099 and 1060 cm^{-1} are reproduced in all four simulated spectra and are due to $\nu(\text{P-O-C})$ and $\nu(\text{P-O-C})/\nu(\text{P=O})$ coupled vibrations. All isomers have $\nu(\text{NMe}_3)$ bands in the range of the experimental band. However, broadening of the $\nu(\text{P=O})$ and the $\nu_{\text{sym}}(\text{O=C-O})$ band suggests the presence of more than one isomer. In line with the findings for $[\text{PC } 4:0/4:0 + \text{H}]^+$, the aliphatic bands and the NMe_3 group are not influenced by the binding of sodium.

The red-shifted $\nu(\text{C=O})$ shoulder in the theoretical spectrum of Na_2 is at odds with the presence of this structure; the same is true for the broad band at 1084 cm^{-1} and the lack of absorption near $1206\text{--}1167 \text{ cm}^{-1}$ in Na_p . The higher energy differences between the isomers and the spectroscopic match of most bands point toward the predominant formation of $\text{Na}_{1/2}$ and Na_1 isomers. However, the presence of a single isomer is unlikely, as indicated by $\nu(\text{P=O})$ and $\nu_{\text{sym}}(\text{O=C-O})$ modes with band widths of $\geq 50 \text{ cm}^{-1}$.

Similar to the sodium isomers, $\text{K}_{1/2}$ is the energetically most stable potassium isomer (Figure 6, band positions in Table S4). The ΔG_{298} values between the isomers further increase compared to H^+ and Na^+ .

The experimental band at 1713 cm^{-1} coincides with $\nu(\text{C=O})$ bands of all isomers predicted for the *sn-1/sn-2* esters. The theoretical $\nu(\text{C=O})$ bands of all isomers but $\text{K}_{1/2}$ are red-shifted compared to those in the experiment. Experimental bands assigned to $\nu_{\text{sym}}(\text{O=C-O})$ are in line with computed $\nu_{\text{sym}}(\text{O=C-O})$ band positions. Wavenumbers of CH_2/CH_3

vibrations in the calculated spectra are in good agreement with the experimental signals at 1471 and 1351 cm^{-1} . The experimental band at 1181 cm^{-1} can be explained by $\nu(\text{P=O})$ signals of all isomers. Wavenumbers of computed $\nu(\text{P-O-C})$ and $\nu(\text{P-O-C})/\nu(\text{P=O})$ bands of $\text{K}_{1/2}$ fit the experimental findings. The same is true for the band at 957 cm^{-1} , which is best reproduced by the $\nu(\text{NMe}_3)$ modes of $\text{K}_{1/2}$. In general, all bands are sharper in the potassium adduct compared to the proton and the sodium (e.g., $\nu(\text{C=O})$ widths 39 cm^{-1} $\text{H}/54 \text{ cm}^{-1}$ $\text{Na}/25 \text{ cm}^{-1}$ K) adducts, suggesting that one isomer dominantly contributes to the experimental spectrum. This is supported by ΔG_{298} higher than that of both other adducts.

Based on the experimentally assigned $\nu(\text{C=O})$ and $\nu(\text{NMe}_3)$ bands and the small energy differences of $\sim 1.5 \text{ kJ}\cdot\text{mol}^{-1}$ between isomers, multiple isomers involving *sn-1* and *sn-2* protonated esters for $[\text{PC } 4:0/4:0 + \text{H}]^+$ and interconversion between these isomers are likely. Additionally, the dominant loss of the charged headgroup prohibits the observation of neutral *sn*-specific fragments for $[\text{PC } (4:0/4:0) + \text{H}]^+$. Therefore, differentiation between the ester groups and selective formation of a single fragment ion isomer is not facilitated by the precursor structure. This is in line with literature reports, where *sn*-selectivity is not, or to a limited extent, reported for protonated lipids.^{16,50,51} In contrast to the protonated species, predicted spectra and energy differences for the sodium and potassium isomers indicate the presence of two ($\text{Na}_1/\text{Na}_{1/2}$) or one structure ($\text{K}_{1/2}$), with stronger interactions of the metal ion with the *sn-1* ester in $\text{Na}_{1/2}$ and

$K_{1/2}$. Preferential interaction with one ester potentially explains the selective FA cleavage in the *sn*-2 position, as reported in the literature.^{16,19} Factors impacting the fragmentation reactions are the stabilization of the phosphate as a leaving group, reduction of the nucleophilic character of the ester by ester-metal interactions, and steric hindrance of the nucleophilic attack on the *sn*-3 carbon by the *sn*-1 ester.^{12,16,19,52} Therefore, binding of the alkali metal to the *sn*-1 ester can promote the cyclization of the *sn*-2 ester by cleaving the headgroup resulting in I (Figure 1), which is in line with reported OzID and UVPD results.^{13,16} To investigate the structure of resulting fragment ions, computational and experimental studies were conducted for sodiated and potassiumated PC 4:0/4:0 ions after neutral loss of 183 Da.

Investigation of [PC 4:0/4:0 + Na/K - 183]⁺ Fragments. In order to contribute to the mechanistic understanding of GP fragmentation pathways and resulting structures, IRMPD spectroscopy was performed on the fragment ions. For this purpose, CID fragments corresponding to headgroup loss of [PC 4:0/4:0 + Na/K - 183]⁺ were spectroscopically investigated, as shown in Figure 7 (structures in Figure S10 and band positions in Tables S5 and S6). Calculations were performed with sodium and potassium attached to 1,3-dioxolane- (Na_{O5} , Na_{O5i} , K_{O5}) and 1,3-dioxane-type (Na_{O6} , K_{O6}) structures. The 1,3-dioxolane derivative is energetically favored by 87.1 kJ·mol⁻¹ (80.2 for Na_{O5i}) in [PC 4:0/4:0 + Na]⁺, and the six-membered ring 1,3-dioxane derivative is energetically favored by 2.7 kJ·mol⁻¹ for [PC 4:0/4:0 + K]⁺.

In contrast to the precursor ion spectra, the IRMPD spectra of the CID fragments contain six bands, which appear at very similar wavenumbers for [PC 4:0/4:0 + Na - 183]⁺ and [PC 4:0/4:0 + K - 183]⁺. The bands at ~1700 and 1025 cm⁻¹ are red-shifted by 20 cm⁻¹ for the potassium compared to the sodium complex. The similar positions and number of bands suggest structural similarity of the fragment structures. Due to the shifts of the ester-related signals between Na⁺ and K⁺, the charge carriers are likely attached to them. Compared to the precursor ion spectra, the bands assigned to $\nu(C=O)$ are red-shifted for both adducts. This shift suggests either a stronger influence of the charge carriers on the ester in the fragment as compared to the precursor or the appearance of a new structural motif in the fragment ions. The double-peak feature at 1200–1150 cm⁻¹ as well as bands at 1300–1400 and 1025 cm⁻¹ appear in the [PC 4:0/4:0 + Na/K - 183]⁺ spectra but are absent in the precursor IRMPD spectra. Bands assigned to $\nu(NMe_3)$ and the phosphate group in the precursor spectra are absent in the fragment spectra.

Based on literature values, experimental bands at 1689 cm⁻¹ (Na⁺) and 1717 cm⁻¹ (K⁺) are assigned as a combination of a red-shifted $\nu(C=O)$ band and a cyclic acetal-like $\nu(O-C-O)$ band.³⁹ For both adducts, experimental versus theoretical differences for $\nu(C=O)$ are small for five-membered rings (7 cm⁻¹ Na_{O5} /4 cm⁻¹ Na_{O5i} /16 cm⁻¹ K_{O5}) and increase for the six-membered rings (19 cm⁻¹ Na_{O6} /44 cm⁻¹ K_{O6}). Deviations between experimental bands and theoretical $\nu(O-C-O)$ modes are higher for the five-membered rings (39 cm⁻¹ Na_{O5} /16 cm⁻¹ Na_{O5i} /32 cm⁻¹ K_{O5}) compared to the six-membered rings (15 cm⁻¹ Na_{O6} /9 cm⁻¹ K_{O6}). Compared with the precursor IRMPD spectra, the combined $\nu(C=O)$ and $\nu(O-C-O)$ modes are red-shifted by 20 cm⁻¹ (Na⁺) and 4 cm⁻¹ (K⁺). The red shift of the band is likely a result of an increased interaction of the ester to the metal ion, which is

consistent with the candidate structures, where interactions of the alkali metal with the ester probably increases due to the lack of interactions with the phosphate moiety. The O-C-O motif potentially contributes to the red shift.

Bands assigned to $\nu_{sym}(O=C-O)$ are in the upper range of literature values and blue-shifted compared to the precursor spectra. The bands assigned to $\delta(O-C-O)$ are part of the crowded experimental region at ~1230–1150 cm⁻¹ with maxima at 1188/1158 cm⁻¹ in Na⁺ and 1198/1171 cm⁻¹ in K⁺. The number and position of bands in our data are similar to structurally related acetals reported in the literature.^{53,54} In particular, Bermann et al. described the presence of characteristic acetal bands in IR spectroscopy, with wavenumbers of 1151–1140 and 1110–1091 cm⁻¹ for 1,3-dioxolane. The experimental bands are all within the range of literature values for acetals $\delta(O-C-O)$ (1300–1000 cm⁻¹). The same is true for the calculated acetal $\delta(O-C-O)$ vibrations. Bands at 1013 cm⁻¹ (Na⁺) and 1052 cm⁻¹ (K⁺) in the experimental spectra may be explained by the $\nu(O-C-C)$ modes of all isomers. Similar to $\delta(O-C-O)$, the values are close to literature values for $\nu(O-C-C)$ of acetals.⁵⁵ Presence of a cyclic acetal-like structure can be the result of cyclization of the glycerol backbone, as shown in Figure 1, and are strong indication of formation of cyclic dioxolane/dioxane structures upon precursor ion fragmentation.

Bands at 1451 cm⁻¹ (Na⁺) and 1453 cm⁻¹ (K⁺) are close to theoretical $\delta(CH_n)$ bands for all isomers. The bands at 1388 and 1393 cm⁻¹, only found in the fragment spectra, are in line with $\delta(CH_1/CH_2)_{ring}$ vibrations in the calculated spectra, but bands in theoretical five- and six-membered ring isomers are too close to distinguish between dioxolane and dioxane structures.

Therefore, $\nu(C=O)$ and $\nu(O-C-O)$ bands are the only spectroscopic signatures that are not overlapping with other bands and whose frequencies are significantly influenced by interactions with ions or by structural changes.^{56,57} The positions and widths of $\nu(C=O)$ in the experimental spectrum for the Na⁺ cationized fragment overlap more with predicted vibrations for the Na_{O6} structure than with those for the Na_{O5} structure, but all other bands are in better agreement with Na_{O5} . This is quite surprising when comparing the energetic destabilization of Na_{O6} (87.1 kJ·mol⁻¹) compared to Na_{O5} . The high-energy differences between Na_{O5} / Na_{O5i} and Na_{O6} are probably the result of complexation of Na⁺ by the C=C bond, which is absent in Na_{O6} . Due to the thermal energy at 298 K and the inaccuracy of the DFT energy differences between isomers, interconversion between Na_{O5} and Na_{O5i} possibly occurs, the “true” energetic order is not captured with DFT methods or high-energy isomers are kinetically trapped upon CID. The $\nu(C=O)$ and $\nu(O-C-O)$ bands of the calculated Na_{O5i} spectrum are in line with the experimental IRMPD data making both Na_{O5i} and Na_{O6} likely candidate structures for the CID fragment ion, but the significant energetic destabilization of Na_{O6} makes the presence of a 1,3-dioxolane structure more likely.

The energetic difference between the isomers K_{O5} and K_{O6} for [PC 4:0/4:0 + K - 183]⁺ is only 2.7 kJ·mol⁻¹ as potassium does not interact with the C=C bond to stabilize the dioxolane compared to the dioxane. Compared with the experimental spectrum, the $\nu(C=O)$ and $\nu(O-C-O)$ bands in the theoretical spectra are red-shifted by roughly 50 cm⁻¹ for the K_{O6} isomer and by only 10 cm⁻¹ for K_{O5} . Moreover, no other isomer for K_{O6} exists that can explain the position and

width of the experimental band at 1717 cm^{-1} . This suggests the CID fragment ion to possess a 1,3-dioxolane structure, which is supported by a better overlap between experimental and theoretical results of the other bands.

CONCLUSION

In this study, we present the first IRMPD spectra of PC ions and PC-derived fragment ions. The aim of this study was to contribute to the understanding of reactions underlying tandem MS fragmentation of lipids in the gas phase.¹⁶ For this purpose, IRMPD spectra of protonated, sodiated, and potassiumated PC 4:0/4:0 were recorded, and theoretical structures, energies, and IR spectra of three (H^+) to four (Na^+ , K^+) potential isomers of the adducts were obtained. In addition, IRMPD spectra of fragment ions formed by neutral loss of 183 Da were investigated.

With help of these predicted spectra for the different isomers and comparison to experimental results, multiple, two, and one isomer(s) for H^+ , Na^+ , and K^+ adducts, respectively, were identified as most likely gas-phase ion structure. Whereas the multitude of energetically low-lying isomers prevents unambiguous assignment of IRMPD spectra to a single protonated lipid isomer structure, the lowest-energy isomers of $[\text{PC 4:0/4:0} + \text{Na/K}]^+$ are in line with experimental results and are structurally similar. In particular, isomers for Na^+ and K^+ that best describe experimental band positions contain pronounced phosphate–metal–*sn*-1 ester interactions, whereas the *sn*-2 ester does not, or at least to a lesser extent, bind to the alkali metal ion. These preferred interactions between *sn*-1 ester carbonyl and alkali metal ions most likely decrease the flexibility and electron density for a nucleophilic attack of the carbonyl oxygen at the *sn*-3 carbon atom as proposed to occur during CID activation compared to the *sn*-2 moiety. Therefore, our assigned precursor structures are consistent with the proposed formation of 1,3-dioxolane intermediates.

Further evidence for the preferred formation of 1,3-dioxolane over 1,3-dioxane structures upon CID fragmentation of alkali metal adducts of GPs is presented by spectroscopic investigation of $[\text{PC 4:0/4:0} + \text{Na/K} - 183]^+$ ions. In particular, the appearance of $\delta(\text{O}-\text{C}-\text{O})$, $\delta(\text{CH}_{1,2})_{\text{ring}}$, and other bands associated with an acetal moiety as well as absence of $\nu(\text{NMe}_3)$, $\nu(\text{P}=\text{O})$, and $\nu(\text{P}-\text{O}-\text{C})$ bands as compared to the precursor spectra, is in line with 1,3-dioxolane and 1,3-dioxone structures. Comparison of predicted $\nu(\text{C}=\text{O})$ and $\nu(\text{O}-\text{C}-\text{O})$ bands for potential 1,3-dioxolanes and 1,3-dioxanes to experimental spectra point toward the predominant formation of 1,3-dioxolane isomers. This further supports the mechanistic picture in which 1,3-dioxolane fragments are formed upon CID and explaining the *sn*-isomer selectivity of tandem MS tools targeting these specific CID fragment ions. Our findings are also in line with a recent study by Kirschbaum et al. that provided evidence for the formation of 1,3-dioxolanes upon fragmentation of protonated lipids.⁵⁸ This study also shows that the methodology and the findings of our work most likely extend to other lipid classes and other lipid chain length but further experiments are required to validate this assumption.

This first IRMPD spectroscopic study of GPs and corresponding isomers demonstrates that spectroscopic investigations of lipids can contribute to a better understanding of proposed CID fragmentation rules and mechanisms. Therefore, we envisage more and extended spectroscopic investigations of lipids and lipid fragment ions in the future, in

order to rationalize lipid fragment ion mass spectra and systematically improve structure elucidation of lipids in high-throughput lipidomics workflows.

ASSOCIATED CONTENT

Supporting Information

The Supporting Information is available free of charge at <https://pubs.acs.org/doi/10.1021/jasms.1c00277>.

Proposed lipid fragmentation mechanism; DFT convergence of protonated lipid structures to the *sn*-1 isomer; structure of reference complexes; IRMPD mass spectra of $[\text{PC 4:0/4:0} + \text{M}]^+$ ($\text{M} = \text{H, Na, K}$) at $\sim 1700 \text{ cm}^{-1}$; detailed view of optimized $[\text{PC 4:0/4:0} + \text{M}]^+$ ($\text{M} = \text{H, Na, K}$) DFT structures and corresponding geometric parameters; vibrational band positions and assignments for $[\text{PC 4:0/4:0} + \text{M}]^+$ ($\text{M} = \text{H, Na, K}$); detailed view of optimized $[\text{PC 4:0/4:0} + \text{M} - 183]^+$ ($\text{M} = \text{Na, K}$) DFT structures and corresponding geometric parameters; vibrational band positions and assignments for $[\text{PC 4:0/4:0} + \text{M} - 183]^+$ ($\text{M} = \text{Na, K}$) (PDF)

AUTHOR INFORMATION

Corresponding Author

Sven Heiles – Institute of Inorganic and Analytical Chemistry, Justus Liebig University Giessen, 35392 Giessen, Germany; orcid.org/0000-0003-3779-8071; Email: sven.heiles@anorg.chemie.uni-giessen.de

Authors

Simon Becher – Institute of Inorganic and Analytical Chemistry, Justus Liebig University Giessen, 35392 Giessen, Germany

Giel Berden – FELIX Laboratory, Institute for Molecules and Materials, Radboud University, 6525 ED Nijmegen, The Netherlands

Jonathan Martens – FELIX Laboratory, Institute for Molecules and Materials, Radboud University, 6525 ED Nijmegen, The Netherlands; orcid.org/0000-0001-9537-4117

Jos Oomens – FELIX Laboratory, Institute for Molecules and Materials, Radboud University, 6525 ED Nijmegen, The Netherlands

Complete contact information is available at: <https://pubs.acs.org/doi/10.1021/jasms.1c00277>

Notes

The authors declare the following competing financial interest(s): Simon Becher has received funding from TransnMIT GmbH, Germany. Giel Berden, Jonathan Martens, Jos Oomens and Sven Heiles declare no competing financial interest.

ACKNOWLEDGMENTS

S.H. acknowledges the Fonds der chemischen Industrie for financial support through a Liebig fellowship. We acknowledge technical assistance by the Bioinformatics Core Facility/Professorship of Systems Biology at JLU Giessen and access to resources financially supported by the BMBF Grant FKZ 031A533 to the BiGi center within the de.NBI network. The authors gratefully acknowledge the Nederlandse Organisatie

voor Wetenschappelijk Onderzoek (NWO) for the support of the FELIX Laboratory.

REFERENCES

- (1) Shevchenko, A.; Simons, K. Lipidomics: coming to grips with lipid diversity. *Nat. Rev. Mol. Cell Biol.* **2010**, *11* (8), 593–598.
- (2) Wenk, M. R. Lipidomics: new tools and applications. *Cell* **2010**, *143* (6), 888–895.
- (3) Kimura, T.; Jennings, W.; Epan, R. M. Roles of specific lipid species in the cell and their molecular mechanism. *Prog. Lipid Res.* **2016**, *62*, 75–92.
- (4) Wenk, M. R. The emerging field of lipidomics. *Nat. Rev. Drug Discovery* **2005**, *4*, 594–610.
- (5) Ersoy, B. A.; Tarun, A.; D'Aquino, K.; Hancer, N. J.; Ukumadu, C.; White, M. F.; Michel, T.; Manning, B. D.; Cohen, D. E. Phosphatidylcholine transfer protein interacts with thioesterase superfamily member 2 to attenuate insulin signaling. *Sci. Signaling* **2013**, *6* (286), ra64.
- (6) Balog, J.; Kumar, S.; Alexander, J.; Golf, O.; Huang, J.; Wiggins, T.; Abbassi-Ghadi, N.; Enyedi, A.; Kacska, S.; Kinross, J.; Hanna, G. B.; Nicholson, J. K.; Takats, Z. In vivo endoscopic tissue identification by rapid evaporative ionization mass spectrometry (REIMS). *Angew. Chem., Int. Ed.* **2015**, *54* (38), 11059–11062.
- (7) Munir, R.; Lisec, J.; Jaeger, C.; Zaidi, N. Abundance, fatty acid composition and saturation index of neutral lipids in colorectal cancer cell lines. *Acta Biochim. Polym.* **2021**, *68* (1), 115–118.
- (8) Kuge, H.; Akahori, K.; Yagyu, K.-I.; Honke, K. Functional compartmentalization of the plasma membrane of neurons by a unique acyl chain composition of phospholipids. *J. Biol. Chem.* **2014**, *289* (39), 26783–26793.
- (9) Liebisch, G.; Vizcaino, J. A.; Köfeler, H.; Trötz Müller, M.; Griffiths, W. J.; Schmitz, G.; Spener, F.; Wakelam, M. J. O. Shorthand notation for lipid structures derived from mass spectrometry. *J. Lipid Res.* **2013**, *54* (6), 1523–1530.
- (10) Ejsing, C. S.; Sampaio, J. L.; Surendranath, V.; Duchoslav, E.; Ekroos, K.; Klemm, R. W.; Simons, K.; Shevchenko, A. Global analysis of the yeast lipidome by quantitative shotgun mass spectrometry. *Proc. Natl. Acad. Sci. U. S. A.* **2009**, *106* (7), 2136–2141.
- (11) Danne-Rasche, N.; Coman, C.; Ahrends, R. Nano-LC/NSI MS Refines Lipidomics by Enhancing Lipid Coverage, Measurement Sensitivity, and Linear Dynamic Range. *Anal. Chem.* **2018**, *90* (13), 8093–8101.
- (12) Murphy, R. C. Tandem Mass Spectrometry of Lipids. *New Developments in Mass Spectrometry*; Royal Society of Chemistry: Cambridge, UK, 2014.
- (13) Heiles, S. Advanced tandem mass spectrometry in metabolomics and lipidomics—methods and applications. *Anal. Bioanal. Chem.* **2021**, *413*, 5927.
- (14) Paine, M. R. L.; Poade, B. L. J.; Eijkel, G. B.; Marshall, D. L.; Blanksby, S. J.; Heeren, R. M. A.; Ellis, S. R. Mass Spectrometry Imaging with Isomeric Resolution Enabled by Ozone-Induced Dissociation. *Angew. Chem., Int. Ed.* **2018**, *57* (33), 10530–10534.
- (15) Wäldchen, F.; Becher, S.; Esch, P.; Kompauer, M.; Heiles, S. Selective phosphatidylcholine double bond fragmentation and localisation using Paternò-Büchi reactions and ultraviolet photodissociation. *Analyst* **2017**, *142* (24), 4744–4755.
- (16) Williams, P. E.; Klein, D. R.; Greer, S. M.; Brodbelt, J. S. Pinpointing Double Bond and sn-Positions in Glycerophospholipids via Hybrid 193 nm Ultraviolet Photodissociation (UVPD) Mass Spectrometry. *J. Am. Chem. Soc.* **2017**, *139* (44), 15681–15690.
- (17) Kates, M. Techniques of lipidology: Isolation, analysis and identification of lipids. *Laboratory techniques in biochemistry and molecular biology*, 2nd revised ed.; Elsevier, 1986; Vol. 3.
- (18) Mouchlis, V. D.; Chen, Y.; McCammon, J. A.; Dennis, E. A. Membrane Allostery and Unique Hydrophobic Sites Promote Enzyme Substrate Specificity. *J. Am. Chem. Soc.* **2018**, *140* (9), 3285–3291.
- (19) Hsu, F.-F.; Turk, J. Electrospray ionization/tandem quadrupole mass spectrometric studies on phosphatidylcholines: The fragmentation processes. *J. Am. Soc. Mass Spectrom.* **2003**, *14* (4), 352–363.
- (20) Cao, W.; Cheng, S.; Yang, J.; Feng, J.; Zhang, W.; Li, Z.; Chen, Q.; Xia, Y.; Ouyang, Z.; Ma, X. Large-scale lipid analysis with C=C location and sn-position isomer resolving power. *Nat. Commun.* **2020**, *11* (1), 375.
- (21) Becher, S.; Esch, P.; Heiles, S. Relative Quantification of Phosphatidylcholine sn-Isomers Using Positive Doubly Charged Lipid-Metal Ion Complexes. *Anal. Chem.* **2018**, *90* (19), 11486–11494.
- (22) Lemaire, J.; Boissel, P.; Heninger, M.; Mauclair, G.; Bellec, G.; Mestdag, H.; Simon, A.; Le Caer, S.; Ortega, J. M.; Glotin, F.; Maitre, P. Gas phase infrared spectroscopy of selectively prepared ions. *Phys. Rev. Lett.* **2002**, *89* (27), 273002.
- (23) Oomens, J.; van Rooij, A. J. A.; Meijer, G.; von Helden, G. Gas-Phase Infrared Photodissociation Spectroscopy of Cationic Polyaromatic Hydrocarbons. *Astrophys. J.* **2000**, *542* (1), 404–410.
- (24) Heiles, S.; Berden, G.; Oomens, J.; Williams, E. R. Competition between salt bridge and non-zwitterionic structures in deprotonated amino acid dimers. *Phys. Chem. Chem. Phys.* **2018**, *20* (23), 15641–15652.
- (25) Oomens, J.; Young, S.; Molesworth, S.; van Stipdonk, M. Spectroscopic evidence for an oxazolone structure of the b(2) fragment ion from protonated tri-alanine. *J. Am. Soc. Mass Spectrom.* **2009**, *20* (2), 334–339.
- (26) Lagutschenkov, A.; Langer, J.; Berden, G.; Oomens, J.; Dopfer, O. Infrared spectra of protonated neurotransmitters: dopamine. *Phys. Chem. Chem. Phys.* **2011**, *13* (7), 2815–2823.
- (27) Knorke, H.; Langer, J.; Oomens, J.; Dopfer, O. Infrared Spectra of Isolated Protonated Polycyclic Aromatic Hydrocarbon Molecules. *Astrophys. J.* **2009**, *706* (1), L66–L70.
- (28) van Outersterp, R. E.; Martens, J.; Berden, G.; Steill, J. D.; Oomens, J.; Rijs, A. M. Structural characterization of nucleotide 5'-triphosphates by infrared ion spectroscopy and theoretical studies. *Phys. Chem. Chem. Phys.* **2018**, *20* (44), 28319–28330.
- (29) Lagatie, O.; Verheyen, A.; van Asten, S.; Odiere, M. R.; Djuardi, Y.; Leveck, B.; Vlaminck, J.; Mekonnen, Z.; Dana, D.; T'Kindt, R.; Sandra, K.; van Outersterp, R.; Oomens, J.; Lin, R.; Dillen, L.; Vreeken, R.; Cuyckens, F.; Stuyver, L. J. 2-Methyl-pentanoyl-carnitine (2-MPC): a urine biomarker for patent *Ascaris lumbricoides* infection. *Sci. Rep.* **2020**, *10* (1), 15780.
- (30) Martens, J.; van Outersterp, R. E.; Vreeken, R. J.; Cuyckens, F.; Coene, K. L. M.; Engelke, U. F.; Kluijtmans, L. A. J.; Wevers, R. A.; Buydens, L. M. C.; Redlich, B.; Berden, G.; Oomens, J. Infrared ion spectroscopy: New opportunities for small-molecule identification in mass spectrometry - A tutorial perspective. *Anal. Chim. Acta* **2020**, *1093*, 1–15.
- (31) Martens, J.; Berden, G.; Gebhardt, C. R.; Oomens, J. Infrared ion spectroscopy in a modified quadrupole ion trap mass spectrometer at the FELIX free electron laser laboratory. *Rev. Sci. Instrum.* **2016**, *87* (10), 103108.
- (32) Hamlow, L. A.; Zhu, Y.; Devereaux, Z. J.; Cunningham, N. A.; Berden, G.; Oomens, J.; Rodgers, M. T. Modified Quadrupole Ion Trap Mass Spectrometer for Infrared Ion Spectroscopy: Application to Protonated Thiated Uridines. *J. Am. Soc. Mass Spectrom.* **2018**, *29* (11), 2125–2137.
- (33) Becke, A. D. Density-functional thermochemistry. III. The role of exact exchange. *J. Chem. Phys.* **1993**, *98* (7), 5648–5652.
- (34) Jensen, F. Polarization consistent basis sets: Principles. *J. Chem. Phys.* **2001**, *115* (20), 9113–9125.
- (35) Hanwell, M. D.; Curtis, D. E.; Lonie, D. C.; Vandermeersch, T.; Zurek, E.; Hutchison, G. R. Avogadro: an advanced semantic chemical editor, visualization, and analysis platform. *J. Cheminf.* **2012**, *4* (1), 17.
- (36) Grimme, S.; Antony, J.; Ehrlich, S.; Krieg, H. A consistent and accurate ab initio parametrization of density functional dispersion correction (DFT-D) for the 94 elements H-Pu. *J. Chem. Phys.* **2010**, *132* (15), 154104.

- (37) Valiev, M.; Bylaska, E.J.; Govind, N.; Kowalski, K.; Straatsma, T.P.; Van Dam, H.J.J.; Wang, D.; Nieplocha, J.; Apra, E.; Windus, T.L.; de Jong, W.A. NWChem: A comprehensive and scalable open-source solution for large scale molecular simulations. *Comput. Phys. Commun.* **2010**, *181* (9), 1477–1489.
- (38) Laury, M. L.; Carlson, M. J.; Wilson, A. K. Vibrational frequency scale factors for density functional theory and the polarization consistent basis sets. *J. Comput. Chem.* **2012**, *33* (30), 2380–2387.
- (39) Meyers, R. A., Ed. *Encyclopedia of Analytical Chemistry*; John Wiley & Sons, Ltd., 2006.
- (40) Becker, H. G. O.; Beckert, R. *Organikum: Organisch-chemisches Grundpraktikum*, 24., vollst. überarb. und aktualisierte Aufl./von Rainer Beckert; Wiley-VCH, 2015.
- (41) Fales, B. S.; Fujimade, N. O.; Nei, Y.-w.; Oomens, J.; Rodgers, M. T. Infrared multiple photon dissociation action spectroscopy and theoretical studies of diethyl phosphate complexes: effects of protonation and sodium cationization on structure. *J. Am. Soc. Mass Spectrom.* **2011**, *22* (1), 81–92.
- (42) Bottger, G. L.; Geddes, A. L. The infrared spectra of the crystalline tetramethylammonium halides. *Spectrochim. Acta* **1965**, *21* (10), 1701–1708.
- (43) Lommerse, J. P. M.; Price, S. L.; Taylor, R. Hydrogen bonding of carbonyl, ether, and ester oxygen atoms with alkanol hydroxyl groups. *J. Comput. Chem.* **1997**, *18* (6), 757–774.
- (44) Jeffrey, G. A. An introduction to hydrogen bonding. *Topics in physical chemistry*; Oxford University Press, 1997.
- (45) Corbridge, D. E. C. *The structural chemistry of phosphorus*; Elsevier, 1974.
- (46) Lewis, R. N.; McElhane, R. N.; Pohle, W.; Mantsch, H. H. Components of the carbonyl stretching band in the infrared spectra of hydrated 1,2-diacylglycerol bilayers: a reevaluation. *Biophys. J.* **1994**, *67* (6), 2367–2375.
- (47) Marlton, S. J. P.; McKinnon, B. I.; Ucur, B.; Maccarone, A. T.; Donald, W. A.; Blanksby, S. J.; Trevitt, A. J. Selecting and identifying gas-phase protonation isomers of nicotineH⁺ using combined laser, ion mobility and mass spectrometry techniques. *Faraday Discuss.* **2019**, *217* (0), 453–475.
- (48) Campbell, J. L.; Yang, A. M.-C.; Melo, L. R.; Hopkins, W. S. Studying Gas-Phase Interconversion of Tautomers Using Differential Mobility Spectrometry. *J. Am. Soc. Mass Spectrom.* **2016**, *27* (7), 1277–1284.
- (49) van Stipdonk, M. J.; Patterson, K.; Gibson, J. K.; Berden, G.; Oomens, J. IRMPD spectroscopy reveals a novel rearrangement reaction for modified peptides that involves elimination of the N-terminal amino acid. *Int. J. Mass Spectrom.* **2015**, *379*, 165–178.
- (50) Ekroos, K.; Ejsing, C. S.; Bahr, U.; Karas, M.; Simons, K.; Shevchenko, A. Charting molecular composition of phosphatidylcholines by fatty acid scanning and ion trap MS3 fragmentation. *J. Lipid Res.* **2003**, *44* (11), 2181–2192.
- (51) Pham, H. T.; Maccarone, A. T.; Thomas, M. C.; Campbell, J. L.; Mitchell, T. W.; Blanksby, S. J. Structural characterization of glycerophospholipids by combinations of ozone- and collision-induced dissociation mass spectrometry: the next step towards “top-down” lipidomics. *Analyst* **2014**, *139* (1), 204–214.
- (52) Nagelkerke, R.; Thatcher, G. R.; Buncl, E. Alkali-metal ion catalysis and inhibition in nucleophilic displacement reactions at carbon, phosphorus and sulfur centres. IX. p-Nitrophenyl diphenyl phosphate. *Org. Biomol. Chem.* **2003**, *1* (1), 163–167.
- (53) Brügel, W.; Oster, R. Über eine charakteristische IR-Bande der Acetale. *Angew. Chem.* **1956**, *68* (13), 441.
- (54) Bergmann, E. D.; Pinchas, S. Reaction products of primary β -hydroxy-amines with carbonyl compounds. I. The infrared absorption of acetals and ketals. *Recl. Trav. Chim. Pays-B. (Recueil des Travaux Chimiques des Pays-Bas)* **1952**, *71* (2), 161–167.
- (55) Smith, B. C. *Infrared spectral interpretation: A systematic approach*; CRC Press, 1999.
- (56) Bush, M. F.; Oomens, J.; Saykally, R. J.; Williams, E. R. Effects of alkaline earth metal ion complexation on amino acid zwitterion stability: results from infrared action spectroscopy. *J. Am. Chem. Soc.* **2008**, *130* (20), 6463–6471.
- (57) Drayß, M. K.; Armentrout, P. B.; Oomens, J.; Schäfer, M. IR spectroscopy of cationized aliphatic amino acids: Stability of charge-solvated structure increases with metal cation size. *Int. J. Mass Spectrom.* **2010**, *297* (1–3), 18–27.
- (58) Kirschbaum, C.; Greis, K.; Polewski, L.; Gewinner, S.; Schollkopf, W.; Meijer, G.; Helden, G.; Pagel, K. Unveiling Glycerolipid Fragmentation by Cryogenic Infrared Spectroscopy. *J. Am. Chem. Soc.* **2021**, *143* (36), 14827–14834.

Cite this: *Analyst*, 2021, **146**, 3977

Influence of protein ion charge state on 213 nm top-down UVPD†

Simon Becher,^a Huixin Wang,^b Michael G. Leeming,^c William A. Donald^{b,d} and Sven Heiles^{b,e}✉

Ultraviolet photodissociation (UVPD) is a powerful and rapidly developing method in top-down proteomics. Sequence coverages can exceed those obtained with collision- and electron-induced fragmentation methods. Because of the recent interest in UVPD, factors that influence protein fragmentation and sequence coverage are actively debated in the literature. Here, we performed top-down 213 nm UVPD experiments on a 7 T Fourier-transform ion cyclotron resonance mass spectrometer (FT-ICR MS) for the model proteins ubiquitin, myoglobin and cytochrome c that were electrosprayed from native, denaturing and supercharging solutions in order to investigate the effect of protein charge states on UVPD fragments. By performing UVPD in ultrahigh vacuum, factors associated with collisional cooling and any ion activation during transfer between mass analyzers can be largely eliminated. Sequence coverage increased from <10% for low charge states to >60% for high charge states for all three proteins. This trend is influenced by the overall charge state, *i.e.*, charges per number of amino acid residues, and to a lesser degree by associated structural changes of protein ions of different charge states based on comparisons to published collision-cross section measurements. To rationalize this finding, and correlate sequence ion formation and identity with the number and location of protons, UVPD results were compared to protonation sites predicted based on electrostatic modelling. Assuming confined protonation sites, these results indicate the presence of two general fragmentation types; *i.e.*, charge remote and charge directed. For moderately high protein charge states, fragment ions mostly originate in regions between likely protonation sites (charge remote), whereas sequence ions of highly charge protein ions occur either near backbone amide protonation sites at low-basicity residues (charge directed) or at charge remote sites (*i.e.*, high-basicity residues). Overall, our results suggest that top-down 213 nm UVPD performance in the zero-pressure limit depends strongly on protein charge states and protonation sites can influence the location of backbone cleavages.

Received 5th April 2021,
Accepted 13th May 2021
DOI: 10.1039/d1an00571e
rsc.li/analyst

Introduction

Sequencing peptides generated by enzymatic digestion of proteins, so called bottom-up proteomics, is the method of choice to investigate complex protein mixtures *via* mass spectrometry (MS) and tandem MS (MSⁿ) approaches, whereas dissociation of intact protein ions, *i.e.* top-down proteomics, is increasingly employed to reveal proteoform complexity. The increasing

prevalence of top-down investigations is driven by a growing appreciation that single amino acid alterations, isomerism or post-translational modifications (PTMs) can impact the functional context of proteins.¹ For example, Fournier *et al.* showed that acetylation of lysine can influence protein activity and function.² Using high-energy collisional dissociation the authors demonstrated that human lysine acetyltransferases KAT2A and KAT2B are capable of activating and deactivating polo-like kinase 4 by acetylation of PLK4 kinase residues K45 and K46.

On the other hand, the improvement of mass spectrometric performance, such as sensitivity, mass resolution, mass range, as well as development of novel MSⁿ workflows give access to proteins/protein complexes formed by electrospray ionization from native-like solutions and reveals proteoform complexity that is hard to capture with bottom-up methodologies.^{3–5} However, the success of proteoform identification as well as sequence coverages depends on the method of ion activation.

^aInstitute of Inorganic and Analytical Chemistry, Justus Liebig University Giessen, 35392 Giessen, Germany. E-mail: sven.heiles@anorg.chemie.uni-giessen.de

^bMark Wainwright Analytical Centre, University of New South Wales, New South Wales, Australia

^cBio21 Molecular Science and Biotechnology Institute, The University of Melbourne, Victoria, Australia

^dSchool of Chemistry, University of New South Wales, Sydney, New South Wales, Australia

† Electronic supplementary information (ESI) available. See DOI: 10.1039/d1an00571e

Collision-induced dissociation (CID) is the most widely used MSⁿ method in top-down proteomics.^{6,7} Upon CID, protein ions are heated by collisions with the gas atoms/molecules resulting in protein ion fragmentation. Due to the low energy per collision of most CID methods (typically 10 kJ mol⁻¹ per collision is transferred to protein ions in low-energy CID), the introduced energy after every collision equilibrates throughout the protein before bond cleavage occurs. Therefore, most prominent fragment ion signals are often associated with the lowest bond dissociation enthalpies. For example, Donald and co-workers demonstrated that CID of intact highly charged ubiquitin, cytochrome c, lysozyme and β -lactoglobulin ions results in preferential cleavage sites near the first low-basicity amino acid residue that is predicted to be protonated with increasing charge state yielding highly selective ion fragmentation.⁸ The highest sequence coverages are obtained for charge states without backbone protonation, because nonspecific cleavage of the amide backbone occurs. By comparison to predictions of charge carrier positions benchmarked against gas-phase basicity measurements, hybrid quantum mechanics and molecular dynamics simulations of dissociation pathways and energy-resolved CID measurements, the dominance of the observed selective fragment ions can be attributed to the lowered energetic demand of backbone cleavage due to protonation.⁹ However, slow heating during CID triggers preferential loss of labile groups complicating the ability to identify the sites of some PTMs and causing hydrogen/deuterium (H/D) scrambling.^{10,11} Infrared multiphoton dissociation (IRMPD) of protein ions utilizes the absorption of multiple IR photons, resulting in fragmentation patterns that are often similar to CID results.^{12,13}

An alternative means of fragmentation in top-down proteomics involves generating hydrogen-rich radical protein ions that subsequently fragment through intramolecular bond homolysis.¹⁴ Electrons can be introduced directly (electron-capture dissociation ECD) or *via* ion-ion reactions involving electron transfer (electron-transfer dissociation ETD). Molina *et al.* and Zenaidee *et al.* showed that cleavage of protein bonds in ETD and ECD tend to occur near the likely locations of charge carriers and depends strongly on charge state.^{15,16} That is, fragmentation in ECD and ETD experiments is influenced by the number and position of charge carriers, which impacts the sequence coverage. Resulting sequence coverage values for top-down proteomics *via* ETD and ECD are typically comparable to that for CID or higher, and importantly PTM fragmentation can be minimized in ETD/ECD.¹⁷

Another method for ion activation that recently has received considerable attention is ultraviolet photodissociation (UVPD). The method employs high energy UV photons for the electronic excitation of analyte ions to trigger fragmentation. The energy of a single UV photon can be used to form fragment ions and access high-energy dissociation pathways.^{18–20} The wavelengths mostly employed for UVPD of protein and peptide ions are 266 nm, 213 nm, 193 nm, and 157 nm.

UVPD has been employed in numerous case studies. For example, zwitterionic salt bridges in gaseous ions were identi-

fied by Julian and co-workers by irradiating protein ions with 266 nm laser light creating photoelectrons in close proximity to salt bridges as indicated by the detected c-fragments.²¹ Wavelengths below 266 nm allow excitation of amide and ester bonds. In a top-down proteomics approach Shaw *et al.* reported 99%, 93% and 87% sequence coverages using 193 nm photons on ubiquitin (9 kDa; 7+ to 13+), myoglobin (17 kDa; 16+, 18+, 20+, 22+ and 24+) and carbonic anhydrase II (29 kDa; 34+), respectively.¹⁷ Studies on apo- and holo-myoglobin showed fragment suppression for sites that bind to the heme unit as well as for the helical core of the molecule. This indicates the sensitivity of UVPD for selected charge states to probe primary, secondary, tertiary and quaternary protein structures.²²

Application of 157 nm photons from the vacuum ultraviolet (VUV) range increases possible fragmentation sites due to absorption by C–C and carbon–heteroatom bonds leading to homolytic bond cleavage in peptides.^{23,24} However, in addition to complications arising from containing the VUV laser beam, fragmentation can also result in extensive cleavage of side chain residues resulting in very complex tandem mass spectra.

Another UVPD wavelength that employs solid state lasers is 213 nm that is absorbed by aromatic groups, amides as well as sulfides, and is now available as part of a commercial mass spectrometer.²⁵ 213 nm UVPD systems have been used by multiple researchers to investigate peptides and protein ions. For example, cleavage of C–S and S–S bonds of cysteine moieties by 213 nm UVPD can result in the formation of unique thioether, disulfide and trisulfide fragments, which facilitate identification of cysteine linkages in antibodies.²⁶ The major factor that determines the performance of 213 nm UVPD top-down and bottom-up proteomics experiments is the absorption of UV light by the amide $n-\pi^*$ transition.²⁷ Typically amide groups exhibit a local absorption maximum around 210 nm.²⁸ In a study by Fornelli *et al.*, the authors found that proline residues increase fragmentation efficiencies compared to other amino acids in 213 nm UVPD.²⁹ Unique fragments of proline were also found by Dugourd and co-workers corresponding to $b + 2$, $a + 2$ and $y - 2$ ions formed in 213 nm UVPD.³⁰ The authors explained the formation of these 213 nm UVPD specific ions by homolytic bond cleavage after excitation of $n-\pi^*$ transitions in proline moieties. The dependence of protein charge states on 213 nm performance has been investigated by Fornelli *et al.* for ubiquitin (8+ to 13+), myoglobin (14+ to 25+) and carbonic anhydrase (29+ to 43+). This study was performed on an orbital trapping mass spectrometer but did not reveal a pronounced charge state dependence.²⁹

Here, we present top-down 213 nm UVPD results for a wide range of charge states for a set of model proteins in the zero-pressure limit in order to probe the intrinsic response of proteins to 213 nm light irradiation and rationalize fragmentation patterns in terms of charge state dependence. We examined ubiquitin, cytochrome c and myoglobin with charge states ranging from 5+ to 17+, 7+ to 24+, and 9+ to 34+ with top-down 213 nm UVPD, respectively. Cyclic alkyl carbonate solution additives were used to form protein ion charge states in

very high charge states.^{9,31} Experimental UVPD cleavage sites and ion abundances for all protein charge states are compared to predicted protonation sites in order to rationalize the impact of charge location and overall protein charge on 213 nm UVPD performance.

Experimental section

Safety considerations

Methanol (MeOH), 4-vinyl-1,3-dioxolan-2-one (vinyl ethylene carbonate, VEC), propylene carbonate (PC) ($\geq 99.7\%$) and formic acid (FA) were used for protein solutions. Heated electrospray ionization (HESI) uses high voltage and high temperatures. The high voltage area and hot surfaces were shielded by the source. Lasers in the UV range are dangerous for the human eye. To avoid danger, laser safety goggles were worn all the time and a laser safety officer examined the instrument.

Materials

Ubiquitin from bovine erythrocytes ($\geq 98\%$), cytochrome c from bovine heart ($\geq 95\%$), myoglobin from equine skeletal muscle ($\geq 95\%$), propylene carbonate (PC) ($\geq 99.7\%$), 4-vinyl-1,3-dioxolan-2-one (vinyl ethylene carbonate, VEC) ($\geq 99\%$) were purchased from Sigma-Aldrich (St Louis, MO, USA). Ammonium acetate (NH₄Ac) ($\geq 97\%$) was purchased from Alfa Aesar (Kandel, Germany). Methanol (HPLC grade) was purchased from Merck (Darmstadt, Germany). Water (HPLC grade) was purchased from VWR (Darmstadt, Germany). Formic acid (FA) ($\sim 98\%$) was purchased from Honeywell Fluka (Seelze, Germany).

Sample preparation

Proteins were diluted to final concentrations of 10^{-4} to 10^{-8} M. For native MS, 0.2% NH₄Ac and 1% FA in water were used as solvent.³² For denaturing solutions, proteins were prepared in 44.5% MeOH, 54.5% water and 1% FA. Protein supercharging was achieved by adding PC (1% to 20%) or VEC (5% to 10%) to the denaturing solutions (Fig. S1†).^{33,34} The heme associated signal at m/z 616.2 found in the supercharged cytochrome c spectrum is most likely a result of in-source activation of the highly charged ions.

Mass spectrometry

All experiments were performed on a 7 T LTQ FT Ultra (Thermo Fisher Scientific, Bremen, Germany), operated with 100 000 resolution at m/z 400. HESI was used for the ionization and typical parameters were: 3.5 to 5.5 kV spray voltage, 310 °C cone temperature, 2 to 20 $\mu\text{L min}^{-1}$ flow rate, 4 to 25 (arbitrary units) sheath gas rate, 0 to 5 (arbitrary units) aux gas rate, 0 to 20 (arbitrary units) sweep gas rate. All reported uncertainties are standard deviations of triplicate measurements. For the data evaluation, 120 UVPD spectra were averaged per charge state and protein (Fig. S2†). The influence on the signal-to-noise (S/N) ratio was evaluated by measuring 800 spectra using

100 000 resolution at m/z 400 and 300 spectra using 750 000 resolution at m/z 400.

For UVPD experiments a 213 nm laser was installed as described previously (Fig. S3a†).³⁵ Briefly, the fifth harmonic of a solid state Nd:YAG (Tempest, New Wave Research, Portland, USA) was guided in the ICR-cell through a UV-grade fused silica viewport (Hositrade, Hoevelaken, Netherlands). The laser was operated at 20 Hz providing 0.7 mJ per pulse with a 3.5 mm beam diameter. To limit the influence of secondary fragmentation, the dependence of the sequence coverage and the *PY* on pulses per spectra was investigated (Fig. S4–6†). For all proteins the sequence coverage increases with the number of pulses per spectrum, reaches a maximum and decreases for the highest pulse numbers. The decrease of sequence coverage most likely stems from extensive secondary fragmentation. To limit the impact of secondary fragments but also to obtain reasonably high sequence coverage, the pulse number at which the sequence coverage reaches a maximum (ubiquitin = 40 pulses per spectrum Fig. S4†, cytochrome c = 10 pulses per spectrum Fig. S5†, myoglobin = 20 pulses per spectrum Fig. S6†) was used. Precursor ions were isolated using $\Delta m/z = \pm 10$ to isolate the complete isotopic distribution of every charge state. Holo-myoglobin was fragmented in the native charge state 9+, all other experiments were carried out on apo-myoglobin.

To minimize the influence of the precursor signal intensity on UVPD results, the number of ions in the ICR-cell was controlled by adjusting the automatic gain control target, protein concentrations and HESI parameters. Stability of the spray conditions were checked by monitoring precursor signal intensity over 40 spectra (20 before and 20 after the UVPD measurement). The normalized level (NL) of the trapped ions was adjusted from 8×10^3 to 7×10^4 (Fig. S7†).

Data analysis

Data evaluation of UVPD-MS² data was performed using a custom in-house MATLAB algorithm. The Roepstorff nomenclature is used to describe peptide fragment ions.³⁶ Details of the algorithm are described in the ESI (Fig. S8†). The signal-to-noise (S/N) level was evaluated manually for each measurement. The S/N ratio used for data analysis was set to 3. All isotopes with a theoretical abundance of 65% relative to the most abundant isotope need to be present for signal annotation. The maximum absolute deviation was set to 10 ppm. PTMs, H₂O or NH₃ loss and multiply cleaved fragments were not taken into account. Only fragments meeting all these requirements were used for the sequence coverage and *PY* calculations. Fragment ion intensities were normalized such that the sum of all fragment intensities is 1. The efficiency of dissociation is represented by the product yield (*PY*), which is defined as

$$PY = \frac{\sum \frac{I_P}{z}}{\sum \frac{I_P}{z} + \sum \frac{I_A}{z}} \quad (1)$$

where I_F is the intensity of all fragment ions, I_A is the intensity of the precursor signal, and z is the charge of the signal to account for the charge state dependent signal response intrinsic to all FT-MS methods.

Protonation of the proteins was investigated theoretically by calculating the frequency of protonation at different amino acid residues using the freeware PredictPrPlus,⁸ which is based on the method reported by Williams and co-workers.³⁷ Specifically, the energies of proton configurations were calculated by assuming the proteins are in highly elongated 1D strings, treating each amino acid residue as a node with an intrinsic gas-phase basicity and accounting for coulombic repulsion between charge sites. Our model does not adequately describe the distributions of protons for native-like protein ion structures. Therefore, linking fragmentation patterns to native-like protein ion structures should be avoided. The energies are then optimized using a Monte Carlo-type 'pseudo-random walk' method.³⁷ This approach can be used to predict the configuration of ionizing protons on an elongated protein, thereby estimate the measured basicity values¹⁶ and collision-induced cleavage sites of intact protein ions.⁸ Here, PredictPrPlus was modified to also calculate and output the electrostatic potential experienced by a 'probe' charge placed at neutral backbone amide moieties as a function of the residue number, and the electrostatic repulsion between fragment ions at a given cleavage site prior to fragmentation as a function of amino acid residue number. Input parameters used for the calculations are given in Table S1.†

Results and discussion

Effects of MS parameters on UVPD results

To probe the intrinsic propensity of proteins to fragment upon 213 nm UVPD, the effects of experimental MS parameters on the number, intensity and identity of fragment ions were investigated. Firstly, the background pressure can impact UVPD results.³⁸ Here, we assume that gas-protein ion collisions during the trapping time of at most 2 s are negligible at a background pressure of $\sim 2 \times 10^{-10}$ mbar in the vacuum chamber surrounding the FT-ICR cell.³⁹

Four further factors can influence the PY and S/N of UVPD results. These are: (a) number of trapped ions, (b) the mass spectrometric performance settings (e.g. resolution and scan number), (c) the number of averaged spectra and (d) the number of laser pulses per spectrum.

(a) The influence of the number of trapped ions on the UVPD results was investigated by monitoring the sequence coverage as a function of precursor ion abundance. A representative example of a plot of sequence coverage vs. precursor ion abundance for [ubiquitin + 13H]¹³⁺ is shown in Fig. S9.† The sequence coverage increases with increasing precursor abundance. However, ion abundances cannot be necessarily readily tuned for each charge state as the detected intensity of protein charge states is determined by the spray solution composition as well as the ESI process.^{40–42} To reduce the influence of the

precursor ion abundance between different protein charge states, precursor abundances were adjusted to 8×10^3 – 7×10^4 (Fig. S7†) by tuning the concentration and ion collection time, which was the values typically encountered for the lowest intensity protein charge states in all experiments.

(b) Because fragment ions can potentially overlap in m/z in top-down tandem MS, increasing the mass resolution will ultimately yield higher sequence coverage values compared to lower mass resolution settings. This is also true for our UVPD results as demonstrated in Fig. S10.† Compromising between measurement time and resolution all experiments were performed at mass resolution settings of 100 000 at m/z 400.

(c) The number of averaged spectra also influences the sequence coverage by affecting S/N levels. As expected, the noise decreases when increasing the number of averaged spectra (Fig. S2†), which increases the experiment time. To compromise between increased sequence coverage and measurement time, 120 spectra were averaged in all experiments.

(d) Another experimental parameter that influences fragment ion S/N levels is the number of laser pulses per spectrum. The influence of the number of laser pulses on the sequence coverage was studied for [ubiquitin + 13H]¹³⁺, [cytochrome c + 19H]¹⁹⁺ and [myoglobin c + 21H]²¹⁺, and the results are shown in Fig. S4–6.† Initially the sequence coverage increases when more laser pulses are used, hits a maximum and starts decreasing for the largest laser pulse numbers. But PY values stay mostly within the error margin of the experiments for laser pulse numbers above 10 (or 500 ms of irradiation time). The decrease of sequence coverage with increased number of laser pulses is likely caused by extensive secondary fragmentation of fragment ions. Laser pulse numbers with the maximum sequence coverage were selected and used throughout this study (40, 10 and 20 shots per spectrum for ubiquitin, cytochrome c and myoglobin, respectively). The constant PY for high laser pulse numbers also indicates that the influence of a kinetic shift on the PY and sequence coverage values is negligible under our experimental conditions. This is because increasing the laser pulse number goes along with an increased time for irradiated proteins to fragment until ion detection. If a kinetic shift would prevent fragmentation prior to ion detection, PY values should continuously increase with increasing laser pulse number.

Overall, the selected settings enabled the influence of experimental and instrumental parameters on the UVPD results to be minimized as the aim was to exclusively probe the intrinsic UVPD response of protein ions as a function of charge state. However, these settings are not intended to maximize the sequence coverage. If sequence coverage is near 100%, then any effects of charge state on the UVPD of protein ions will be more challenging to determine.

Influence of charge state on UVPD photoproduct yield

The PY of proteins subjected to tandem MS methods, such as CID or ETD, is known to be affected by many factors including primary, secondary, tertiary and quaternary protein structures

as well as protein charge state.^{8,43,44} In order to investigate the dependence of the *PY* on these factors in 213 nm UVPD, ubiquitin, myoglobin and cytochrome c were sprayed fragmented and analyzed from native, denaturing and supercharging solutions.

The resulting *PY*s as a function of charge state are shown in Fig. 1. Charge states analyzed from native, denaturing and unfolded solutions are color-coded yellow, blue and red, respectively.⁴⁵ The *PY* of all proteins increases with increasing charge states. A linear fit of *PY* values as a function of precursor ion charge state results in moderate to good coefficients of determination. In particular, R^2 values are 0.70 for ubiquitin (circles), 0.90 for cytochrome c (triangles) and 0.84 for myoglobin (crosses). Absolute deviations to the linear regression are at most ± 0.25 for all three proteins.

The collision cross sections (CCS) increase with protein charge state. However, the extent of the increase in CCS per charge state depends on ESI spray solution conditions and typically exhibits characteristic "jumps" in the slope of CCS vs. charge between charge states obtained from different solution conditions. For example, the CCS values in He for cytochrome c increases by $\sim 200 \text{ \AA}^2$ per charge for ions generated from native solutions, whereas that for denaturing and supercharging solutions increases by only $\sim 100 \text{ \AA}^2$ and $\sim 50 \text{ \AA}^2$ per charge respectively.⁴⁶ Because the *PY* values follow a largely linear trend for all precursor charge states, including charge states formed *via* different solution conditions, including presence of holo- (native MS) and apo-myoglobin (denaturing and

supercharging), these results suggest that protein structure and associated structural changes do not influence the overall UVPD *PY* as strongly as CCS values under these conditions. Therefore, our data implies that the most important factor affecting the magnitude of *PY*s is the overall charge state. Potentially, coulombic repulsion and the location of protons can more strongly affect the efficiency of fragmentation in 213 nm protein UVPD. These data are consistent with results reported by Kolbowski *et al.* who used 213 nm UVPD to identify the peptide charge density as driving force for peptide backbone cleavage.⁴³

Sequence coverage as a function of charge state

In contrast to the *PY*, the sequence coverage does not necessarily increase when fragment ion intensities increase. For example, multiple fragment ions originating from cleavage between the same adjacent residues (*e.g.*, detecting complementary a/x ions only vs. a/x, b/y, and c/z) do not increase the sequence coverage, whereas the *PY* is increased. The increase in sequence coverage for ubiquitin, cytochrome c and myoglobin is plotted vs. the protein charge state in Fig. 2. For all three proteins, the UVPD sequence coverage under our experimental conditions for the lower charge states is below 10%, increases with approximately 5% per charge state as the charge state increases, and then plateaus at a maximum of 50–60%. This non-linear increase in the sequence coverage with an increase in the charge state directly contrasts with previous top-down CID results.⁸ In CID, the sequence coverage first increases as

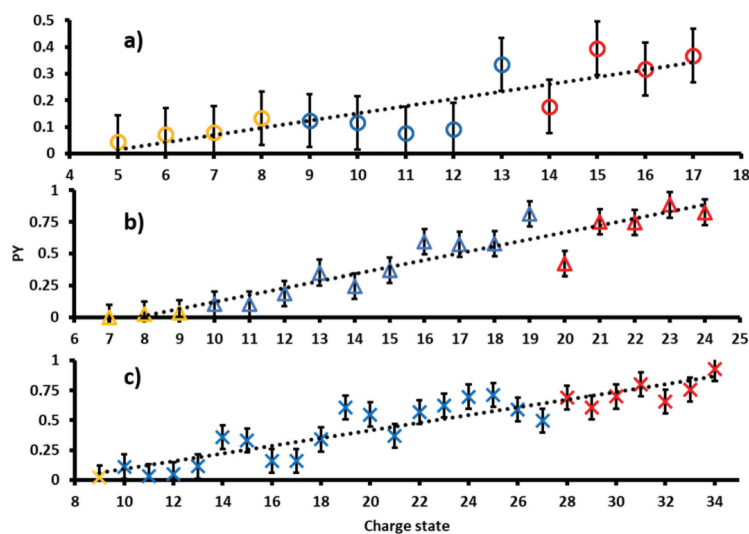


Fig. 1 Photoproduct yields for (a) ubiquitin, (b) cytochrome c and (c) myoglobin ions as a function of precursors charge state. Proteins formed from native, denaturing and supercharging solutions are color-coded yellow, blue and red, respectively. As a guide to the eye linear trend lines are shown in black.

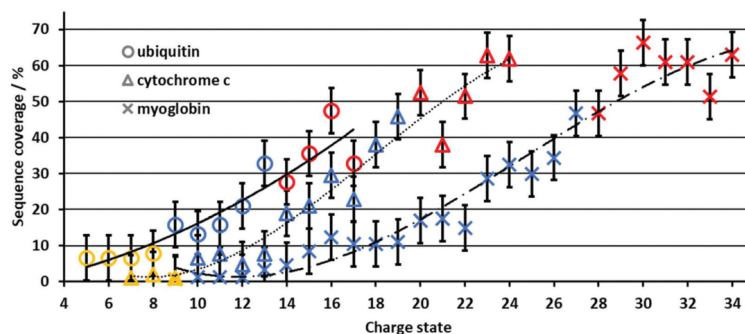


Fig. 2 Sequence coverage for ubiquitin, cytochrome c and myoglobin ions as a function of precursor charge state. Ubiquitin, cytochrome c and myoglobin are represented by circles, triangles and crosses, respectively. Proteins formed from native, denaturing and supercharging solutions are colored yellow, blue and red, respectively. The black lines serve as a guide to the eye.

protein charge states increase, and then drops significantly for higher protein charge states. Therefore, the charge state of protein ions influences the sequence coverage in 213 nm UVPD in a substantially different manner than in CID experiments for the same proteins and charge states.

Although the size and overall charge state of ubiquitin, cytochrome c and myoglobin are different, the increase in the sequence coverage with an increase in charge state follows a similar trend for all three proteins (Fig. 2). This implies that the increase of the sequence coverage in 213 nm UVPD with charge state is not substantially affected by the protein identity, size or overall charge but by the protein ion charge with respect to the protein size, *i.e.* the number of charges per amino acid. Therefore, Fig. 3 shows the sequence coverage as a function of charges per amino acids. The maximum charge states of the three proteins are 17+, 24+, 34+ for ubiquitin, cytochrome c and myoglobin, respectively. The charges per amino acid for all three proteins are in the range of 0.06 to 0.22.

The slope corresponding to the change in sequence coverage *vs.* an increase in charge density for all three proteins differs in the ranges of 0.06 to 0.11, 0.11 to 0.18 and 0.18 to 0.22 charges per residue. In the range of 0.06 to 0.11 there is essentially no increase in sequence coverage. From 0.11 to 0.18 the sequence coverage increases dramatically by 200–600% for ubiquitin, cytochrome c and myoglobin, respectively. In contrast, from 0.18 to 0.22 charges per residue, there is virtually no change in sequence coverage. The general trend is very similar for all three proteins. This suggests that the most important descriptor for the change of sequence coverage with charge state is the number of charges per amino acid.

Increasing the number of charges per amino acid of the protein has multiple effects. The distance between charges decreases on average and the repulsive Coulomb force between charge sites increases substantially. Moreover, at moderate to high charge states, nearly all basic residues should become

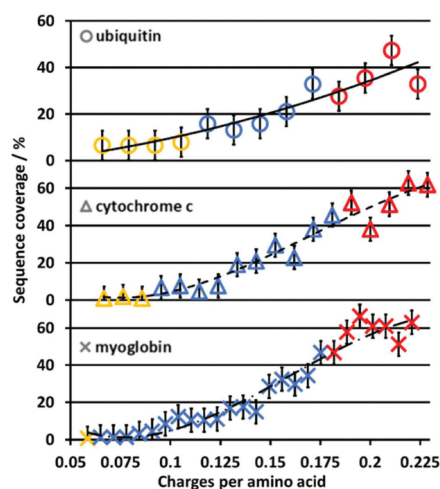


Fig. 3 Sequence coverage for ubiquitin, cytochrome c and myoglobin ions as a function of charges per amino acid residues. Ubiquitin, cytochrome c and myoglobin are represented by circles, triangles and crosses, respectively. Proteins formed from native, denaturing and supercharging solutions are colored yellow, blue and red, respectively. The black lines serve as a guide to the eye.

protonated resulting in the protonation of the amide backbone at higher charge states.^{8,47}

Influence of the charge state on fragment ion identities

We next investigated the type of fragment ions formed in 213 nm UVPD as a function of charge state. In Fig. 4, the normalized number of each fragment ion type formed upon UVPD

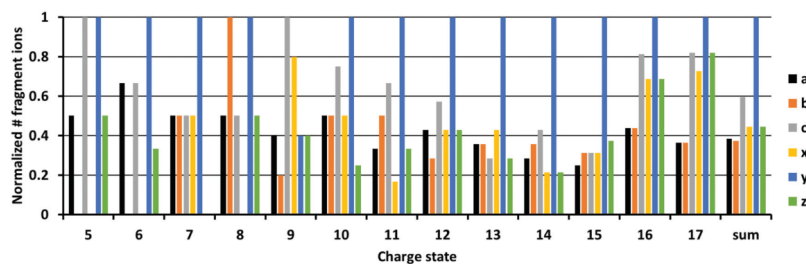


Fig. 4 Normalized number of fragment ions of ubiquitin charge states 5+ to 17+. Fragment ions of a, b, c, x, y, z are shown in black, orange, grey, yellow, blue and green, respectively. Fragments with masses of -1 and $+1$ are included.

of ubiquitin 5+ to 17+ is shown. Fragments with masses -1 Da and $+1$ Da were included for each ion type, corresponding to hydrogen-transfer reactions that can occur as fragment ions separate. Data for myoglobin and cytochrome c are provided in the ESI (Fig. S11 and 12†). Due to the limited sequence coverage obtained under our experimental conditions for low ion charge states, only a few fragments are present for charge states $<9+$. For charge states $>9+$, y-fragments are most abundant and for high charge states ($>15+$), all fragment types are formed in very similar abundances. The dominance of y ions for medium charge states is in line with studies by Dugourd and co-workers, who found y-fragments were the most prominent in 213 nm top-down UVPD of ubiquitin in an orbitrap instrument.⁴⁸ The dominance of y-type fragments is even more abundant in our data. This could be an effect of the trap pressure. While formation of b- and y-fragments is suppressed by collisional cooling in high pressure regimes, the b- and y-ion intensities increase at lower pressures.³⁸ These data are consistent with enhanced intramolecular vibrational relaxation from electronically excited states in the ultrahigh vacuum of the FT-ICR cell, resulting in the formation of relatively higher abundant y-ions, which are usually a distinctive sequence ion in top-down CID experiments.

The relative abundances of a, b, c, x, y and z fragments did not change substantially from the 8+ to 13+ charge states. Relative fragment type abundances were also reasonably constant up to charge state 17+. However, the difference in abundance between y-ions and all other ion types decreased for the 16+ and 17+ charge states. Results obtained for myoglobin and cytochrome c differ to ubiquitin (Fig. S11 and 12†). However, no trend for the fragment types is found for increasing charge states. Overall, these results indicate that the charge state of protein ions does not influence the relative abundance of 213 nm UVPD derived fragment ion types to a large extent, unlike all other parameters, such as *PY* and sequence coverage that depended strongly on the protein ion charge state.

Correlating fragmentation sites to charge carrier positions

In order to rationalize the impact of charge on top-down UVPD results, charge carrier positions and electrostatic potentials

were predicted using PredictPrPlus and compared to experimental results. Corresponding mass spectrometric fragment ion abundances (black bars), electrostatic potentials (white squares connected by a green line), protonation frequencies of side chains (blue bars) and the amide backbone (orange bars) are shown in Fig. 5 for $[\text{ubiquitin} + 12\text{H}]^{12+}$ and $[\text{ubiquitin} + 17\text{H}]^{17+}$. Results for all charge states of ubiquitin, cytochrome c and myoglobin are included in the SI (Fig. S13–15†). As the proton position of native-like protein ions are not accurately predicted, only fragment ions of unfolded charge states are quantitatively compared to model predictions.

$[\text{ubiquitin} + 12\text{H}]^{12+}$ is the first charge state of ubiquitin for which the number of protons is predicted to exceed the number of high-basicity amino acid moieties. For the UVPD of this ion, the experimental fragment ions are dominated by bond cleavage at Glu₁₈ (Fig. 5, top). Comparison to the predicted protonation sites reveals that the excess proton that is predicted to be located at a low basicity amide backbone site is likely to be located between Glu₁₆ and Ser₂₀. This suggests that amide bond cleavage correlates with amide backbone protonation. This is also in line with results for $[\text{ubiquitin} + 17\text{H}]^{17+}$ which contains four protons that are predicted to protonate the amide backbone (Fig. 5, bottom). These protonation sites (*i.e.* two protons between Leu₁₅ and Thr₂₂, one between Ile₃₆ and Pro₃₈ and one between Ser₅₇ and Tyr₅₉) correlate to experimental cleavage sites that result in high fragment ion intensities. This suggests that the presence of a charge on the amide backbone can facilitate and direct protein ion fragmentation, consistent with a charge-directed fragmentation event.^{30,49,50}

In contrast, some fragment ions for $[\text{ubiquitin} + 12\text{H}]^{12+}$, $[\text{ubiquitin} + 17\text{H}]^{17+}$ and also other ubiquitin charge states (Fig. S13†) are not associated with protonation of the amide backbone. For example, fragments close to Ile₃₆–Asp₃₉, Asp₅₂, Thr₅₅ in $[\text{ubiquitin} + 12\text{H}]^{12+}$ as well as Leu₈, Thr₉ and Ile₄₄ to Gly₄₇ in $[\text{ubiquitin} + 17\text{H}]^{17+}$ do not coincide with the presence of amide bond protonation. However, the location of these fragment ions in the amino acid sequence correlates with local or global minima of the Coulomb potential. In $[\text{ubiquitin} + 17\text{H}]^{17+}$ fragmentation between Ile₄₄ to Gly₄₇ would lead to most

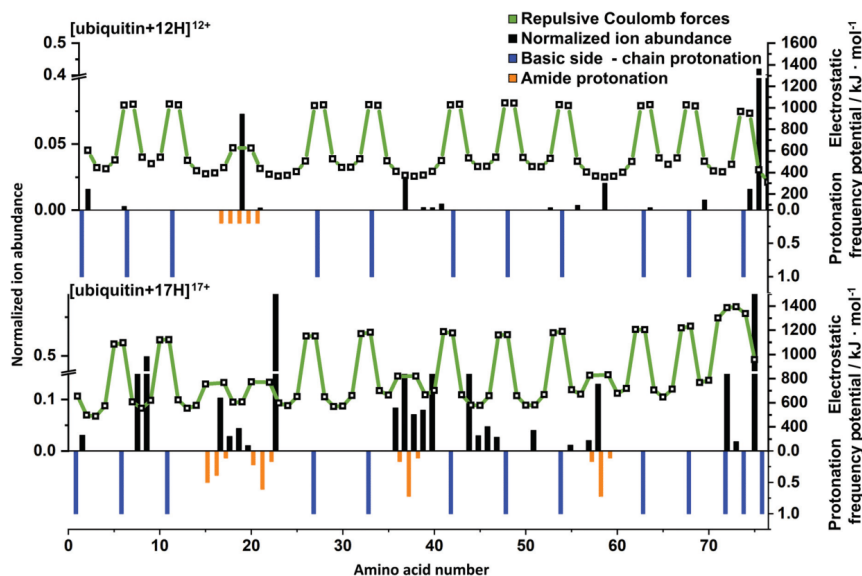


Fig. 5 Normalized experimental fragment ion abundances are shown as black bars. The calculated electrostatic potential at each residue is shown with white squares, which are connected with green lines to guide the eye. Predicted protonation frequencies at basic side-chain amino acid residue (or N/C-terminus) and the amide backbone are shown in blue and orange bars, respectively.

equally charged 9+ and 8+ fragments, resulting in a maximal decrease of intermolecular electrostatic potentials, (Fig. S16†) which is represented by high fragmentation yields between Ile₃₆ to Asp₃₉ and Ile₄₄ to Gly₄₇ for [ubiquitin + 17H]¹⁷⁺. The correlation of these fragmentation ions with a decrease of electrostatic potentials suggests that formation of these fragmentation ions is facilitated by maximizing the Coulomb energy decrease due to fragment ion formation. As formation of these fragment ions are not directly affected by the presence of charges but indirectly by remote influence of the Coulomb potential, the corresponding fragment ions can be classified as charge-remote fragment ions. Similar trends were observed for charge dependent fragment ions of myoglobin and cytochrome c (Fig. S14 and S15†). For example, [cytochrome c + 21H]²²⁺ has intense signals at Thr₂₉, Gly₃₅ - Phe₃₇, Lys₅₆ and Ser₄₈, Met₆₆ - Tyr₆₈, Leu₉₅ which coincide with minima of the electrostatic potential and protonation of the amide backbone, respectively. On the other hand, fragmentation at Lys₁₄ and Ile₇₆ does not correspond to charge-directed or charge-remote fragmentation. Therefore, all investigated protein ions contain between 10–15% of fragment ions not in line with the simplistic dissociation scenarios discussed above. However, the large majority of the fragments formed upon 213 nm are in agreement with the charge remote or charge directed fragmentation pathways. To explain the remaining 213 nm fragment ions, more future research is needed.

In CID experiments fragmentation at amino acid Glu₁₈ is highly selective for the 12+.⁸ Donald and co-workers attributed this selectivity to protonation of the amide bond of the first low basicity amino acid residue that is protonated with increasing charge (Glu₁₈) based on mixed QM/MM modelling, energy resolved CID experiments, and electrostatic calculations. Protonation of the amide bond was calculated to reduce the dissociation barrier by 50 kJ mol⁻¹ in charge-induced vs. charge-remote fragmentation mechanisms. In contrast to CID, 213 nm UVPD experiments of the 12+ ubiquitin yields additional fragments at Ile₃₆ to Gln₄₀ and Asp₅₂ reducing the selectivity of the formation of Glu₁₈ associated fragment ions in 213 nm UVPD compared to CID.

Differences in the selectivity of Glu₁₈ associated ions between CID and UVPD most likely arise due to excitation and energy redistribution events characteristic to the excitation methods. During CID, molecules are heated by less than 10 kJ mol⁻¹ per collision, followed by redistribution of the excess energy to the vibrational heat bath of the protein ion.⁵¹ This ultimately leads to dynamical sampling of accessible protein conformers by the CID-heated ions, preferentially accessing fragmentation pathways with the lowest dissociation barriers. Hence, fragmentation preferentially occurs for the energetically weakest bond.

In contrast, 213 nm UVPD introduces 562 kJ mol⁻¹ per photon to activate ions. While some degree of energy redistri-

bution will still occur, the energy introduced by UV photons can be sufficient to directly cleave amide bonds of approximately 335 kJ mol^{-1} or less (depending on Coulomb repulsion) prior to or after only partial energy redistribution or photon emission in gas-phase fluorescence.^{52,53} Therefore, 213 nm UVPD mass spectra should contain fragment ions also observed in CID experiments (particularly in ultrahigh vacuum with limited collisional cooling) but also additional fragments from direct bond cleavage. This is in line with our observation for ubiquitin, cytochrome c and myoglobin hinting to fragment ions arising due to charge-remote (side chain protonation) and charge-induced dissociation (amide protonation) in 213 nm UVPD.

Conclusions

In this work we investigated the effect of the overall protein ion charge state on the 213 nm UV photodissociation of native-like, unfolded and supercharged charge states of ubiquitin, cytochrome c and myoglobin in terms of the extent of fragmentation, the type of fragment ions that are formed, and fragmentation sites. The goal was not to explore the limits of sequence coverage in top-down UVPD measurements but to control the experimental conditions in order to systematically probe the intrinsic UVPD fragmentation of protein ions as a function of protein charge state. Our data strongly indicates that the photoproduct yields and sequence coverages increase as the charge state increases. The major factor that impacts top-down 213 nm UVPD fragmentation of protein ions is the overall protein charge state, and the effects of secondary/tertiary structural changes of these protein ions are less pronounced under these conditions. The extent of protein ion charging correlates with the sequence coverage and the *PY* value but the relative number of different fragment ion types that are formed is largely independent of protein charge state. In particular, the relative sequence coverage increase depends more strongly on the number of charges per amino acid residues than on the masses or identity of the proteins. For unfolded and supercharged charge states these results are consistent with a major driving force in the dissociation of intact protein ions by 213 nm top-down UVPD being the Coulomb repulsion between individual localized charges in these multiply charged protein ions.

Comparison of the protein cleavage sites and abundances to predicted charge locations and the resulting calculated electrostatic potentials reveal that the majority of cleavage sites are consistent with two mechanisms. For protein ions in which the proton number does not exceed the number of high-basicity residues in which protons are located primarily on high-basicity amino acid residue side chains, the majority of fragment ions stem from sites of local coulombic minima between adjacent charges. Unlike, fragmentation in ECD and ETD in which fragmentation sites are directed by the location of protons, the majority of fragments in our UVPD results arise at sites with a relatively large distance between predicted proto-

nation sites thereby minimizing coulombic repulsion upon dissociation.³⁴ For some supercharged protein ions the number of protons exceed the number of basic sites and protonation of the amide backbone is predicted. For these highly charged protein ions, cleavage sites are not only determined by the Coulomb repulsion but also by amide protonation as high sequence ion abundance is observed in the same region in which amide backbone protonation is predicted. This, however, is in marked contrast to top-down CID results for the same protein ion, which is dominated by highly selective fragment ions formed typically at the first amide backbone site that is predicted to be protonated with increasing charge state.⁸

In contrast to our results, another study has investigated the protein charge state dependence in 213 nm top-down UVPD experiments on an orbitrap instrument and found that sequence coverage does not depend on the charge density of highly charged protein ions.^{29,48} A potential explanation for these differences is the pressure regimes in which UVPD is performed. In our FT-ICR MS, pressures of 2×10^{-10} mbar minimizes ion-neutral collisions during UVPD experiments, whereas frequent deactivating collision at about 10^{-5} mbar could minimize fragmentation arising from vibrational excitation owing to intramolecular vibrational relaxation from electronically excited states. Such an effect of pressure has been studied by Hao *et al.* who demonstrated that the intensities of UVPD-like fragments can decrease at lower pressures.³⁸

Thus, these results can be considered a first step towards rationalizing fragmentation sites in top-down 213 nm UVPD as a function of charge state but more work is required to understand the differences between different UVPD wavelength, the impact of the wavelengths on sequence coverage results, influences of locally different UV absorption cross sections, and additional effects of experimental conditions on the UVPD charge-state dependence.

Conflicts of interest

The authors declare no competing financial interest.

Acknowledgements

S.H. acknowledges the Fonds der chemischen Industrie for financial support through a Liebig fellowship. The authors thank Alexander S. Berninger for initial support during this project and Marion Girod for providing their UVPD data. W.A. D. thanks the Australian Research Council for funding (FT200100798).

References

- 1 C. Xia, Y. Tao, M. Li, T. Che and J. Qu, *Exp. Ther. Med.*, 2020, **20**, 2923–2940.

- 2 M. Fournier, M. Orpinell, C. Grauffel, E. Scheer, J.-M. Garnier, T. Ye, V. Chavant, M. Joint, F. Esashi, A. Dejaegere, P. Gönczy and L. Tora, *Nat. Commun.*, 2016, **7**, 13227.
- 3 S. K. Wierenga, M. J. Zocher, M. M. Mirus, T. P. Conrads, M. B. Goshe and T. D. Veenstra, *Rapid. Commun. Mass Spectrom.*, 2002, **16**, 1404–1408.
- 4 S. Hildonen, T. G. Halvorsen and L. Reubsæet, *Proteomics*, 2014, **14**, 2031–2041.
- 5 S. Doll and A. L. Burlingame, *ACS Chem. Biol.*, 2015, **10**, 63–71.
- 6 S. C. Beu, M. W. Senko, J. P. Quinn, F. M. Wampler III and F. W. McLafferty, *J. Am. Soc. Mass Spectrom.*, 1993, **4**, 557–565.
- 7 W. Cai, H. Guner, Z. R. Gregorich, A. J. Chen, S. Ayaz-Guner, Y. Peng, S. G. Valeja, X. Liu and Y. Ge, *MCP*, 2016, **15**, 703–714.
- 8 H. Wang, M. G. Leeming, J. Ho and W. A. Donald, *Chem. – Eur. J.*, 2019, **25**, 823–834.
- 9 H. Wang, G. Yong, S. L. Brown, H. E. Lee, M. A. Zenaidee, C. T. Supuran and W. A. Donald, *Anal. Chim. Acta*, 2018, **1003**, 1–9.
- 10 J. F. Nemeth-Cawley, S. Karnik and J. C. Rouse, *J. Mass Spectrom.*, 2001, **36**, 1301–1311.
- 11 N. I. Brodie, R. Huguet, T. Zhang, R. Viner, V. Zabrouskov, J. Pan, E. V. Petrochenko and C. H. Borchers, *Anal. Chem.*, 2018, **90**, 3079–3082.
- 12 N. C. Polfer, *Chem. Soc. Rev.*, 2011, **40**, 2211–2221.
- 13 D. P. Little, J. P. Speir, M. W. Senko, P. B. O'Connor and F. W. McLafferty, *Anal. Chem.*, 1994, **66**, 2809–2815.
- 14 J. J. Coon, J. Shabanowitz, D. F. Hunt and J. E. P. Syka, *J. Am. Soc. Mass Spectrom.*, 2005, **16**, 880–882.
- 15 H. Molina, R. Matthiesen, K. Kandasamy and A. Pandey, *Anal. Chem.*, 2008, **80**, 4825–4835.
- 16 M. A. Zenaidee, M. G. Leeming, F. Zhang, T. T. Funston and W. A. Donald, *Angew. Chem., Int. Ed.*, 2017, **56**, 8522–8526.
- 17 J. B. Shaw, W. Li, D. D. Holden, Y. Zhang, J. Griep-Raming, R. T. Fellers, B. P. Early, P. M. Thomas, N. L. Kelleher and J. S. Brodbelt, *J. Am. Chem. Soc.*, 2013, **135**, 12646–12651.
- 18 J. A. Madsen, D. R. Boutz and J. S. Brodbelt, *J. Proteome Res.*, 2010, **9**, 4205–4214.
- 19 T. Ly and R. R. Julian, *Angew. Chem., Int. Ed.*, 2009, **48**, 7130–7137.
- 20 J. S. Brodbelt, L. J. Morrison and I. Santos, *Chem. Rev.*, 2020, **120**, 3328–3380.
- 21 J. Bonner, Y. A. Lyon, C. Nellessen and R. R. Julian, *J. Am. Soc. Mass Spectrom.*, 2017, **139**, 10286–10293.
- 22 M. B. Cammarata and J. S. Brodbelt, *Chem. Sci.*, 2015, **6**, 1324–1333.
- 23 W. Cui, M. S. Thompson and J. P. Reilly, *J. Am. Soc. Mass Spectrom.*, 2005, **16**, 1384–1398.
- 24 M. S. Thompson, W. Cui and J. P. Reilly, *Angew. Chem., Int. Ed.*, 2004, **43**, 4791–4794.
- 25 S. Becher, P. Esch and S. Heiles, *Anal. Chem.*, 2018, **90**, 11486–11494.
- 26 J. Bonner, L. E. Talbert, N. Akkawi and R. R. Julian, *Analyst*, 2018, **143**, 5176–5184.
- 27 A. Y. Pereverzev, Z. Koczor-Benda, E. Saparbaev, V. N. Kopysov, E. Rosta and O. V. Boyarkin, *J. Phys. Chem. Lett.*, 2020, **11**, 206–209.
- 28 A. Chakir, G. Solignac, A. Mellouki and D. Daumont, *Chem. Phys. Lett.*, 2005, **404**, 74–78.
- 29 L. Fornelli, K. Srzentić, T. K. Toby, P. F. Doubleday, R. Huguet, C. Mullen, R. D. Melani, H. Dos Santos Seckler, C. J. DeHart, C. R. Weisbrod, K. R. Durbin, J. B. Greer, B. P. Early, R. T. Fellers, V. Zabrouskov, P. M. Thomas, P. D. Compton and N. L. Kelleher, *Mol. Cell. Proteomics*, 2020, **19**, 405–420.
- 30 M. Girod, Z. Sanader, M. Vojkovic, R. Antoine, L. MacAleese, J. Lemoine, V. Bonacic-Koutecky and P. Dugourd, *J. Am. Soc. Mass Spectrom.*, 2015, **26**, 432–443.
- 31 E. D. B. Foley, M. A. Zenaidee, R. F. Tabor, J. Ho, J. E. Beves and W. A. Donald, *Anal. Chim. Acta*, 2019, **1**, 100004.
- 32 A. Theisen, R. Black, D. Corinti, J. M. Brown, B. Bellina and P. E. Barran, *J. Am. Soc. Mass Spectrom.*, 2019, **30**, 24–33.
- 33 C. A. Teo and W. A. Donald, *Anal. Chem.*, 2014, **86**, 4455–4462.
- 34 M. A. Zenaidee and W. A. Donald, *Anal. Methods*, 2015, **7**, 7132–7139.
- 35 S. Becher, B. Spengler and S. Heiles, *Eur. J. Mass Spectrom.*, 2018, **24**, 54–65.
- 36 P. Roepstorff and J. Fohlman, *Biomed. Mass Spectrom.*, 1984, **11**, 601.
- 37 P. D. Schnier, D. S. Gross and E. R. Williams, *J. Am. Soc. Mass Spectrom.*, 1995, **6**, 1086–1097.
- 38 C. Hao, J. C. Y. Le Blanc, U. H. Verkerk, K. W. M. Siu and A. V. Loboda, *Rapid Commun. Mass Spectrom.*, 2010, **24**, 2262–2268.
- 39 A. V. Tolmachev, E. W. Robinson, S. Wu, L. Paša-Tolić and R. D. Smith, *Int. J. Mass Spectrom.*, 2009, **281**, 32–38.
- 40 S. H. Lomeli, S. Yin, R. R. Ogorzalek Loo and J. A. Loo, *J. Am. Soc. Mass Spectrom.*, 2009, **20**, 593–596.
- 41 A. T. Iavarone, J. C. Jurchen and E. R. Williams, *J. Am. Soc. Mass Spectrom.*, 2000, **11**, 976–985.
- 42 C. A. Cassou, H. J. Sterling, A. C. Susa and E. R. Williams, *Anal. Chem.*, 2013, **85**, 138–146.
- 43 L. Kolbowski, A. Belsom and J. Rappsilber, *J. Am. Soc. Mass Spectrom.*, 2020, **31**, 1282–1290.
- 44 J. P. O'Brien, W. Li, Y. Zhang and J. S. Brodbelt, *J. Am. Chem. Soc.*, 2014, **136**, 12920–12928.
- 45 S. Vahidi, B. B. Stocks and L. Konermann, *Anal. Chem.*, 2013, **85**, 10471–10478.
- 46 J. C. May, E. Jurneczko, S. M. Stow, I. Kratochvil, S. Kalkhof and J. A. McLean, *Int. J. Mass Spectrom.*, 2018, **427**, 79–90.
- 47 D. S. Gross and E. R. Williams, *J. Am. Chem. Soc.*, 1995, **117**, 883–890.
- 48 M. A. Halim, M. Girod, L. MacAleese, J. Lemoine, R. Antoine and P. Dugourd, *J. Am. Soc. Mass Spectrom.*, 2016, **27**, 1435–1442.
- 49 M. J. Nold, C. Wesdemiotis, T. Yalcin and A. G. Harrison, *Int. J. Mass Spectrom.*, 1997, **164**, 137–153.

- 50 A. Somogyi, V. H. Wysocki and I. Mayer, *J. Am. Soc. Mass Spectrom.*, 1994, **5**, 704–717.
- 51 A. P. Horton, S. A. Robotham, J. R. Cannon, D. D. Holden, E. M. Marcotte and J. S. Brodbelt, *Anal. Chem.*, 2017, **89**, 3747–3753.
- 52 S. J. Blanksby and G. B. Ellison, *Acc. Chem. Res.*, 2003, **36**, 255–263.
- 53 M. F. Czar, F. Zosel, I. König, D. Nettels, B. Wunderlich, B. Schuler, A. Zarrine-Afsar and R. A. Jockusch, *Anal. Chem.*, 2015, **87**, 7559–7565.

III. Appendix

Acknowledgements

I would like to thank Prof. Dr. Spengler for the opportunity to work on this exciting topic and for trusting me in the instrumental modifications. The opportunity to learn everything about mass spectrometers and insights into engineering expanded my horizon and was a challenging, fulfilling task for the last years. Sincere thanks to Prof. Dr. Bernd Smarsly for his willingness to be the second referee of this thesis. Also, I thank Prof. Dr. Siegfried Schindler and Prof. Dr. Martin Rühl for being a part of my examination committee.

I am highly grateful to Jun-Prof. Dr. Sven Heiles, who supervised my research in the laboratory for more than five years. The fruitful, regular discussions helped a lot to expand my understanding, on the one hand, and to develop and evaluate new ideas, on the other hand. It was a pleasure to be a part of the Heiles team.

During this project I got in contact with collaboration partners. For the discussions and the contribution of this thesis, I would like to thank Prof. Dr. Jos Oomens, Dr. Giel Berden, Dr. Jonathan Martens, Dr. Huixin Wang, Dr. Michael G. Leeming, Prof. Dr. William A. Donald, and Dr. Susannah Brown. For ongoing conversations, social events, an awesome working atmosphere in the lab and at conferences I would like to express heartfelt thanks to Fabian Wäldchen, Dr. Stefanie Gerbig, Felix Hormann, Patrick Esch, David Lüke, Lars Liebschwager, Christian Schinz, Parviz Ghezellou, and the whole group of Prof. Spengler. Comprehensive knowledge in instrumentations of Dr. Christian Schäfer and support in component crafting by Ralf Sack were important parts of this work.

Finally, I am indescribably thankful for the support of my family, my friends, and my American Football team. They helped me during all ups and downs of my studies and ultimately the completion of this doctoral thesis. Thanks a lot Christine Betz, Andreas Becher, Anna Becher, Lea Becher, Paul Lukas Huber, Martin Klein, Marc Marcel Farnschläder, Andreas Betz, and Erich Heinz. Special thanks to Svenja Sommer, you are a safe anchor in stormy times, a lovely fellow, and the best partner I can imagine.

Declaration

I declare that I have completed this dissertation without the unauthorized help of a second party and only with the assistance acknowledged herein. I have appropriately acknowledged and referenced all text passages that are derived literally from or are based on the content of published or unpublished work of others, and all information that relates to verbal communications. I have abided the principles of good scientific conduct laid down in the charter of the Justus Liebig University of Giessen in carrying out the investigations described in the dissertation.

Place, date and signature